

## LA-UR-14-28809

Approved for public release; distribution is unlimited.

Title: Reduction of dissipation in Lagrange cell-centered hydrodynamics (CCH)  
through corner gradient reconstruction (CGR)

Author(s): Burton, Donald E.  
Morgan, Nathaniel Ray  
Carney, Theodore Clayton  
Kenamond, Mark Andrew

Intended for: Report

Issued: 2015-06-09 (rev.2)

---

**Disclaimer:**

Los Alamos National Laboratory, an affirmative action/equal opportunity employer, is operated by the Los Alamos National Security, LLC for the National Nuclear Security Administration of the U.S. Department of Energy under contract DE-AC52-06NA25396. By approving this article, the publisher recognizes that the U.S. Government retains nonexclusive, royalty-free license to publish or reproduce the published form of this contribution, or to allow others to do so, for U.S. Government purposes. Los Alamos National Laboratory requests that the publisher identify this article as work performed under the auspices of the U.S. Department of Energy. Los Alamos National Laboratory strongly supports academic freedom and a researcher's right to publish; as an institution, however, the Laboratory does not endorse the viewpoint of a publication or guarantee its technical correctness.

# Reduction of dissipation in Lagrange cell-centered hydrodynamics (CCH) through corner gradient reconstruction (CGR)

D.E. Burton<sup>a,\*</sup>, N. R. Morgan<sup>a</sup>, T.C. Carney<sup>a</sup>, M.A. Kenamond<sup>a</sup>

<sup>a</sup>X-Computational Physics Division; Los Alamos National Laboratory; P.O. Box 1663, Los Alamos, NM, USA

---

## Abstract

This work presents an extension of a second order cell-centered hydrodynamics scheme on unstructured polyhedral cells [13] toward higher order. The goal is to reduce dissipation, especially for smooth flows. This is accomplished by multiple piecewise linear reconstructions of conserved quantities within the cell. The reconstruction is based upon gradients that are calculated at the nodes, a procedure that avoids the least-square solution of a large equation set for polynomial coefficients. Conservation and monotonicity are guaranteed by adjusting the gradients within each cell corner. Results are presented for a wide variety of test problems involving smooth and shock-dominated flows, fluids and solids, 2D and 3D configurations, as well as Lagrange, Eulerian, and ALE methods.

**Keywords:** Lagrangian, hydrodynamics, Godunov, cell-centered, finite-volume, reconstruction, higher-order, dissipation, CCH, corner gradient reconstruction, CGR

---

## 1. Introduction

In cell-centered hydrodynamics schemes (CCH), all conservation equations are solved on a common control volume. As we discuss later, modern CCH methodology was enabled by the work of Després and Mazeran [33], followed by Maire and others [74, 13]. The following work is based upon the particular second order method (denoted CCH2) described in [13, 15], but the results are applicable to other implementations.

As discussed in [13] and also in [16], CCH is quite accurate on shock-driven test problems. However, it has been noted that the second order method can generate dissipation errors for many smooth flows. As an example of the dissipation, we consider the motion of an oscillating elastic plate that will be discussed in detail in Section 5.1. Figure 1 shows the calculated vertical velocity of the central point of the plate. Because the plate is elastic, the amplitude of the oscillations should remain relatively constant in time. For an undamped reference calculation (green), this is essentially true. However, the CCH2 method artificially dissipates kinetic energy.

In this work, we seek to increase the accuracy of CCH by employing a higher order extension that significantly reduces the dissipation error in such cases. CCH2 uses a finite volume spatial integration and a two stage Runge-Kutta temporal integration (RK2). Each Lagrange step begins with the knowledge of the extensive values of conserved quantities within cells. In finite volume methods, the distribution of conserved quantities within a cell is not known *a priori* and must be reconstructed or inferred from values in adjacent cells. As described later, 2nd and higher order CCH methods differ principally in the details of this reconstruction that must be constrained to be both conservative and monotonic. In the 2nd order reconstruction of References [13, 71], conserved quantities within cells are distributed linearly using monotonicity preserving gradients. A 3rd order reconstruction would require a quadratic polynomial having 6 coefficients in 2D and 10 in 3D. A least-squares (LSQ) solution for those coefficients involves the computationally expensive solution of a multi-equation system for each cell and for each reconstructed variable. Further, as discussed by Cheng and Shu [27], third and higher order schemes require curvature of the cell faces to achieve the specified order. Our work focuses on improvements to the second-order method while retaining straight cell faces.

---

\*Corresponding author: burton@lanl.gov

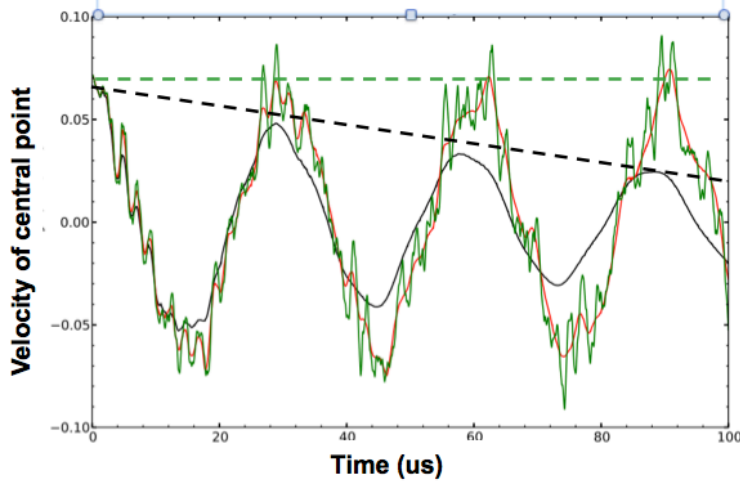


Figure 1: Vertical velocity of the central point in a bending Be plate. Reference calculation (green), CCH2 (black), (red) to be discussed later.

A more computationally efficient alternative to 3rd order is a piecewise linear reconstruction that we call Corner Gradient Reconstruction or CGR. The method is not formally 3rd order, but captures many of its properties. In CGR, linear functions are generated at each mesh point and applied in each cell corner. The solution for the point gradients involves only Cramer’s rule.

### 1.1. Organization of the paper

The paper is organized in two principal parts, the first explaining the theory and the second presenting test calculations. The theory begins with a brief explanation of notation in Section 1.2 and follows with an overview of CCH2 in Section 2. The notion of reconstruction is explored generally in Section 3 and in detail for CGR in Section 4. The test problems beginning in Section 5 are ordered by (a) smooth flows starting in Section 5.1, (b) shock dominated flows starting in Section 6.1, (c) and finally Eulerian and ALE problems starting in Section 7.2. We summarize our conclusions in Section 8. Details of the solid model are given in Appendix A.

### 1.2. Mesh topology and notation

A discretization stencil describes how information defined on grids is spatially connected. It is important that the mathematical formulation be consistent with the stencil. For polytopal grids, potential complexity is overcome by finding a simple but universal stencil. Our stencil is a minor extension of the multi-dimensional unstructured stencil of Reference [10] and is formed by decomposing polytopal cells into triangular (2D) or tetrahedral (3D) substructures. This gives rise to a number of geometrical entities depicted in Figure 2. In 3D, the various control positions  $p$ ,  $z$ ,  $f$ , and  $e$  denote respectively points (or nodes), zones (or cells), faces, and edges. In 2D, also depicted in Figure 2, the face and edge control positions are degenerate.

The *iota* is the smallest letter in the Greek alphabet, and will be used to denote the smallest simplex definable with this set of control positions  $\{p, z, f, e\}$ . Depending upon the dimensionality, the iota is bounded by one of each of the types of control positions. The stencil also includes connectivity to adjacent iotas. The cell *corner*  $c$  consists of those iotas sharing a common  $z$  and  $p$ .

In the discrete equations, it will be necessary to refer to physical quantities in relation to the iota connectivity structure. The iota will be indicated by a superscript. The logical location of the variable relative to a particular iota is identified with a subscript. For example,  $\mathbf{u}_z^i$  and  $\mathbf{u}_p^i$  denotes velocity at cell center and point respectively relative to iota  $i$ , while  $\sigma_z^i$  and  $\sigma_p^i$  denote the stress at the respective locations. A geometrical quantity associated with an iota is the outward directed surface normal  $\mathbf{N}^i = N^i \hat{\mathbf{n}}^i$  with area  $N^i$  and direction  $\hat{\mathbf{n}}^i$ . Here we use a caret to indicate unit vectors.



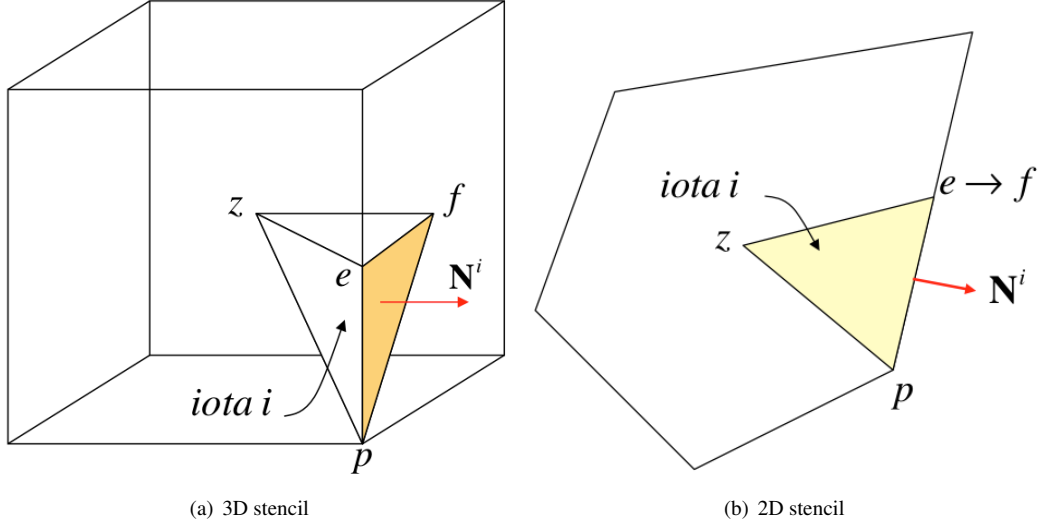


Figure 2: 3D and 2D discretization stencils showing relation of the *iota* to a computational cell and control points. The *f* and *e* positions are degenerate in 2D, and also the *p* position in 1D.

*Sums:* It will be necessary to perform summations over *iotas* or other geometrical quantities. Considerable notational simplification is achieved if summations are expressed in terms of *iotas*. In summation expressions, superscripts will be used to denote the *iota* index. In such expressions, where typographic fonts permit, vectors and tensors will be bold faced. For example, the geometrical statement that the sum of surface vectors about a closed cell *z* or about a point *p* is zero can be expressed as

$$\oint_z d\mathbf{N} = \sum_i^z \mathbf{N}^i = 0$$

$$\sum_i^p \mathbf{N}^i = 0$$

In the first expression, the subscript *i* and the superscript *z* indicate that we are summing over all the *iotas* inside the cell *z*. Likewise, the superscript *p* in the second expressions indicates we are summing over *iotas* surrounding a point *p*.

*Scalars, vectors, tensors:* In expressions not involving the *iota* index, we may use *indicial* notation in which superscripts denote vector and tensor components, and the Einstein summation convention over repeated indices is followed. Scalar products are indicated by a dot, such as  $\hat{\mathbf{n}} \cdot \sigma \leftrightarrow \hat{n}^i \sigma^{ij}$ . Dyadic tensors are indicated by juxtaposition  $\hat{\mathbf{n}}\mathbf{u} \leftrightarrow \hat{n}^i u^j$ . The double scalar product is expressed  $\sigma: \mathbf{G} \leftrightarrow \sigma^{ij} G^{ij}$ .

*Gradients:* A subscript on the nabla operator indicates that it is a discrete version while also indicating how it is centered in space. For example,  $\nabla_z \mathbf{u}$  represents the discrete cell-centered gradient of velocity that is centered within the cell. In indicial notation, this gradient would be expressed  $\partial_z^i u^j$ .

*Temporal notation:* Whereas discrete spatial differencing is indicated in the subscript of the differential operators, temporal discretization is also indicated with superscripts. For example, we write that a time marching scheme is used to advance cell quantities in time  $t^n \rightarrow t^{n+1}$ . An RK2 scheme is used to center quantities appearing in the evolution equations at  $n + 1/2$ . Since the bulk of the formulation involves the consideration of quantities that are centered at  $n + 1/2$ , it is convenient to omit those superscripts.

## 2. CCH overview

Most Lagrange and many Eulerian schemes are derivatives of the original von Neumann and Richtmyer (VNR) 1D formulation [110], now commonly termed staggered grid hydrodynamics (SGH). In SGH the evolution equations for

stress and momentum are solved on offset control volumes such that the logical center of each lies on the boundary of the other. Cell-centered hydrodynamics schemes (CCH) in which all conservation equations are solved on a common control volume have been widely applied to Eulerian methods, but only recently widely applied to Lagrange. A cell-centered Lagrange method was first suggested by Godunov [49, 48]. Early implementations such as that in the CAVEAT code [2, 39] solved an approximate Riemann problem at cell faces rather than at the nodes. It was not until the seminal work of Després and Mazeran [33] that a solution at the nodes was found. Since then, interest in CCH methods has increased and at least three additional formulations have arisen [74, 3, 13] giving rise to extensions in many areas [25, 32, 58, 75, 76, 71, 77, 70, 46, 45, 73, 72, 21, 14, 81, 15, 80]. Although the discussion in this paper is centered about the CCH2 formulation of [13, 15], it is relevant to all.

We begin with an overview of the CCH2 method. Details are in the cited references that we summarize here in very general terms. Reference [13] describes the basic XY formulation while [15] describes an RZ formulation based on conservative fluxes that preserves symmetry on equiangular polar meshes. The cyclic ordering of the steps depends upon the particular implementation. For purposes of discussion, we begin with the finite volume integration.

*Finite volume integration.* The extensive evolution or rate equations for momentum, deformation, and total energy are expressed as surface integrals

$$\dot{\mathbf{U}}_z = M_z \dot{\mathbf{u}}_z = \oint_z d\mathbf{N} \cdot \boldsymbol{\sigma} \rightarrow \sum_i^z \mathbf{N}^i \cdot \boldsymbol{\sigma}_p^i \quad (1)$$

$$\dot{\Gamma}_z = M_z \dot{\gamma}_z = \oint_z d\mathbf{N} \mathbf{u} \rightarrow \sum_i^z \mathbf{N}^i \mathbf{u}_p^i \quad (2)$$

$$\dot{T}_z = M_z \dot{\tau}_z = \oint_z d\mathbf{N} \cdot \boldsymbol{\sigma} \cdot \mathbf{u} \rightarrow \sum_i^z \mathbf{N}^i \cdot \boldsymbol{\sigma}_p^i \cdot \mathbf{u}_p^i \quad (3)$$

in which  $M_z$  is the cell mass and  $\{\dot{\mathbf{u}}_z, \dot{\gamma}_z, \dot{\tau}_z\}$  are respectively specific cell average rates of change of velocity, deformation, and total energy. The fundamental challenge in CCH is the determination of the surface fluxes  $\mathbf{u}_p$  and  $\boldsymbol{\sigma}_p$  that are solutions to a Riemann problem. The decomposition of the total energy into kinetic and internal rates  $\{\dot{k}_z, \dot{e}_z\}$  will be discussed later in Section 2.1. A stress rate  $\dot{\sigma}_z$  is derived from the internal energy rate and deformation rate through a constitutive model such as that described in Appendix A. The rate equations are integrated to yield new values for velocity, stress, and total energy.

$$\begin{aligned} \mathbf{u}_z^{n+1} &= \mathbf{u}_z^n + \dot{\mathbf{u}}_z \delta t \\ \boldsymbol{\sigma}_z^{n+1} &= \boldsymbol{\sigma}_z^n + \dot{\boldsymbol{\sigma}}_z \delta t \\ \tau_z^{n+1} &= \tau_z^n + \dot{\tau}_z \delta t \end{aligned}$$

*Conservative reconstruction.* The finite volume method provides no direct information about the distribution of conserved quantities within a computational cell. A reconstructed distribution is inferred by reference to states in adjacent cells. The scheme we present in this paper differs from CCH2 in this reconstruction step. The conserved quantities to be reconstructed are momentum density and deformation. However, we make the simplifying assumptions of uniform density and uniform moduli, so that velocity and stress can be treated as conserved. The reconstruction is constrained by requiring (a) monotonicity or boundedness of the distribution and (b) conservation of the quantity within the cell, that is

$$V_z \mathbf{u}_z = \int_z \mathbf{u}(\mathbf{x}) dV \quad (4)$$

$$V_z \boldsymbol{\sigma}_z = \int_z \boldsymbol{\sigma}(\mathbf{x}) dV \quad (5)$$

The distribution then defines values of the fields at the point that are in general discontinuous

$$\begin{aligned}\mathbf{u}_c &= \mathbf{u}(\mathbf{x}_p) \\ \sigma_c &= \sigma(\mathbf{x}_p)\end{aligned}$$

*Flux conservation.* The detailed balance of incoming and outgoing fluxes is enforced by requiring the summation of fluxes at the nodes to vanish

$$\sum_i^p \mathbf{N}^i \cdot \mathbf{u}_p^i = 0 \quad (6)$$

$$\sum_i^p \mathbf{N}^i \cdot \sigma_p^i = 0 \quad (7)$$

The first is satisfied by a condition of velocity continuity; that is,  $\mathbf{u}_p^i$  is the same for all  $i$  surrounding the point  $p$ . The second must be explicitly enforced as in [33, 74, 13] since  $\sigma_p^i$  is discontinuous; that is, not the same for all  $i$  surrounding the point  $p$ .

*Nodal solution.* Following [13], we assert a Riemann jump condition

$$\hat{\mathbf{n}} \cdot \delta_{pc} \sigma = \mu \delta_{pc} \mathbf{u} |\hat{\mathbf{n}} \cdot \hat{\mathbf{a}}| \quad (8)$$

in which

$$\delta_{pc} \mathbf{u} = \mathbf{u}_p - \mathbf{u}_c \quad (9)$$

and similarly for stress. The quantity  $\hat{\mathbf{a}} = \delta_{pc} \mathbf{u} / |\delta_{pc} \mathbf{u}|$  is a unit vector in the direction of the shock. As discussed in [13], the factor  $|\hat{\mathbf{n}} \cdot \hat{\mathbf{a}}|$  corrects for the shock intersecting the cell face at an angle. The quantity  $\mu > 0$  is an impedance that is the product of density times the shock velocity  $\mu = \rho a$ . Various authors [62, 114] have given approximate forms for the shock velocity. Here, we use a form due to Dukowicz [38]

$$a = c + s \delta^* u \quad (10)$$

in which  $c$  is the sound speed and

$$\delta^* u = \begin{cases} |\delta \mathbf{u}| & \text{compression} \\ 0 & \text{expansion} \end{cases}$$

For polytropic gases,  $s = (\gamma + 1)/2$ . For solids,  $s$  is the slope of the  $U_s - U_p$  data as explained in Appendix A. As noted later in Section 5, we have reaffirmed conclusions of earlier work [74, 13] that the best results were obtained by ignoring the second term in Equation 10. As the term has a physical basis, this has remained a disconcerting observation.

Combined with the flux conservation relation for stress (Equation 7), the Riemann jump condition (Equation 8) defines an approximate Riemann problem that can be solved for

$$\mathbf{u}_p = \frac{\sum_i^p N^i [\mu^i \mathbf{u}_c^i |\hat{\mathbf{n}}^i \cdot \hat{\mathbf{a}}| - \hat{\mathbf{n}}^i \cdot \sigma_c^i]}{\sum_i^p N^i [\mu^i |\hat{\mathbf{n}}^i \cdot \hat{\mathbf{a}}|]} \quad (11)$$

The stress  $\sigma_p$  is then determined from the jump condition (Equation 8) on each  $i$ , thereby closing the system. Because  $\hat{\mathbf{a}}$  vanishes for stationary flow, the preceding expression can become singular. To avoid this, we interpolate between the trial value and the corner normal (defined below) depending upon whether the velocity difference is *large* or *small*

$$\hat{\mathbf{a}} = f \frac{\delta_{pc} \mathbf{u}}{|\delta_{pc} \mathbf{u}|} + (1 - f) \hat{\mathbf{n}}_c \quad (12)$$

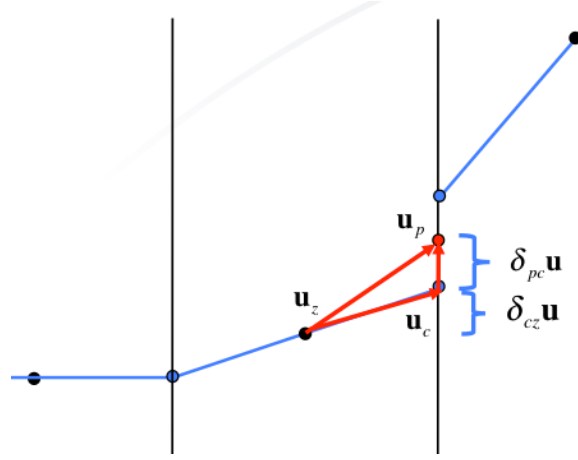


Figure 3: Depiction of 3 adjacent cells showing the decomposition of velocity into reconstruction (cz) and discontinuity (pc) components. A comparable decomposition of the stress tensor can also be made.

which is then renormalized to be a unit vector. The determination of *large* or *small* is made by comparing with the sound speed  $c$ . As we are only trying to avoid a singularity, the actual value of the sound speed is much larger than required, so that a fraction of it,  $\eta c$ , is used. The interpolation factor is then

$$f = \frac{|\delta_{pc}\mathbf{u}|}{\eta c + |\delta_{pc}\mathbf{u}|} \quad (13)$$

The corner normal  $\hat{\mathbf{n}}_c$  is defined by the normalized sum of the surface vectors in the corner and has itself been used directly in some cell-centered formulations [32]. By choosing a large value for  $\eta$ , the scheme can be forced to always use the corner normal, and this is done for some test problems.

### 2.1. Decomposition of the total energy equation

Dissipation is the irreversible transfer of kinetic to internal energy. To understand the algorithmic cause, it is necessary to decompose the total energy rate equation. Referring to Figure 3, the surface velocity and stress in each cell can be decomposed into a reconstruction component and a discontinuity.

$$\mathbf{u}_p = \mathbf{u}_z + \delta_{cz}\mathbf{u} + \delta_{pc}\mathbf{u}$$

with  $\delta_{cz}\mathbf{u} = \mathbf{u}_c - \mathbf{u}$  and similarly for stress. With this substitution, the total energy rate equation can be exactly decomposed into kinetic and internal terms

$$\begin{aligned} \dot{T}_z &= \oint_z \mathbf{dN} \cdot (\boldsymbol{\sigma}_p \cdot \mathbf{u}_p) \\ &= \dot{K}_z + \dot{E}_z \end{aligned}$$

with

$$\dot{E}_z = \dot{W}_z + \dot{R}_z + \dot{D}_z$$

The various contributions to the internal energy are discussed individually below. They can be directly evaluated, but in practice, the rate equation for internal energy is simply evaluated as

$$\dot{E}_z = \dot{T}_z - \dot{K}_z \quad (14)$$

*Kinetic energy.* The kinetic energy term is recognized as the rate of change of kinetic energy and is the product of the momentum rate and the cell average velocity

$$\dot{K}_z = \left[ \oint_z \mathbf{dN} \cdot \sigma_p \right] \cdot \mathbf{u}_z = \dot{\mathbf{U}}_z \cdot \mathbf{u}_z$$

If we define kinetic energy at time  $t^n$  as

$$K_z^n = \frac{M_z}{2} (\mathbf{u}_z^n)^2$$

and assume a uniform velocity distribution with time centering

$$\mathbf{u}_z = \frac{1}{2} (\mathbf{u}_z^n + \mathbf{u}_z^{n+1})$$

then it is algebraically exact that

$$\dot{K}_z \delta t = K_z^{n+1} - K_z^n$$

and this becomes the so called *compatible* form for kinetic energy [9, 8, 12, 11, 24].

*Reversible work.* The reversible work rate is the product of the average stress and the deformation rate

$$\dot{W}_z = \sigma_z : \left[ \oint_z \mathbf{dN} \mathbf{u}_p \right] = \sigma_z : \dot{\Gamma}_z$$

In this expression the stress is taken to be uniform and given by

$$\sigma_z = \sigma_z^{n+1/2}$$

*Reconstruction contribution.* The energy change due to the shape of the reconstruction is

$$\dot{R}_z = \oint_z \mathbf{dN} \cdot (\delta_{cz} \sigma \cdot \delta_{pc} \mathbf{u} + \delta_{cz} \mathbf{u} \cdot \delta_{pc} \sigma)$$

The first term is actually a correction to the kinetic energy due to a non uniform stress distribution. The second is a correction to the work due to a non uniform velocity distribution. Because of Equation 14, both terms in  $\dot{R}_z$  contribute to the internal energy. In principle, the kinetic energy component could be removed from the internal energy, but investigation of this is beyond the present scope.

*Dissipation.* The dissipation term is given by

$$\dot{D}_z = \oint_z \mathbf{dN} \cdot \delta_{pc} \sigma \cdot \delta_{pc} \mathbf{u}$$

With the introduction of the aforementioned Riemann jump condition (Equation 8) this term is always dissipative.

$$\dot{D}_z = \oint_z dN \mu |\hat{\mathbf{n}} \cdot \hat{\mathbf{a}}| \cdot (\delta_{pc} \mathbf{u})^2 \geq 0$$

The point of this discussion is that the source of dissipation is the  $\dot{D}_z$  term and that it can only be reduced by decreasing the discontinuity  $\delta_{pc} \mathbf{u}$ . This can be accomplished through the reconstruction.

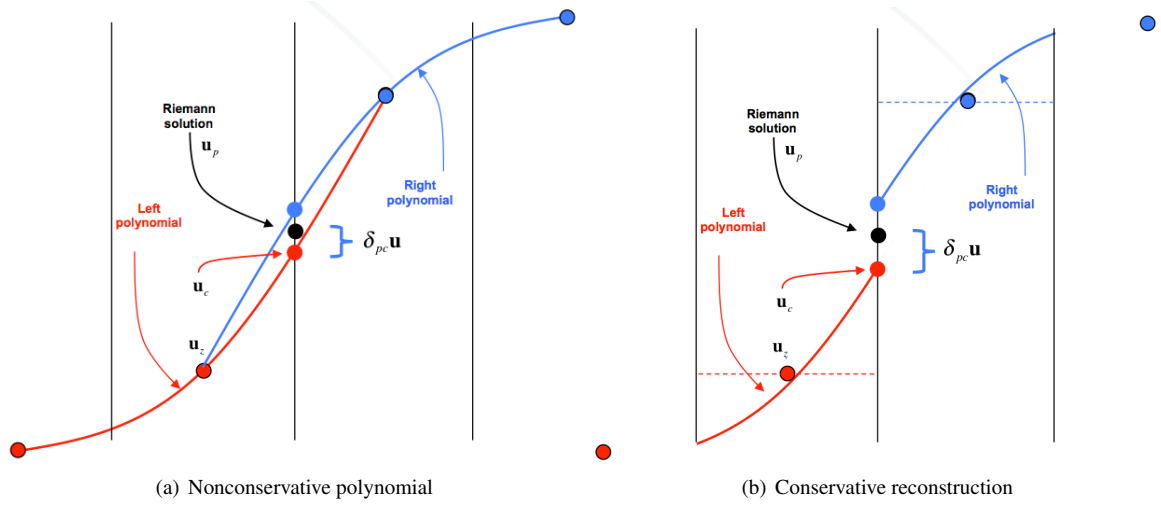


Figure 4: If left (red) and right (blue) polynomials are not coincident, dissipation occurs. Conservation in the sense of Equation 5 is achieved by shifting the polynomial segment within each cell.

### 3. Reconstruction overview

In this section, we will address the concept of reconstruction in general terms and become more specific in Section 4. The notion of reconstruction originated in the Eulerian hydrodynamic schemes involving the 1D advection equation on rectangular grids. For a review of the subject, see [106]. Application of reconstruction in Lagrangian schemes has been more limited. Both the CAVEAT code [2, 39] and Maire [75] employed second order Lagrange formulations. However, there have been several recent reports of higher order polynomial reconstructions. Boscheri and Dumbser recently used them in a 3D cell-centered ADER-WENO ALE scheme on tetrahedral meshes [6]. Charest, *et. al.* [26] have applied them to tetrahedra in a central differenced ENO (CENO) Eulerian scheme. Also, there have been several recent publications on discontinuous Galerkin methods [63, 1, 108] of which the last contains an excellent summary.

Reconstruction involves three considerations: (a) a polynomial fit to adjacent cells, (b) conservation within the cell (Equation 5), and (c) monotonicity with respect to adjacent cells. As noted previously, the result of these is an estimate (subscripted  $c$ ) of the field quantities internal to the cell  $z$ , so that at the point  $p$

$$\begin{aligned} \mathbf{u}_c &= \mathbf{u}(\mathbf{x}_p) \\ \sigma_c &= \sigma(\mathbf{x}_p) \end{aligned}$$

from which an approximate Riemann solution can be found for  $\mathbf{u}_p$ ,  $\sigma_p$ , and the discontinuity  $\delta_{pc} \mathbf{u}$  of Equation 9. We will cast our discussion principally in terms of velocity, but the principles apply to the stress tensor unless otherwise noted.

*(a) The polynomial.* When should dissipation occur? As smooth flow should not dissipate, we begin with a numerical notion of *smoothflow*. Consider the 1D situation at an interface depicted in Figure 4(a) for velocity. The idea is to fit a *left* polynomial (red) to the left cell and its immediate neighbors and a *right* polynomial to the right cell and its immediate neighbors. If the polynomials are coincident at the interface, then the flow is locally smooth and no dissipation should be created at the interface. If the polynomials are not coincident as in Figure 4, then there will be a discontinuity that is resolved by a Riemann-like solution, resulting in a nonzero  $\delta_{pc} \mathbf{u}$  and consequently dissipation in the energy equation.

*(b) Conservative reconstruction.* The second consideration is the conservation requirement

$$V_z \mathbf{u}_z = \int_z \mathbf{u}(\mathbf{x}) dV$$

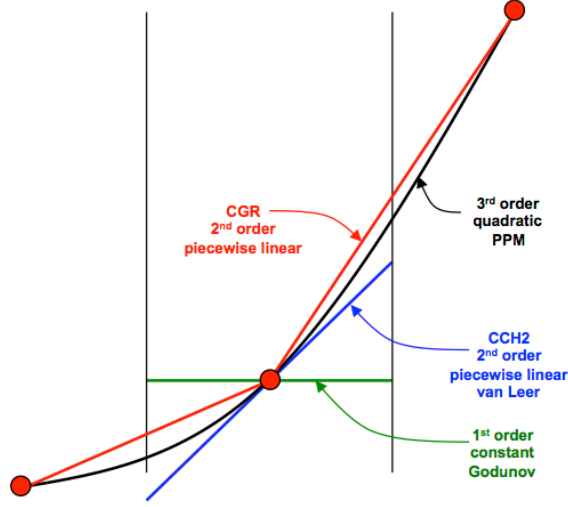


Figure 5: Comparison of first (green), second (blue), third (black), and CGR (red) reconstructions.

and similarly for stress. When the polynomial has curvature within the cell, the polynomial must be shifted to satisfy conservation as illustrated in Figure 4(b). This results in an increase in the discontinuity.

(c) *Monotonicity*. Finally, we wish the reconstruction to be monotonic. That is, the reconstruction should create no new extrema within the cell. This is accomplished by comparing  $\mathbf{u}_c$  and  $\sigma_c$  to the range of average values in neighboring cells and modifying the shape of the polynomial accordingly.

### 3.1. Comparison of reconstruction polynomials

We now compare the specific reconstructions of Figure 5. We again illustrate the discussion with velocity, but similar reconstruction is done for the stress tensor. Both are necessary to the solution of the approximate Riemann problem.

*Second order*. Second order reconstruction was introduced by van Leer [101, 102, 103, 104, 105] as an improvement to Godunov's first order method [47] and was designated MUSCL (Monotone Upstream Scheme for Conservation Laws). In the context of a Lagrangian method, this was the reconstruction used by Maire [75]. As illustrated in Figure 5, for vector component  $k$ , a first degree polynomial is fit to adjacent cells

$$u^k(\mathbf{x}) = u_0^k + \beta^k (x^j - x_z^j) \partial_p^j u^k$$

in which  $\beta^k$  is a limiter on the gradient and we use indicial notation.

To guarantee conservation in the sense of Equation 5, the second order polynomial is referenced to the centroid of the cell  $u_0^k \rightarrow u_z^k$ . If necessary, the gradient is multiplied by a slope limiter  $0 \leq \beta \leq 1$  to guarantee that  $\mathbf{u}_c$  and  $\sigma_c$  be bounded by the cell averages in adjacent cells. The approximate Riemann problem can then be solved to determine  $\mathbf{u}_p$  and  $\sigma_p$  and the discontinuity  $\delta_{pc} \mathbf{u}$ . The second order scheme is computationally efficient, but can result in excessive dissipation as shown in the beam problem of Figure 1.

The stencil commonly used in calculating the LSQ gradient  $\nabla \mathbf{u}$  is illustrated in Figure 6(a) and consists of *first nearest neighbors* (across cell faces) and optionally the cell itself. *Second nearest neighbors* (across cell corners) are not typically used because of ill-defined boundary conditions at the corners of rectangular grids. More will be said about this later. Because second nearest neighbors are not used, the second order gradients can be inaccurate in the diagonal direction.

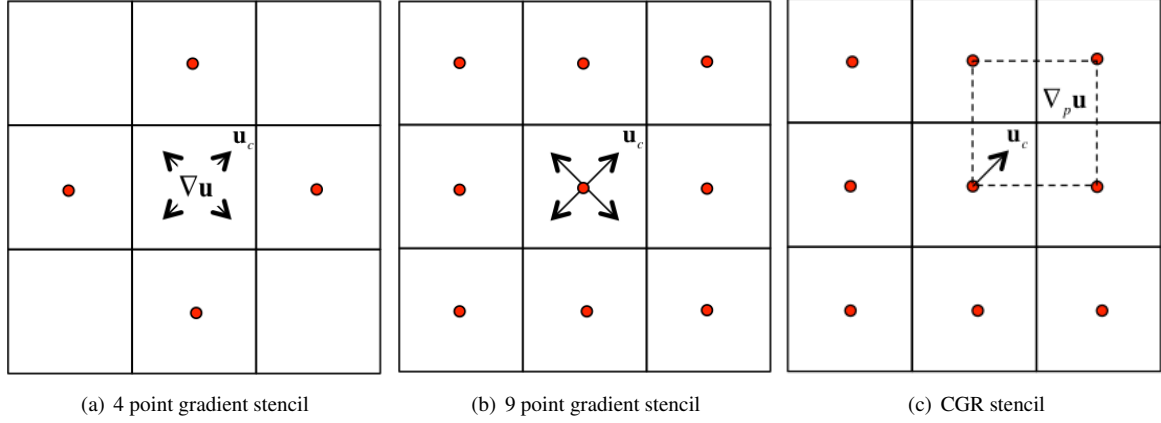


Figure 6: Gradient stencils commonly used in second and third order reconstruction are illustrated on a regular grid. The CGR stencil is illustrated in (c).

*Third order.* A third order method designated PPM (Piecewise Parabolic Method) was advanced by Colella and Woodward [30, 115]. The third order method is the most accurate of those illustrated in Figure 5. For 1D sweeps as originally applied in PPM, the calculation of the LSQ coefficients is inexpensive. However, this is not true in general. For a Lagrange cell in 2D, a second degree polynomial is fit to adjacent cells for each vector or tensor component

$$u^k(\mathbf{x}) = u_o^k + \beta(a_1^k \delta x + a_2^k \delta y) + \beta^2(a_{11}^k \delta x^2 + a_{22}^k \delta y^2 + a_{12}^k \delta x \delta y)$$

with  $\delta x = x - x_z$  and  $\delta y = y - y_z$ . The least squares solution for the coefficients then requires the solution of a 6-equation system in each cell for each vector and tensor component (8 components). In 3D, a 10-equation system for 9 components is necessary. The method is far more computationally expensive than the second order scheme.

The stencil for the least squares solution is nominally 9-point for a regular grid. The stencil is illustrated in Figure 6(b) and involves both first and second nearest neighbors. As noted in Section 4.1, boundary conditions for the 9-point stencil can be complicated on unstructured grids but are feasible.

#### 4. Corner gradient reconstruction (CGR)

In CGR, linear functions are generated at each mesh point and applied in each cell corner. The method does not appear to have been previously employed in cell-centered Lagrangian schemes. However, the notion of constructing subzonal slopes or gradients has been presented in at least two different Eulerian contexts. For 2D advection, Buffard and Clain [7] constructed a multi-slope MUSCL scheme using edge centered scalar slopes on a triangular mesh. In the context of 2D interface reconstruction, Fochesato, *et. al.* [42] calculated subzonal gradients to construct Youngs' [116] interfaces within subcells.

Like the 2nd order reconstruction method, CGR is a piecewise linear scheme, but with the segments bounded by the cell centroids. In terms of formal truncation error, both traditional CCH and CGR are second order for smooth flows. However, CGR is a closer representation of the third order function. It also captures a third order characteristic, that of varying slope within the cell. The stencil for the least squares solution is nominally 9-point for a 2D regular grid but is composed of smaller stencils at each node involving second nearest neighbors. These are illustrated in Figure 6(c).

Our goal is to reduce the dissipation, not necessarily to achieve the most accurate polynomial reconstruction. Consider Figure 7. In CGR, dissipation occurs only when *curvature* (a discontinuous slope) requires a shift to guarantee a conservative reconstruction. In the absence of the conservation requirement, the left and right polynomials (black) will be coincident, giving rise to zero dissipation. The presence of curvature, as indicted by differing slopes, will require a shift of the piecewise construction within the cell (red and blue) in order to satisfy the conservation requirement. This produces a discontinuity and consequently dissipation.



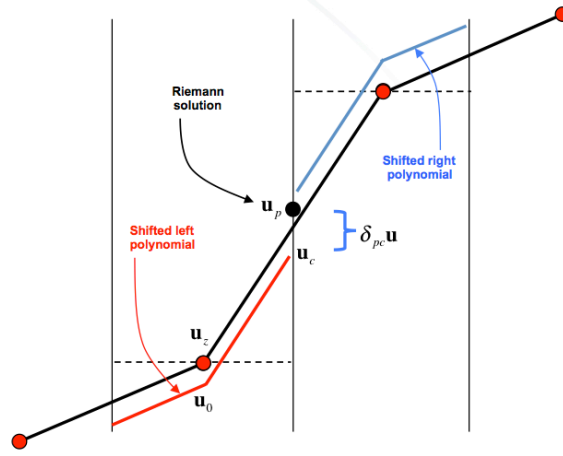


Figure 7: In CGR, dissipation occurs only when curvature requires a shift in the polynomial to guarantee a conservative reconstruction. Non-conservative CGR (black), conservative left polynomial (red), conservative right polynomial (blue).

#### 4.1. The gradient operator

In Section 4, we make extensive use of indicial notation. To preserve symmetry, we calculate the LSQ gradient referenced to the average of the cell centroids surrounding the node

$$\bar{x}_p^i = \frac{1}{N_p} \sum_n^p x_p^i$$

and similarly for velocity  $\bar{u}_p^i$ . Here, the surrounding cells are indexed by  $n$ . The various control points are shown in Figure 8(a). The red points are those used in the LSQ point gradient. Denoting

$$\begin{aligned} \delta x_n^i &= x_n^i - \bar{x}_p^i \\ \delta u_n^i &= u_n^i - \bar{u}_p^i \end{aligned}$$

the gradient at the point

$$g^{ij} = \partial_p^i u^j$$

is found from the optimization of the functional

$$F(g) = \sum_n^N \left[ \delta x_n^i g^{im} - \delta u_n^m \right] \left[ \delta x_n^j g^{jm} - \delta u_n^m \right]$$

Then

$$\begin{aligned} 0 &= \frac{1}{2} \frac{\partial F}{\partial g^{im}} = \sum_n^N \delta x_n^i \left[ \delta x_n^j g^{jm} - \delta u_n^m \right] \\ &= \left[ \sum_n^N \delta x_n^i \delta x_n^j \right] g^{jm} - \left[ \sum_n^N \delta x_n^i \delta u_n^m \right] \\ &= A^{ij} g^{jm} - B^{im} \end{aligned}$$

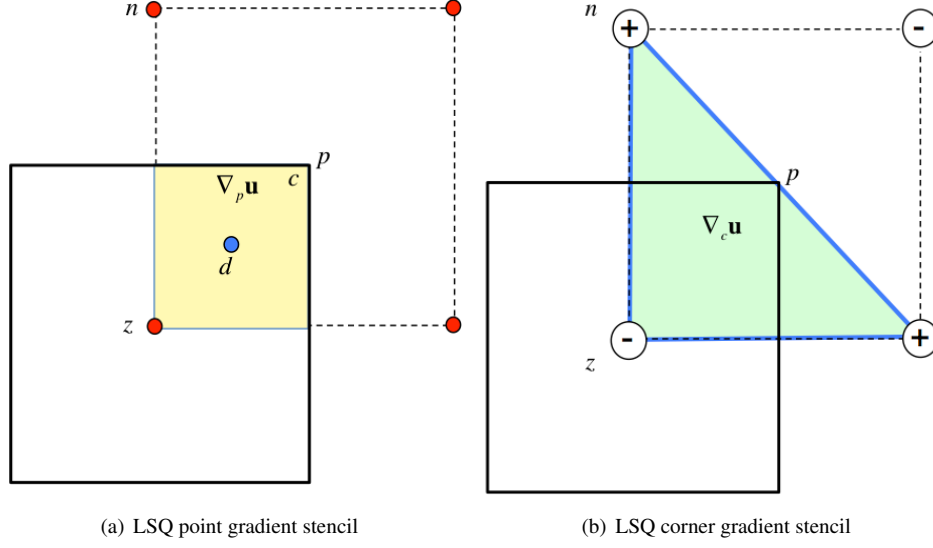


Figure 8: Stencils for point and corner gradients with locations of various control points with  $n$  indexing a neighboring cell,  $d$  being the centroid of a corner subcell, and  $c$  indexing a corner but being physically coincident with  $p$ .

in which

$$A^{ij} = \sum_n^N \delta x_n^i \delta x_n^j$$

$$B^{im} = \sum_n^N \delta x_n^i \delta u_n^m$$

This can be solved for the components of the velocity gradient by the simple application of Cramer's rule. The components of the stress tensor are treated similarly.

*Ghosts.* Boundary conditions for the gradient operator are commonly cast in terms of boundary ghost cells (blue) in Figure 9. The 9-point stencil requires a second nearest neighbor (denoted “?” in the Figure) at the corners of rectangular grids. The missing cell can be ignored in the LSQ solution, but this results in a loss of symmetry for some problems as we will discuss later in Sections 5.3 and 6.2. For regular grids, additional ghost cells are easily incorporated. However, for unstructured grids this is a challenging but tractable problem.

*Null modes.* There is an obvious similarity between the momentum control volume in SGH and the gradient stencil in Figure 8(a), suggesting that null modes (hourglass or checkerboard) could occur. Refer to Figure 8(b) in which a checkerboard pattern is illustrated by alternating high (+) and low (-) values. The LSQ point gradient of Figure 8(a) will vanish so that the mode is invisible to the differencing scheme, giving rise to null modes. However, the LSQ corner gradient (green) will not vanish. For smooth flows, the gradients are the same. The Taylor anvil test problem in Section 5.7 is a good example of a checkerboard null mode. The solution, then, is to mix the two gradients

$$\nabla \mathbf{u} = \lambda \nabla_c \mathbf{u} + (1 - \lambda) \nabla_p \mathbf{u} \quad (15)$$

with  $\lambda \sim 0.25$  being used for the problems in Section 5. We note that most of these test problems also produced satisfactory results without notable checkerboard for  $\lambda = 0$ , but those run with  $\lambda = 1$  were of noticeably lower quality.

#### 4.2. Velocity

Monotonicity is basically a scalar notion that can be extended to rank 1 and 2 tensors by considering either rotational invariants or eigenvalues. We follow the work of [74, 68] in limiting eigenvalues in the case of velocity and

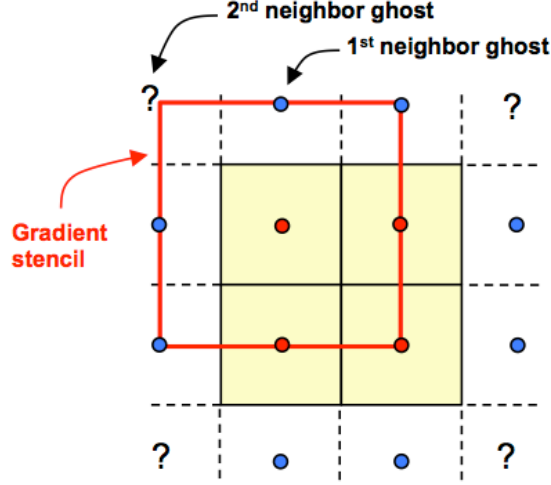


Figure 9: 9-point gradient stencil showing first (blue) and second (?) neighbor ghosts for a 2x2 rectangular grid (red).

the work of [13, 90] in limiting rotational invariants in the case of stress as discussed later. The limiting process in CGR is analogous to that of CCH2 [13]. The velocity reconstruction in cell  $z$  is performed in a rotated coordinate frame that is relevant to the flow, that is, in the principal system of the symmetrized gradient tensor as opposed to the fixed global frame of the problem. Quantities in this rotated frame will be denoted with a tilde. In each cell, the symmetrized velocity gradient or strain rate tensor is given by

$$\varepsilon_z^{ij} = \frac{1}{2} (\partial_z^i u^j + \partial_z^j u^i)$$

with

$$\partial_z^i u^j = \frac{1}{V_z} \sum_c V_c \partial_p^i u^j$$

In the global frame, the unlimited velocity difference (subscripted capital  $C$ ) between  $p$  and  $z$  is given by

$$\delta_C u^k = (x_p^j - x_z^j) \partial_p^j u^k$$

which becomes  $\delta_C \tilde{u}^k$  in the rotated frame. The limiting is performed relative to the rotated frame, so that the final corner velocity projection will be given by

$$\tilde{u}_c^k = \tilde{u}_0^k + \beta^k \delta_C \tilde{u}^k$$

with the quantity  $\tilde{u}_0^k$  determined by the conservation requirement.

*Conservation.* Referring to Figure 8(a), the unlimited velocity difference between the corner centroid  $d$  and the cell center  $z$  in the global frame is

$$\delta_D u^k = (x_d^j - x_z^j) \partial_p^j u^k$$

with  $x_d^j$  the centroid of the corner subcell. This becomes  $\delta_D \tilde{u}^k$  in the rotated frame. Then, the limited velocity at  $d$  is

$$\tilde{u}_d^k = \tilde{u}_0^k + \beta^k \delta_D \tilde{u}^k$$

The extensive quantity in a cell corner is given by the corner volume times the value at the corner centroid

$$\int_c \tilde{u}^k(x) dV = V_c (\tilde{u}_0^k + \beta^k \delta_D \tilde{u}^k)$$

so that, for the entire cell, the conserved quantity is

$$\tilde{u}_z^k V_z = \int_V \tilde{u}^k(x) dV = V_z (\tilde{u}_0^k + \beta^k \Delta \tilde{u}^k)$$

with

$$\Delta \tilde{u}^k = \frac{1}{V_z} \sum_c^z V_c \delta_D \tilde{u}^k$$

The velocity at the cell centroid  $z$  is then related to the limiter by

$$\tilde{u}_0^k(\beta^k) = \tilde{u}_z^k - \beta^k \Delta \tilde{u}^k$$

The shift and limiter calculations are coupled because a change in slope also affects the conservation integral. The limited corner velocity in the rotated frame then becomes

$$\tilde{u}_c^k = \tilde{u}_0^k(\beta^k) + \beta^k \delta_C \tilde{u}^k = \tilde{u}_z^k + \beta^k (\delta_C \tilde{u}^k - \Delta \tilde{u}^k)$$

with  $\beta$  determined by the monotonicity constraint.

*Monotonicity.* We use the method of Barth and Jespersen [4] as the basis of our monotonicity formulation. Let the set of cells including cell  $z$  itself and its first and second nearest neighbors be indexed by  $n$ . In the rotated frame, the bounds of  $z$  are functions of the cell average velocities

$$\tilde{u}_\pm^k = \text{Max/Min}_n^z [\alpha \tilde{u}_n^k + (1 - \alpha) \tilde{u}_z^k] \quad (16)$$

$$\alpha = \begin{cases} 0.5 & \text{tr}(\epsilon_z) < 0 \\ 1.0 & \text{tr}(\epsilon_z) \geq 0 \end{cases} \quad (17)$$

in which the parameter  $\alpha$  was empirically determined [80]. The notation  $\text{Max/Min}_n^z$  indicates the operation is applied to cells  $n$  surrounding cell  $z$ . The limiter  $\beta$  is determined by equating the projection to the bounds

$$\tilde{u}_\pm^k = \tilde{u}_c^k = \tilde{u}_z^k + \beta_\pm^k (\delta_C \tilde{u}^k - \Delta \tilde{u}^k)$$

and constraining the range from 0 to 1. Then

$$\beta_\pm^k = \frac{\tilde{u}_\pm^k - \tilde{u}_z^k}{\delta_C \tilde{u}^k - \Delta \tilde{u}^k}$$

$$\beta^k = \max \{0, \min [1, \beta_+^k, \beta_-^k]\}$$

From this, the limited corner projection is

$$\tilde{u}_c^k = \tilde{u}_0^k(\beta^k) + \beta^k \delta_C \tilde{u}^k$$

and its global representation  $u_c^k$  can be evaluated and used in the approximate Riemann solution.

#### 4.3. Stress

In the case of stress, we adapt the scheme of [13, 90] in which monotonicity is imposed on rotational invariants of the stress tensor. The stress tensor itself is decomposed into isotropic and deviatoric components

$$q = \frac{1}{3} \text{tr}(\sigma)$$

$$\sigma^{kl} = q \delta^{kl} + s^{kl}$$

with the former being the mean stress (negative of pressure) and  $\delta^{kl}$  being the Kronecker delta. Within a cell corner, the reconstructed components are

$$q(x) = q_0 + \beta^1 (x^j - x_z^j) \partial_p^j q$$

$$s^{kl}(x) = s_0^{kl} + \beta^2 (x^j - x_z^j) \partial_p^j s_z^{kl}$$

again with  $q_0$  and  $s_0^{kl}$  to be determined from the conservation constraint.

*Conservation.* Again, referring to Figure 8(a), the projections from the cell centroid  $z$  to corner centroid  $d$  are

$$\begin{aligned} q_d &= q_0 + \beta^1 \delta_d q \\ s_d^{kl} &= s_0^{kl} + \beta^2 \delta_d s^{kl} \\ \delta_d q &= (x_d^j - x_z^j) \partial_p^j q \\ \delta_d s^{kl} &= (x_d^j - x_z^j) \partial_p^j s_z^{kl} \end{aligned}$$

in which  $\beta^m$  is a slope limiter for the entire cell and  $x_d^j$  the centroid of the corner subcell. Again, the extensive quantity in a cell corner is given by the corner volume times the value at the corner centroid

$$\begin{aligned} \int_c q(x) dV &= V_c (q_0 + \beta^1 \delta_d q) \\ \int_c s^{kl}(x) dV &= V_c (s_0^{kl} + \beta^2 \delta_d s^{kl}) \end{aligned}$$

Then for the entire cell

$$\begin{aligned} q_z V_z &= \int_z q(x) dV = V_z (q_0 + \beta^1 \Delta q) \\ s_z^{kl} V_z &= \int_z s^{kl}(x) dV = V_z (s_0^{kl} + \beta^2 \Delta s^{kl}) \\ \Delta q &= \frac{1}{V_z} \sum_c V_c \delta_d q \\ \Delta s^{kl} &= \frac{1}{V_z} \sum_c V_c \delta_d s^{kl} \end{aligned}$$

and the stress at the cell centroid  $z$  is related to the limiters by

$$\begin{aligned} q_0(\beta^1) &= q_z - \beta^1 \Delta q \\ s_0^{kl}(\beta^2) &= s_z^{kl} - \beta^2 \Delta s^{kl} \end{aligned}$$

again with  $\beta^1$  and  $\beta^2$  to be determined from the monotonicity constraint.

*Monotonicity.* The limiting is done in terms of the first and second rotational invariants (the third invariant provides no additional constraints) defined by the functions

$$Y^1(\sigma) = q \tag{18}$$

$$Y^2(\sigma) = \sqrt{3s : s/2} \tag{19}$$

The invariants are calculated for all cells

$$y_z^m = Y^m(\sigma_z)$$

Let the set of cells including cell  $z$  itself and its first and second nearest neighbors be indexed by  $n$ . The invariant bounds for cell  $z$  are

$$\begin{aligned} y_z^m &= \text{Max/Min}_n^z [\alpha y_n^m + (1 - \alpha) y_z^m] \\ \alpha &= \begin{cases} 0.5 & \text{tr}(\varepsilon_z) < 0 \\ 1.0 & \text{tr}(\varepsilon_z) \geq 0 \end{cases} \end{aligned}$$

Projected from the cell centroid  $z$ , the unlimited stress tensor (subscripted  $C$ , not  $c$ ) is calculated for each corner

$$\begin{aligned}\sigma_C^{kl} &= \sigma_0^{kl} + \delta_C \sigma^{kl} \\ \delta_C \sigma^{kl} &= (x_p^i - x_z^i) \partial_p^i \sigma^{kl}\end{aligned}$$

The unlimited invariants are calculated

$$y_C^m = Y^m(\sigma_C^{kl})$$

The stress difference is decomposed into isotropic and deviatoric components

$$\delta_C \sigma^{kl} \rightarrow \{\delta_C q, \delta_C s^{kl}\}$$

Again, the limiter is determined by equating the projection to the bounds

$$y_\pm^m = y_c^m = y_z^m + \beta_\pm^m (y_C^m - y_z^m)$$

and constraining to the range  $[0,1]$ , so that

$$\begin{aligned}\beta_\pm^m &= \frac{y_\pm^m - y_z^m}{y_C^m - y_z^m} \\ \beta^m &= \max\{0, \min[1, \beta_+^m, \beta_-^m]\}\end{aligned}$$

The isotropic and deviatoric components of the limited projection of the stress tensor are then

$$\begin{aligned}q_c &= q_0 + \beta^1 \delta_C q \\ &= q_z + \beta^1 (\delta_C q - \Delta q) \\ s_c^{kl} &= s_0^{kl} + \beta^2 \delta_C s^{kl} \\ &= s_z^{kl} + \beta^2 (\delta_C s^{kl} - \Delta s^{kl})\end{aligned}$$

and the stress tensor projected to the node is

$$\sigma_c^{kl} = s_c^{kl} + q_c \delta^{kl}$$

This completes the description of the CGR reconstruction.

## 5. Smooth flow problems

The principal objective of the test problems presented is to compare the CCH2 and CGR methods in a wide variety of situations. In particular, we wish to consider problems with and without shocks, with and without vorticity, Lagrange and ALE (Eulerian), gases and solids, rectangular and polar grids, planar (XY) and cylindrical (RZ) geometry, and 1D, 2D, and 3D. The test matrix is shown in Table 1. In the table, planar 1D problems are designated 1D, but set up as 2D. The order of presentation is smooth flow, shocks, and ALE.

*Material parameters.* In the test problems, gases are represented with a polytropic gas equation of state, while solids use a Grueneisen equation of state with an elastic-plastic constitutive model described in Appendix A. For most of the problems, the parameters are specified for a units system of  $\{g, cm, \mu s\}$ .

*CGR parameters.* Unless otherwise noted, all problems were run with the following parameters.

- $\eta = 0.05$  in Equation 13 was used in most cases to avoid a possible singularity in the Riemann solution for velocity. However, because the flow in the Noh problem of Section 6.2 becomes stationary, we set  $\eta$  to a large number to force the use of the corner normal. This was also done for the adiabatic release problem of Section 6.5.

Problem	Dim	Geom	Mesh	Hydro	Material	Flow
Be plate	2D	XY	Square	Lag	Elastic	Smooth
Taylor-Green	2D	XY	Square	Lag	Gas	Smooth+vorticity
Coggeshall	2D	XY	Square	Lag	Gas	Smooth
	3D	XYZ	Square	Lag	Gas	Smooth
Kidder shell	2D	RZ	Polar	Lag	Gas	Smooth
	3D	XYZ	Special	Lag	Gas	Smooth
Kidder ball	2D	RZ	Square	Lag	Gas	Smooth
Howell	2D	XY	Polar	Lag	EP	Smooth
Verney	2D	RZ	Polar	Lag	EP	Smooth
	3D	XYZ	Geo	Lag	EP	Smooth
Taylor Anvil	2D	RZ	Square	Lag	EP+hardening	Shock+smooth
Sod	2D	XY	Rect	Lag	Gas	Shock
Noh	2D	XY	Polar	Lag	Gas	Shock
	2D	RZ	Polar	Lag	Gas	Shock
	2D	XY	Square	Lag	Gas	Shock
	2D	RZ	Square	Lag	Gas	Shock
	3D	XYZ	Square	Lag	Gas	Shock
Sedov	2D	XY	Square	Lag	Gas	Shock
	2D	RZ	Square	Lag	Gas	Shock
	3D	XYZ	Square	Lag	Gas	Shock
Saltzman	2D	XY	Special	Lag	Gas	Shock
	2D	RZ	Special	Lag	Gas	Shock
	3D	XYZ	Special	Lag	Gas	Shock
Adiabatic rel	1D	X	Rect	Lag	Gas	Shock+release
EP piston	1D	X	Rect	Lag	EP	Shock
Triple point	2D	XY	Square	ALE	Gas	Shock+vorticity
He bubble	2D	RZ	Rect	ALE	Gas	Shock+vorticity

Table 1: Testing matrix ordered by smooth flow, shock, and ALE problems. Abbreviations: 1D=run on a 2D mesh, Lag=Lagrange, ALE=arbitrary Lagrange-Euler, Geo=geodesic mesh, Rect=rectangular, EP=elastic plastic solid.

- $\lambda = 0.25$  in Equation 15 to mix LSQ point and corner gradients. The need for this is demonstrated in the Taylor anvil calculations of Figure 28 in Section 5.7.
- The  $s$  term in the shock velocity of Equation 10 is set to zero in all problems but as described in Figure 32. We found it either to have negligible effect or to give rise to increased dissipation for the problems considered in the test suite.
- $\alpha$  as in Equation 17 to impose different monotonicity bounds in compression and expansion. This was the only parameter that was systematically changed depending upon the type of problem. For problems with shocks such as the adiabatic release problem of Section 6.5, we found that  $\alpha(\text{compression})=0.5$  significantly reduced the error. However, in smooth flow problems with vorticity, such as the Taylor anvil of Section 5.7, we found that  $\alpha=1$  produced better results. This suggests a modification of the Barth-Jespersen limiter to better detect shocks as an area for future study.

*Convergence.* For some problems, we cite a convergence rate. Given a plot of (log of an error metric) vs. (log of a measure of the cell size), the cited convergence rate is the slope of the trend line. In most cases, the error metric is the  $L_1$  error norm of the form

$$L_1 = \frac{1}{N} \sum_i^N \|\mathbf{u}_i - \mathbf{u}_0\|$$

in which  $\mathbf{u}_0$  is the reference value. In some cases, we volume/area weight the norm.

### 5.1. Bending plate

Thin beams or plates have been the subject of many test problems, see for example [41]. The problem, discussed in Section 1, differs in that it is a thick plate with free boundaries. The problem has been previously analyzed using PAGOSA [111, 112], a three-dimensional Eulerian code. Here the problem is solved in a Lagrangian framework as described in [91]. This is a two dimensional problem comprised of an elastic beryllium plate with no supports or constraints. The domain is  $[-3, +3]$  in the  $x$  direction and  $[-0.5, +0.5]$  in the  $y$ . The centerline of the plate initially coincides with the  $x$ -axis. The plate is prescribed with an initial velocity distribution as given by

$$\dot{y}(x, t) = A\omega \left\{ \begin{array}{l} g_1 [\sinh \Omega(x+3) + \sin \Omega(x+3)] \\ + g_2 [\cosh \Omega(x+3) + \cos \Omega(x+3)] \end{array} \right\} \cos(\omega t)$$

with initial velocity computed at  $t = 0$ . When subject to this initial velocity distribution, the plate begins to oscillate elastically. For the given dimensions and material parameters of the bar,

$$\rho = 1845 \text{ kg/m}^3$$

$$Y_0 = 1.0 \text{ Mb}$$

$$k = 1.18896 \text{ Mb}$$

$$E = 3.182656 \text{ Mb}$$

$$\nu = 0.053896$$

where  $k$ ,  $E$ , and  $\nu$  are the bulk modulus, elastic modulus and Poissons ratio respectively. The yield stress for the material is set at a very high value so that the plate oscillates elastically.

There is no analytic solution for a thick plate as specified for this problem. However, for a thin unconstrained plate, the solution for the first flexural mode is

$$y(x, t) = A \left| \begin{array}{l} g_1 [\sinh \Omega(x+3) + \sin \Omega(x+3)] \\ - g_2 [\cosh \Omega(x+3) + \cos \Omega(x+3)] \end{array} \right| \sin(\omega t)$$

in which

$$\Omega = 0.7883401241 \text{ cm}^{-1}$$



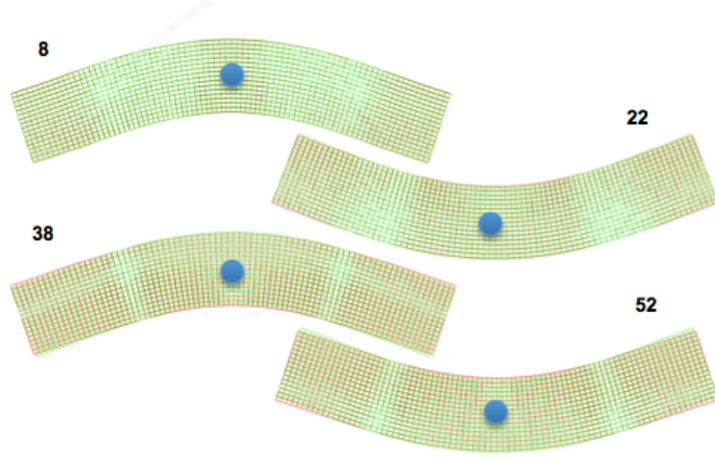


Figure 10: Bending plate. Large deformation of a Be plate at times near maxima of displacement. Blue dots indicate the location of the central point.

is the first non-zero root of  $[\cosh(6\Omega) \cos(6\Omega)] = 1$ . The coefficients and angular frequency are given by

$$\begin{aligned} g_1 &= \cosh(6\Omega) - \cos(6\Omega) = 56.63685154 \\ g_2 &= \sinh(6\Omega) - \sin(6\Omega) = 57.64552048 \\ \omega &= \Omega^2 \Delta y \sqrt{\frac{E}{12\rho(1-\nu^2)}} = 0.2359739922 \mu\text{s}^{-1} \end{aligned}$$

in which  $\Delta y$  is the thickness of the plate. Then, the first flexural mode has a period of  $\tau = 2\pi/\omega = 26.6266 \mu\text{s}$ . For a maximum displacement of  $0.5 \text{ cm}$  at the ends of the plate, the constant  $A$  is given by

$$A = \frac{1}{2} \left( \frac{y_{\max}}{g_2} \right) = 0.004336850425 \text{ cm}$$

Lacking an analytical solution for a thick plate, we use an SGH calculation as a reference in which all artificial viscosities were set to zero to produce a result without dissipation. Figure 10 shows the large deformation of the plate at times near maxima of displacement. Figure 11 compares the vertical velocity of the central point for three calculations. The reference SGH calculation (green) has high frequency oscillations corresponding to the acoustic transit time across the thickness of the plate. The observed period of about  $30 \mu\text{s}$  differs from the first flexural mode, but is in agreement with that reported by others [112, 91]. The CCH2 result (black) previously discussed in Section 1 shows reduced amplitude in the major oscillations indicating irreversible conversion of kinetic to internal energy. The CGR result (red) maintains a uniform amplitude and is smoother than the undamped reference calculation.

## 5.2. Taylor-Green vortex

This 2D problem was discussed by Taylor [98] and has been revisited since by many researchers since [35, 34]. The problem is also discussed in [54]. The problem is of particular interest because it represents a vortical flow problem for which there is a known solution. We take our description of the problem from Reference [34]. The material is a polytropic gas with  $\gamma = 5/3$  and unity density. The domain is a unit square with reflecting boundary conditions on each face. The initial velocity conditions consist of a sinusoidal variation

$$u(x, y) = \{\sin(\pi x) \cos(\pi y), -\cos(\pi x) \sin(\pi y)\}$$

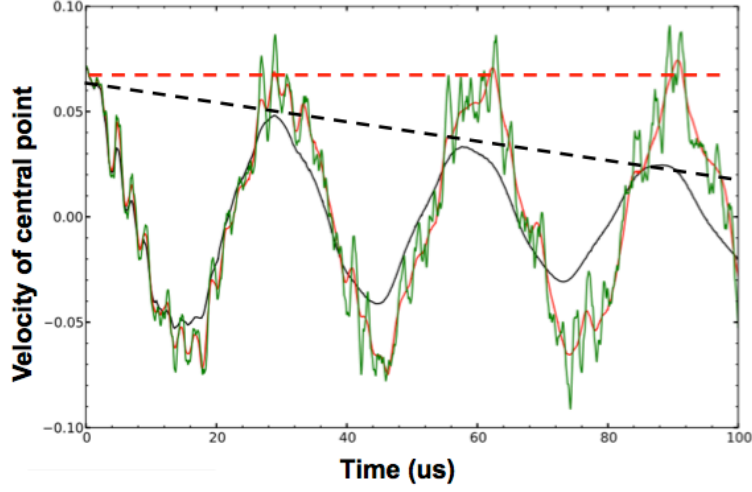


Figure 11: Bending plate. Vertical velocity of the central point in a bending Be plate showing the reduced dissipation in the CGR result (red) relative to the CCH2 result (black). Undamped reference in green. The dashed red and black lines contrast the trends in CGR and CCH2 respectively.

corresponding to a counterclockwise flow whose magnitude should remain constant in time. The initial pressure is given by

$$p(x, y) = \frac{\rho}{4} [\cos(2\pi x) + \cos(2\pi y)] + 1$$

In addition, the problem has an energy source term because the fluid, as modeled, is compressible

$$\dot{e} = \frac{3\pi}{8} [\cos(3\pi x) \cos(\pi y) - \cos(\pi x) \cos(3\pi y)]$$

Because of the large deformation, Lagrangian calculations can only be run for short times. Figure 12(a) shows an initial 60x60 mesh. Figures 12(b) and (c) compare the CCH2 and CGR meshes at  $t=0.5$ . The CGR result shows a smooth deformation through the central region while that of CCH2 is distorted. Figures 12 (d) and (e) compare the velocity fields at  $t=0.5$ . The red contours in the CCH2 calculation show both a loss of amplitude and also loss of symmetry that is not apparent in the CGR result. The central green region is rotated in the CCH2 calculation, but not in the CGR one. Also, the central blue region in the CCH2 calculation is becoming square but remains circular in the CGR calculation.

Convergence calculations were run at resolutions of 10x10, 20x20, 40x40, and 80x80 and compared at  $t = 0.25$ . The L1 norms for density and pressure are given in Table 2 and plotted in Figure 13. The density convergence rates for CCH2 (blue) and CGR (red) were respectively 0.993 and 2.585. Those for pressure were 1.011 and 2.579.

### 5.3. Coggeshall problem

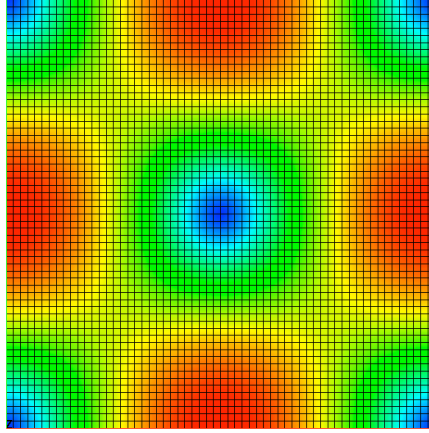
The spherical Coggeshall problem [29] describes the adiabatic compression of a polytropic gas with  $\gamma = 5/3$ . It is similar to the Noh problem of Section 6.2 except the initial velocity is equal to the negative of the radius instead of unity. The initial conditions are

$$\{u_0, \rho_0, e_0\} = \{-r_0, 1.0, 10^{-6}\}$$

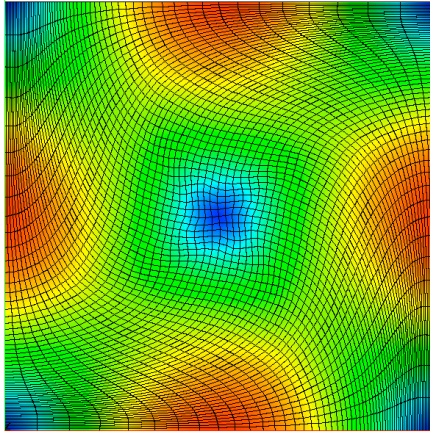
in which  $r_0$  is the initial radius. The calculation is run to a time of 0.6 on a square 50x50 mesh in 2D XY geometry and on a 50x50x50 mesh in 3D planar geometry.

The analytic solution is given by

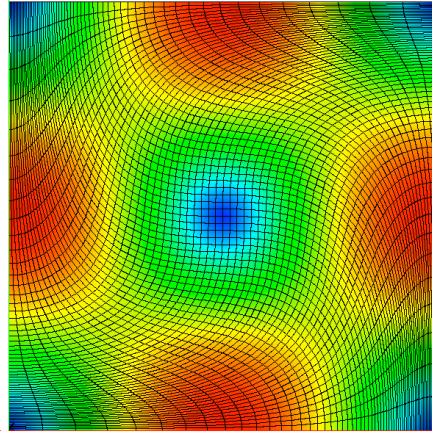
$$\begin{aligned} u(t) &= u_0 \\ r(t) &= r_0 (1 - t) \\ \rho(t) &= \rho_0 (1 - t)^{-\alpha} \\ e(t) &= e_0 (1 - t)^{-\alpha(\gamma-1)} \end{aligned}$$



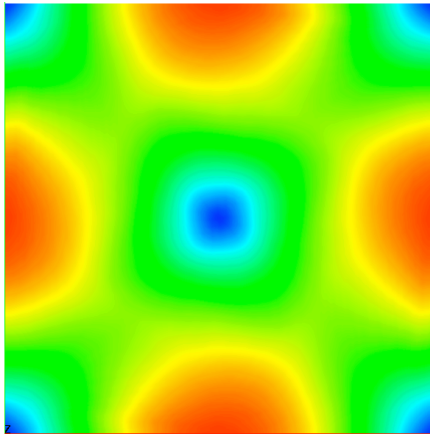
(a)  $t=0.0$



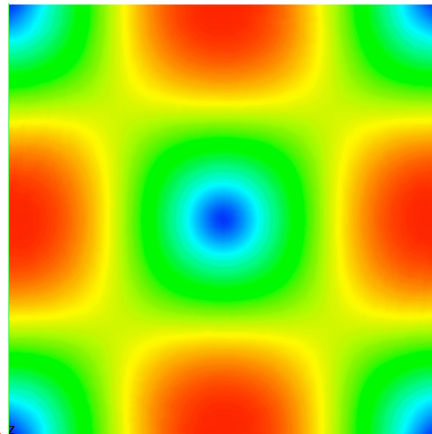
(b) CCH2 mesh,  $t=0.5$



(c) CGR mesh,  $t=0.5$



(d) CCH2 velocity,  $t=0.5$



(e) CGR velocity,  $t=0.5$

Figure 12: 2D Taylor-Green vortex. (a) Initial Lagrangian 60x60 mesh. At  $t=0.5$ , (b) CCH2 mesh, (c) CGR mesh, (d) CCH2 velocity field, (e) CGR velocity field. Colors represent velocity magnitude on a scale of 0 to 1 and should remain stationary in time.

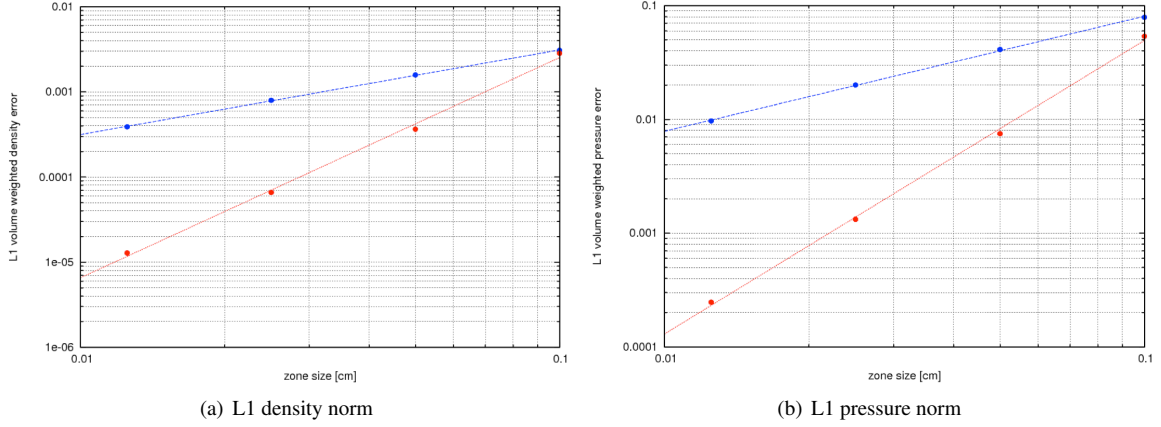


Figure 13: Taylor Green vortex. Convergence plots at  $t = 0.25$ . Density convergence rates were 0.993 (CCH2 blue) and 2.585 (CGR red). Pressure convergence rates were 1.011 (CCH2 blue) and 2.579 (CGR red).

	Cell size	L1 density	L1 pressure
CCH2	0.1	3.0775e-3	7.9062e-2
	0.05	1.5833e-3	4.1129e-2
	0.0250	7.9672e-4	2.0082e-2
	0.0125	3.8956e-4	9.7074e-3
CGR	0.1	2.8460e-3	5.37403e-2
	0.05	3.6488e-4	7.4883e-3
	0.025	6.5975e-5	1.3234e-3
	0.0125	1.2815e-5	2.4702e-4

Table 2: Taylor Green vortex. L1 volume-weighted density and pressure norms at  $t = 0.25$  for CCH2 and CGR.

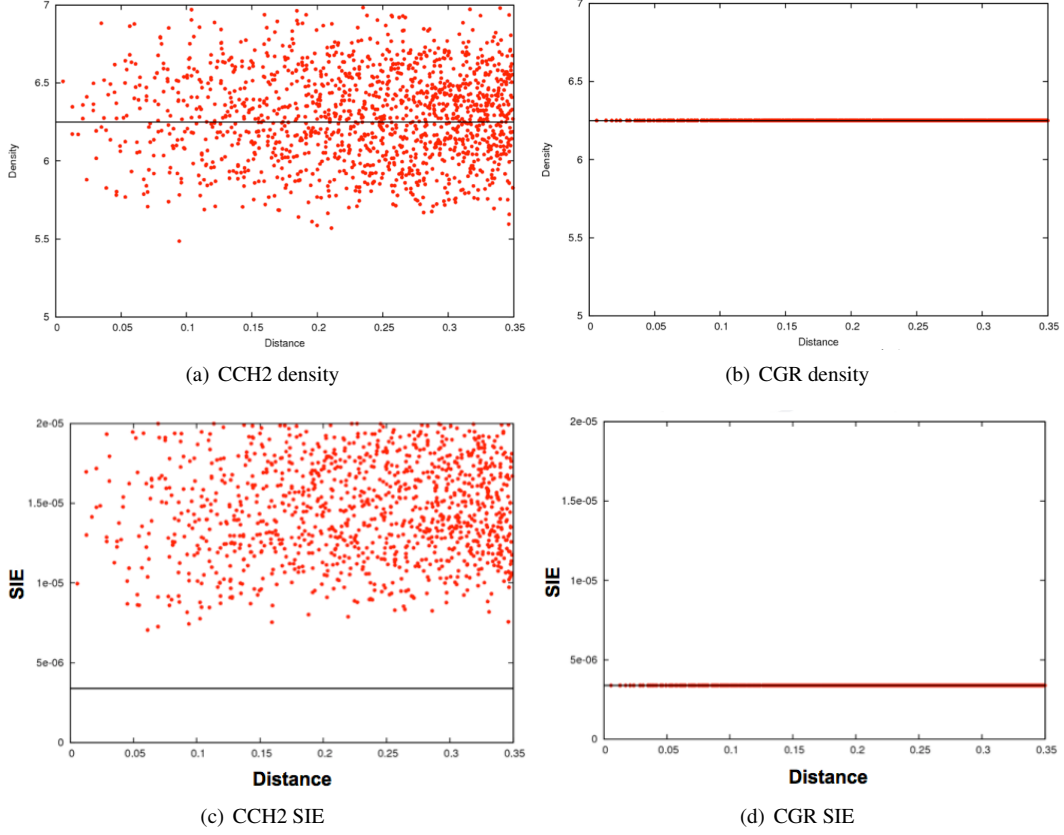


Figure 14: Coggeshall XY ( $\alpha = 2$ ). Scatter plots of density and SIE vs. distance comparing CCH2 and CGR. The vertical scales are the same. Analytic result is in black.

in which  $\alpha = \{1, 2, 3\}$  respectively for planar, cylindrical, or spherical geometry.

Because the specific internal energy (SIE) is small and the velocity large, small errors in the velocity solution give rise to large errors in the thermodynamic variables. This is apparent in Figures 14(a) and (b) are scatter plots (one dot per cell) of density vs. distance for CCH2 and CGR. The CCH2 result has a large scatter, whereas the CGR is in excellent agreement with the analytic result. The same is seen in Figures 14(c) and (d) that compare the specific internal energies.

Figure 15 compares 3D calculations for CCH2 (a) and CGR (b). The same trend as in 2D is observed. Figure (c) is a CGR result without auxiliary ghost cells discussed in Section 4.1 and clearly shows a slight perturbation near the origin. Figure 16 shows the SIE plotted on the surface of the mesh. The CGR result is uniform whereas the CCH2 result is scattered.

#### 5.4. Kidder shell

Kidder [57, 55, 56, 88] derived a series of exact solutions for the isentropic compression of a gas. In this section, we calculate the isentropic compression of a hollow shell of gas [56]. This test problem has been calculated in other hydrodynamic papers including [70, 6, 25, 109, 82]. Time-varying boundary conditions on the inner and outer surfaces cause the shell to compress. The goal of the Kidder hollow shell test problem is to assess the ability of the method to produce symmetric and non-dissipative results. The test problem is isentropic, so no dissipation should be generated.

The equation of state is a polytropic gas with gamma equal to 5/3. The initial conditions of this test problem are as follows. The initial inner and outer radii of the shell are  $r_1^0 = 0.9$  cm and  $r_2^0 = 1.0$  cm respectively. The subscripts 1 and 2 denote the inner and outer surfaces and the super script 0 denotes the initial time. The initial density on the inner and outer surfaces are  $\rho_1^0 = 1$  g/cc and  $\rho_2^0 = 2$  g/cc. The initial density, pressure, and velocity distributions in the

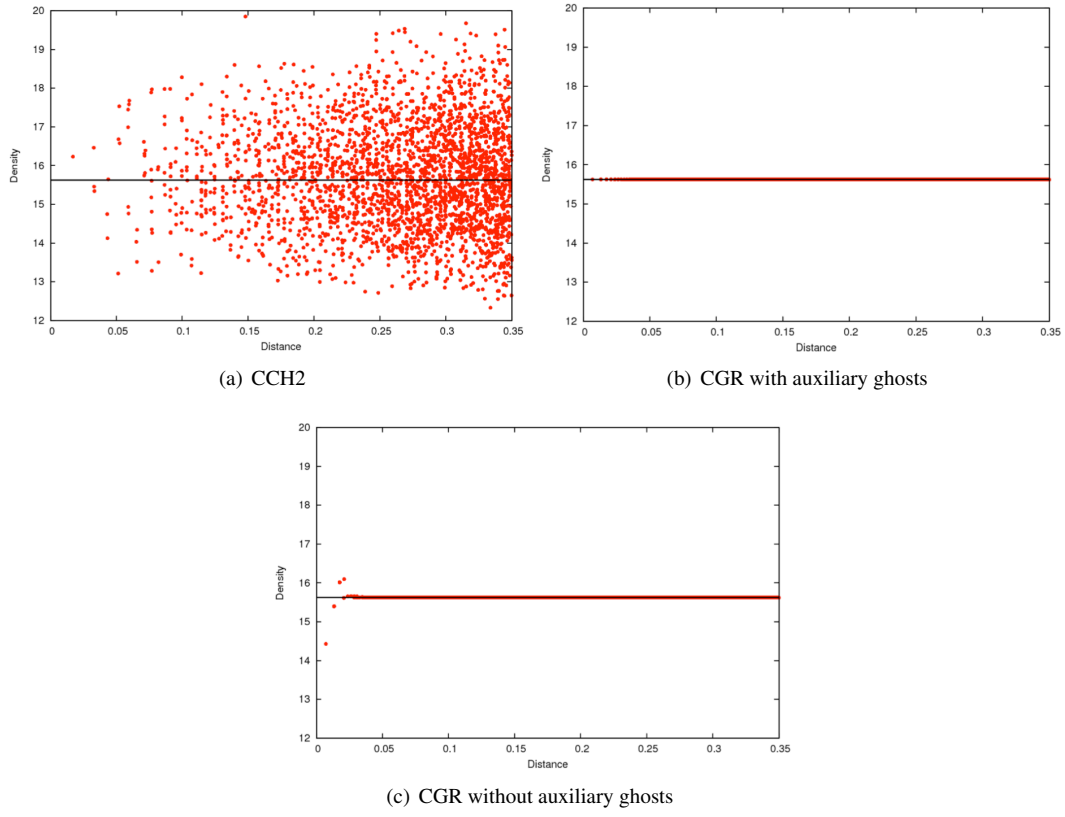


Figure 15: 3D Coggeshall ( $\alpha = 3$ ). Scatter plots of density vs. radius. The vertical scales are the same. Analytic result is in black.

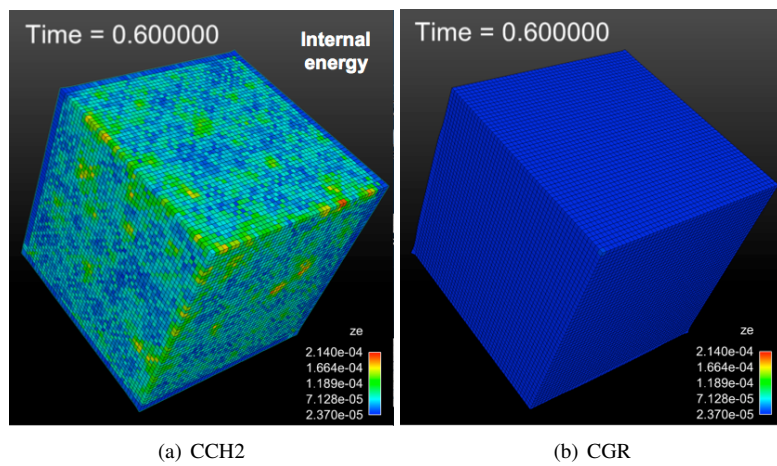


Figure 16: 3D Coggeshall. SIE plotted on the surface of the mesh. CCH2 and CGR have the same color scales, but the former is noisy.

shell are functions of radius given by

$$\begin{aligned}\rho^0(r) &= \left( \frac{r_2^2 - r^2}{r_2^2 - r_1^2} \rho_1^{\gamma-1} + \frac{r^2 - r_1^2}{r_2^2 - r_1^2} \rho_2^{\gamma-1} \right)^{\frac{1}{\gamma-1}} \\ p^0(r) &= \rho^0(r)^\gamma \\ u^0(r) &= 0\end{aligned}\tag{20}$$

The analytic solution for the density, pressure, and velocity as a function of the radius and time are

$$\begin{aligned}\rho(r(t), t) &= \rho^0(r^0) h(t)^{\frac{-2}{\gamma-1}} \\ p(r(t), t) &= p^0(r^0) h(t)^{\frac{-2\gamma}{\gamma-1}} \\ u(r(t), t) &= r^0 \frac{dh(t)}{dt}\end{aligned}\tag{21}$$

The radius varies with time according to

$$r(t) = r^0 h(t)\tag{22}$$

The analytic solutions in Eq. (21) and the radius are functions of the initial radius  $r^0$  and a non-dimensional variable  $h(t)$  given by

$$h(t) = \sqrt{1 - \frac{t^2}{\tau^2}}\tag{23}$$

where  $\tau$  is the focusing time (when  $h$  vanishes) and is given by

$$\tau = \sqrt{\frac{(\gamma - 1) \left[ (r_2^0)^2 - (r_1^0)^2 \right]}{2(c_2^2 - c_1^2)}}\tag{24}$$

The sound speed  $c$  is given by  $c = \sqrt{\gamma p / \rho}$ . The derivative with respect to time of the variable  $h$  is

$$\frac{dh(t)}{dt} = \frac{t}{\tau^2} \frac{1}{h(t)}\tag{25}$$

The simulation is calculated to a time of  $t_{final} = \frac{\sqrt{3}}{2}\tau$ , which corresponds to an inner and outer radius of 0.45 and 0.5 cm. The initial conditions are given by Eq. 20 and time-dependent pressure boundary conditions are applied to the inner and outer surfaces also according to Eq. (21). Unlike the analytical problem, pressure boundary conditions cause the numerical problem to be hydrodynamically unstable. That is, there is no mass outside the boundary, so that the effective Atwood number is unity at the surfaces. In particular, the outer surface is Rayleigh-Taylor (RT) unstable, while the inner is RT stable. This causes numerical perturbations on the outer surface to grow with time and eventually affect the solution on the inner surface. As a high degree of symmetry can be achieved by 2D equiangular meshes and the RZ formulation described in [15], the boundary conditions can be applied directly to both surfaces without strongly affecting the 2D solution.

However, there exists no completely symmetrical tessellation of a sphere in 3D, and the 3D solution is strongly affected by perturbations on the outer surface. There are several possible solutions to this issue that maintain the spirit of the test problem. We elected to simply move the instability away from the surfaces of interest by applying the appropriate pressure boundary condition (also derived from Eq. 21) at an outer radius initially at 1.1 cm. No change was made at the inner surface because it was RT stable.

In 2D, we used 90-degree polar meshes consisting of 12x24, 24x48, 48x96, 96x192, and 192x384 radial by angular cells. In 3D, the shell was assembled in an octant from three logically rectangular blocks. We considered 3 resolutions for the blocks: 10x10x10, 20x20x20, and 40x40x40. In Figure 17(a), we show the initial (yellow) and final (green) meshes for the 12x24 2D calculation. In Figure 17(b-d), we show that portion of the 20x20x20 3D mesh initially between 0.9 and 1.0 cm, omitting the portion between 1.0 and 1.1 cm. The CCH2 and CGR results are indistinguishable on this scale, so that only the CGR meshes are shown.

The calculated inner and outer radii closely follow the analytic solution in time as shown in Figure 18 for 2D (a and c) and 3D (b and d). In 2D, the CCH2 (blue) and CGR (red) results are indistinguishable, but differ slightly in



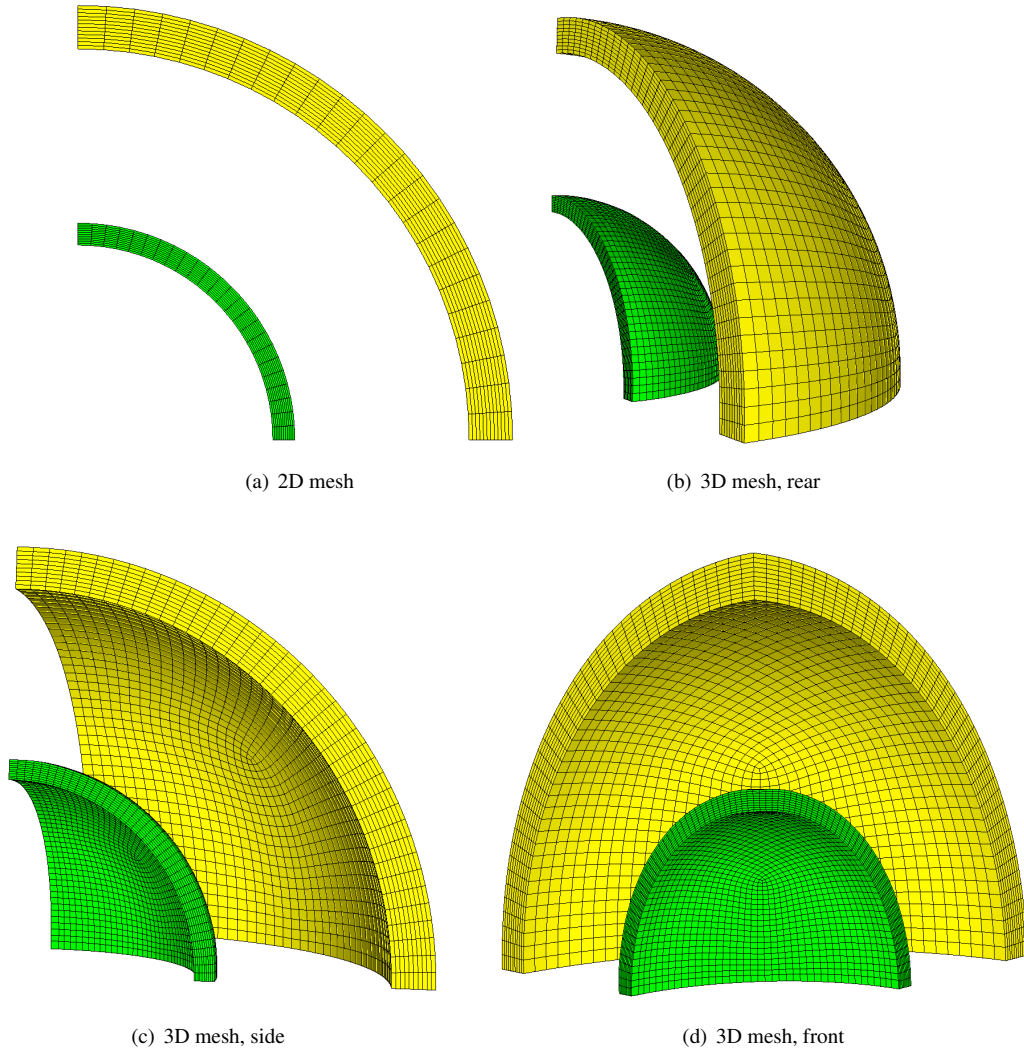


Figure 17: Kidder shell initial (yellow) and final (green) meshes. 2D 12x24 mesh (a) and 3 orientations (b-d) of the 20x20x20 mesh. The CCH2 and CGR results are indistinguishable on this scale, so that only the CGR are shown.



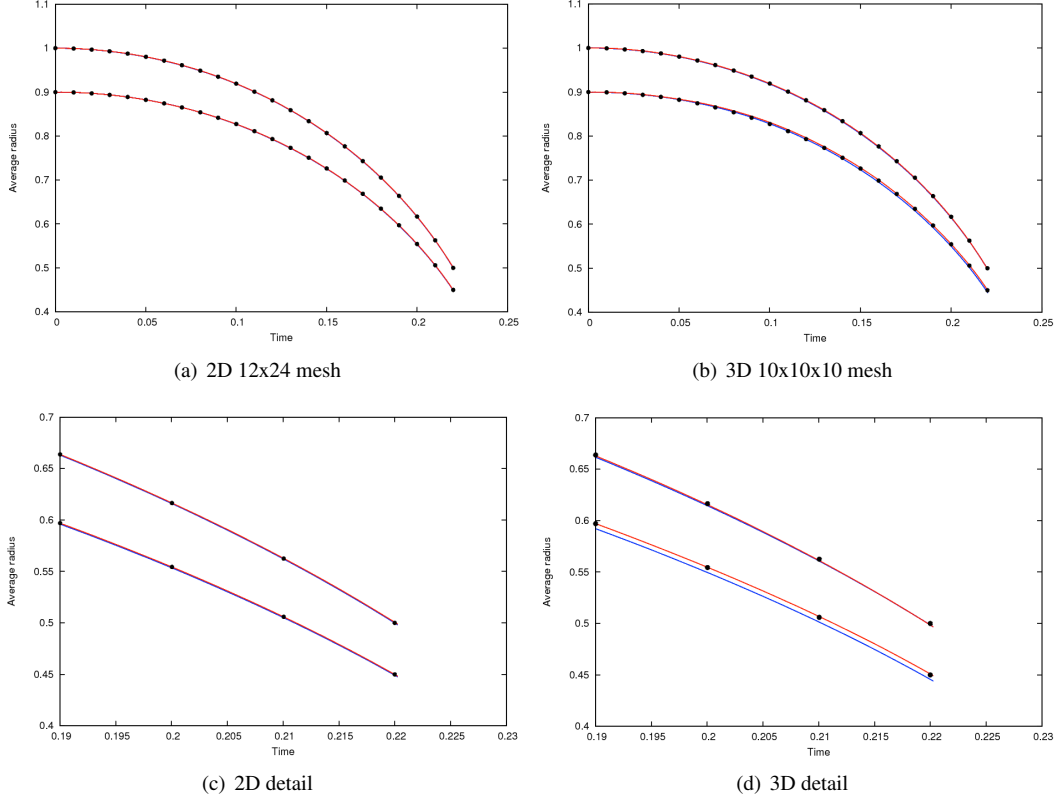


Figure 18: Kidder shell inner and outer radii vs. time for the coarsest meshes. In each figure, the upper curve corresponds to the outer surface, and the lower to the inner. The analytical results are indicated by black dots. 2D is left and 3D right. In 2D, the CCH2 (blue) and CGR (red) results are indistinguishable, but differ slightly in 3D.

3D with CGR being closer to the analytical results. The final radii are given in Table 3 along with the convergence rates. The convergence plots are given in Figure 19. Although the error was small, the 2D CCH2 calculations did not converge because of the aforementioned instabilities. The other convergence rates ranged from about 1.75 to 2.24. The percent RMS deviation from sphericity is calculated as

$$\bar{r} = \frac{1}{n} \sum_i^n r_i$$

$$pct = \frac{100}{n\bar{r}} \sqrt{\sum_i^n (r_i - \bar{r})^2}$$

with the sum being over boundary points. Figure 20(b) compares the deviation of the inner (heavy) and outer (light) surfaces for CCH2 (blue) and CGR (red). The deviation for 2D CGR is notable because it remains near machine precision for most of the calculation, increasing for the outer surface only near the completion time. Other deviations tend to increase at late time as  $t^2$  as might be expected from fluid instability theory.

### 5.5. Kidder ball

The Kidder shell analytic solution in the previous subsection goes to infinity when the inner surface reaches the origin (e.g. Eq. (21) gives  $\rho_1(0, \tau) = p_1(0, \tau) = u_1(0, \tau) = \infty$ ), so the accuracy of the method was quantified on the implosion phase up to a time of  $t_{final} = \frac{\sqrt{3}}{2}\tau$ . Given this, we calculate another isentropic compression problem that is valid for all time and is based on the work of Kidder and Coggeshall [28, 88]. This test problem is a sphere of gas that

	Cell thickness	Inner CCH2	Outer CCH2	Inner CGR	Outer CGR
2D	0.01	0.447475	0.498090	0.448188	0.498775
	0.005	0.449454	0.499779	0.449544	0.499686
	0.0025	0.449893	0.500293	0.449884	0.499919
	0.00125	0.449975	0.500685	0.449970	0.499979
	0.000625	0.449960	0.501841	0.449992	0.499994
	Rate	2.2366	-	1.9668	1.9172
3D	0.02	0.443937	0.496704	0.449209	0.496636
	0.01	0.448588	0.499531	0.449689	0.499113
	0.005	0.449679	0.500062	0.449930	0.499769
	Rate	2.1202	2.8615	1.7497	1.9320

Table 3: 2D and 3D Kidder shell inner and outer radii at  $t=0.22027$  for CCH2 and CGR. Convergence rates are also tabulated.

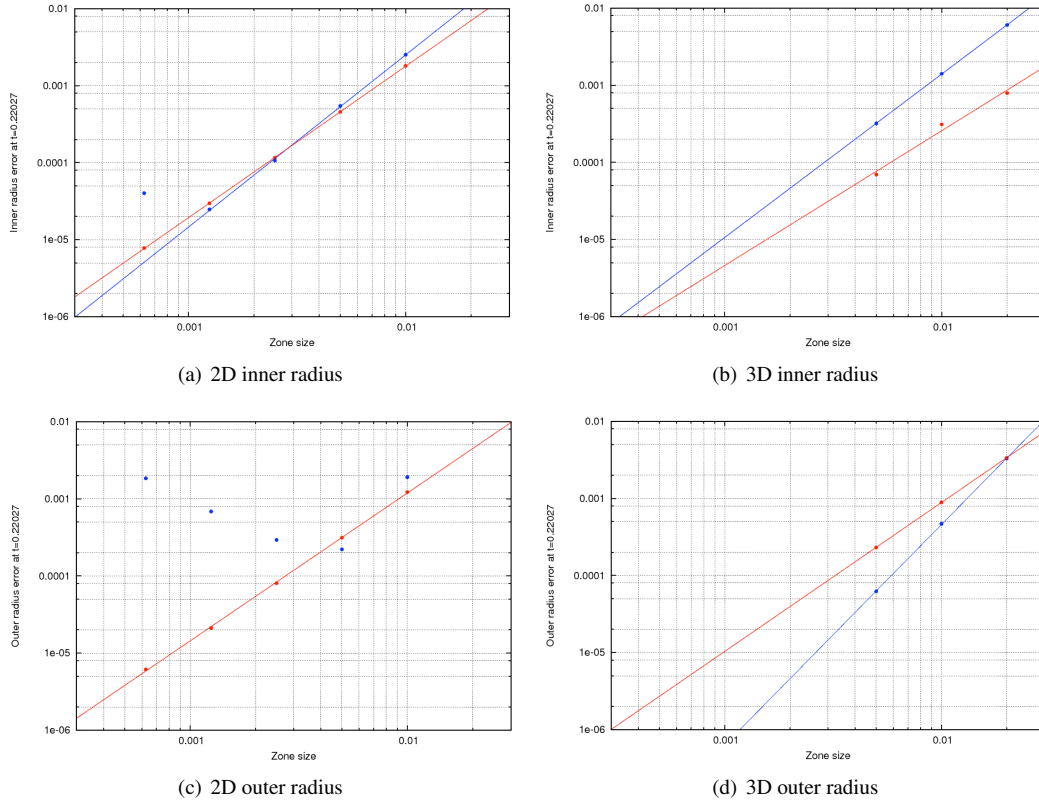


Figure 19: Kidder shell convergence on the inner and outer radii. CCH2 (blue) and CGR (red). Note that the 2D CCH2 calculations did not converge.

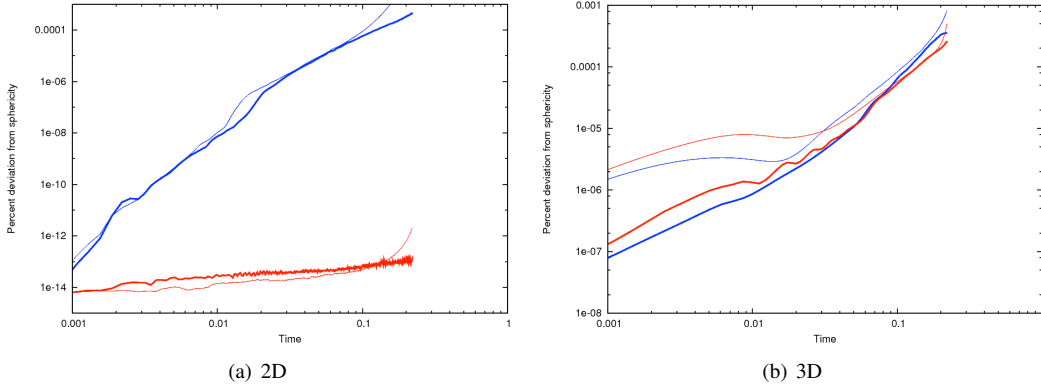


Figure 20: Kidder shell. Percent RMS deviation from sphericity vs. time for 2D resolution 96x192 and 3D resolution 40x40x40. Results for other resolutions are similar. CCH2 (blue) and CGR (red). The lighter curves correspond to the outer surface and the heavier to the inner. The deviation for 2D CGR is notable because it remains near machine precision for the duration of the calculation. Other deviations tend to increase at late time as  $t^2$  as might be expected from fluid instability theory.

is isentropically compressed and is termed the Kidder ball problem to distinguish it from the Kidder shell problem in the previous subsection. The chief goal of the Kidder ball problem is to assess the ability of the hydrodynamic method to reach the theoretical maximum compression, which occurs at the origin. This test problem is isentropic so dissipation errors will artificially reduce the peak compression. Another goal is to demonstrate symmetry preservation. The equation of state is a polytropic gas with gamma equal to 5/3. The initial conditions are as follows: an initial inward linear velocity profile, a Gaussian density profile, and a constant internal energy. The initial velocity profile is  $u = -r/2$ , the initial density profile is  $\rho = \frac{1}{\sqrt{2}} \exp(-r^2/2)$ , and the initial internal energy is 3/8. The analytic solution for the density, radial velocity, and specific internal energy is provided below as a function of time,  $t$ , and radius,  $r$ .

$$\begin{aligned}\rho &= 2\left(1 + (t-1)^2\right)^{-\frac{3}{2}} \exp\left(-\frac{r^2}{1+(t-1)^2}\right) \\ u &= \frac{r(t-1)}{1+(t-1)^2} \\ e &= \frac{\frac{3}{2}}{1+(t-1)^2}\end{aligned}\tag{26}$$

The units are g, cm, and  $\mu s$ . The radial velocity above is applied to the nodes on the outer surface, so this problem can be viewed as a spherical piston. The calculated solution will be compared to the analytic solution.

The problem was modeled in 2D using a rectangular domain of  $(x, y) \in [-3, 3] \times [0, 3]$  with mesh resolutions of 5x10, 10x20, 20x40, 40x80, 80x160, 160x320, and 320x640. The calculation was run to a time of  $t = 2.0$  after which the shock has reflected from the origin as shown in Figure 21. Our analysis is done at a time of maximum compression  $t = 1.0$ . The scatter plots for density and SIE are compared to the analytic solution at  $t = 1.0$  in Fig. 22 for the 80x160 calculation. The CGR result tracks the analytic well, while the CCH2 has much larger errors, especially with respect to SIE. As in the Coggeshall problem, the thermodynamic results are sensitive to velocity errors. For CCH2, the SIE is low because the theoretical compression is not achieved.

The L1 convergence plots for density and pressure at  $t = 1.0$  are plotted in Figure 23 and listed in Table 4 at  $t=1.0 \mu s$ . For both density and pressure, the CGR method converges at a rate of almost 2, while that of CCH2 is only slightly greater than 1.

### 5.6. Verney and Howell problems

Verney [107] examined the case of finite-radius, spherical copper and uranium shells collapsing under a given loading and constructed a simplified, approximate mathematical model of the problem, assuming incompressible, elastic-perfectly-plastic material response. The initial kinetic energy of the material dissipates via conversion to plastic work. These simplifications lead to a closed-form solution for the final inner radius. Later, Howell [53] considered the case of cylindrical shells.

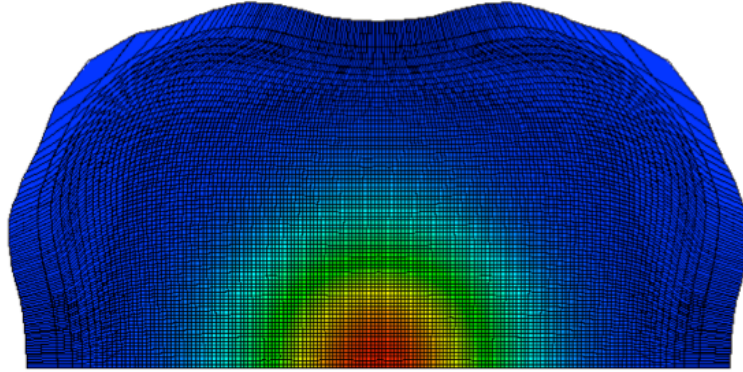


Figure 21: Kidder ball. CGR calculation on a 80x160 mesh at  $t=2.0$  showing the reflection from the origin. Colors reflect density.

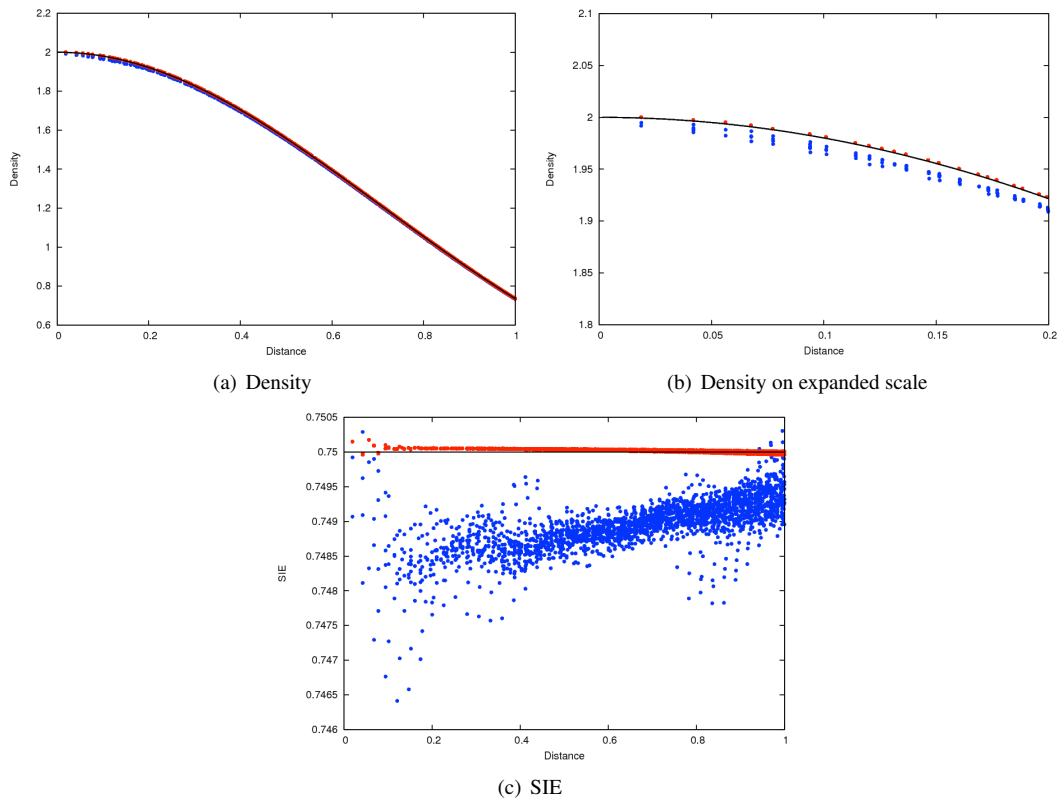


Figure 22: Kidder ball. Scatter plots vs. distance at  $t = 1.0$  for 80x160 mesh resolution. Shown are (a) density, (b) density on an expanded scale, and (c) SIE. CCH2 (blue), CGR (red), and analytic (black).

	Cell size	L1 density	L1 pressure
CCH2	0.6	6.6776e-2	5.9530e-2
	0.3	2.7552e-2	2.3644e-2
	0.15	1.1142e-2	8.7013e-3
	0.075	5.5141e-3	4.0198e-3
	0.0375	2.6478e-3	1.8462e-3
	0.01875	1.2751e-3	8.6276e-4
	0.009375	6.2991e-4	4.2156e-4
CGR	0.6	3.6037e-2	1.6648e-2
	0.3	1.1796 e-2	6.7043e-3
	0.15	2.7809e-3	1.5172e-3
	0.075	7.7574e-4	4.4222e-4
	0.0375	2.0516e-4	1.1676e-4
	0.01875	5.1321e-5	2.9236e-5
	0.009375	1.2969e-5	7.4131e-6

Table 4: Kidder ball. L1 volume-weighted density and pressure norms at  $t = 1$ . for CCH2 and CGR.

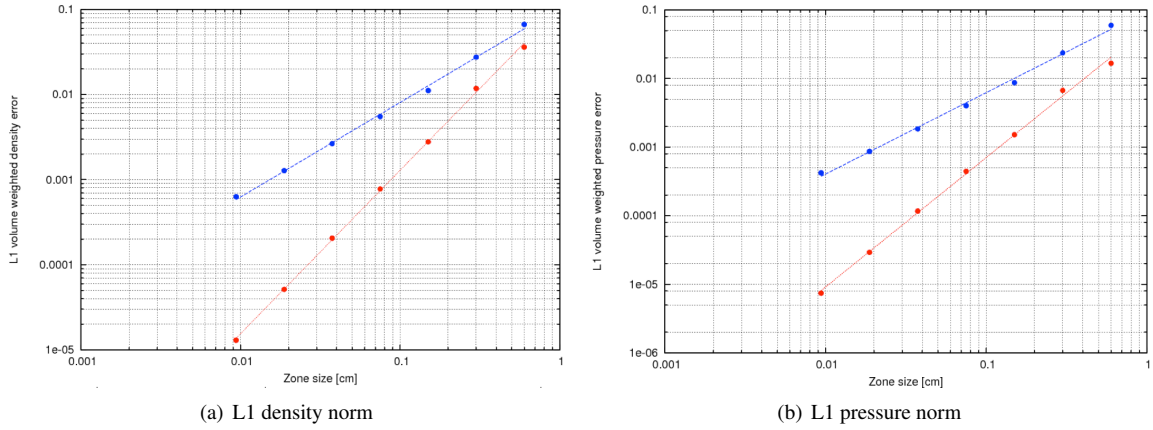


Figure 23: Kidder ball. Convergence plots at  $t = 1$ . Density convergence rates were 1.111 (CCH2 blue) and 1.920 (CGR red). Pressure convergence rates were 1.186 (CCH2 blue) and 1.885 (CGR red).

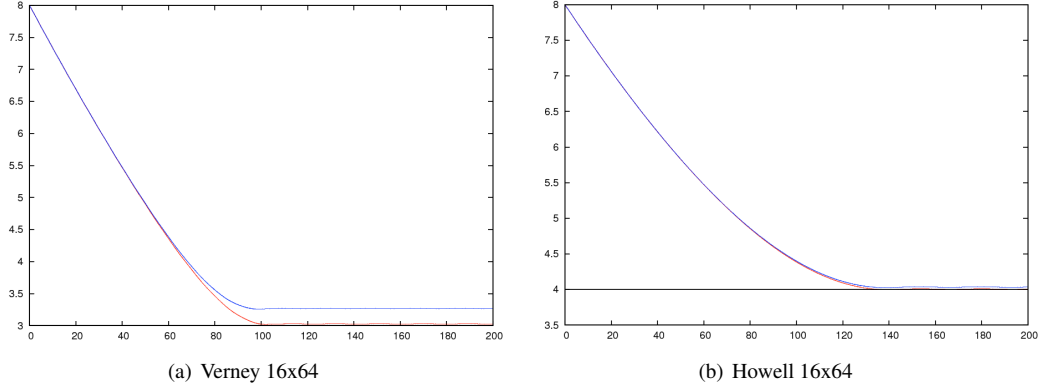


Figure 24: Verney and Howell for 16x64 resolution. Inner radius vs. time for CCH2 (blue) and CGR (red) for the RZ Verney problem (a) and the XY Howell problem (b). On this scale, CCH2 and CGR agree well for Howell but not for Verney.

Mesh	Cell size	Verney CCH2	Verney CGR	Howell CCH2	Howell CGR
4x16	0.050000	4.2812	3.5197	4.5033	4.1430
8x32	0.025000	3.6122	3.1419	4.1294	4.0211
16x64	0.012500	3.2639	3.0249	4.0262	3.9975
32x128	0.006250	3.0867	2.9897	3.9987	3.9915
64x256	0.003125	3.0108	2.9796	3.9912	3.9894
128x512	0.001562	-	2.9734	-	3.9885

Table 5: Verney and Howell problems. Minimum inner radii for CCH2 and CGR. The 128x512 CGR calculations were used as a reference for both CCH2 and CGR.

The cylindrical and spherical problems considered here model the collapse of a 2 cm thick Be shell. The Be is modeled as a compressible material with a density  $\rho_0 = 1.85 \text{ g/cm}^3$ , shear modulus  $G = 1.51 \text{ Mb}$ , yield strength  $Y_0 = 0.0033 \text{ Mb}$ , and a Gruneisen equation of state with  $c_0 = 0.7998$ ,  $s = 1.124$ ,  $\Gamma = 1.16$ . The initial velocity distribution that drives the shell is divergence free and is given by

$$u(r) = u_0 \left( \frac{R_{\text{outer}}}{r} \right)^\alpha \quad (27)$$

The initial stress state is traceless, on the yield surface, and properly rotated. The initial inner and outer radii were 8 and 10 cm respectively and the azimuthal angle was from  $0^\circ$  to  $180^\circ$ . We considered radial and azimuthal mesh resolutions of 4x16, 8x32, 16x64, 32x128, 64x256, and 128x512.

In the XY Howell problem  $\alpha = 1.0$  and  $u_0 = 0.04902 \text{ cm}/\mu\text{s}$ . The shell coasts in until the kinetic energy is dissipated as plastic work. The analytic solution has a stopping time of about  $140 \mu\text{s}$  and an inner radius of 4.0 cm. In the RZ Verney problem  $\alpha = 2.0$  and  $u_0 = 0.06750 \text{ cm}/\mu\text{s}$ . The analytic solution has a stopping time of about  $100 \mu\text{s}$  and an inner radius of 3.0 cm. Figure 24 shows the calculated inner radius vs. time for 16x64 meshed Verney (a) and Howell problems (b). CCH2 results appear in blue, and CGR results in red. On this scale, CCH2 and CGR agree well for Howell but not for Verney.

The numerical solution is compressible, so that the incompressible analytic result does not hold exactly. Acoustic waves at a stress level less than the yield surface continue to propagate with minimal dissipation as shown in the expanded Figure 25. The figure plots the inner radius vs. time for 5 resolutions for both CCH2 (left) and CGR (right) for both the Verney (top) and Howell (bottom) problems. Note that the coarser resolutions are off scale in the CCH2 plots (left).

Because the kinetic energy is not completely dissipated in the compressible calculation, a converged solution to the simulation should oscillate about an average inner radius less than that obtained analytically. In the absence of a

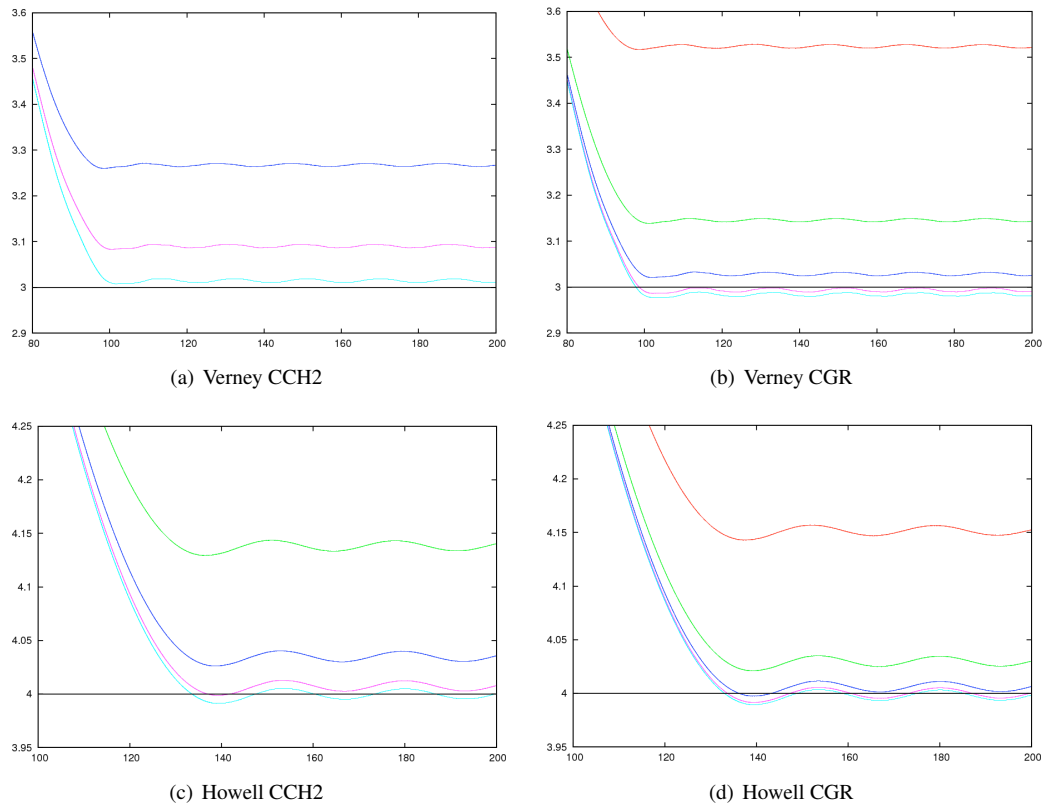


Figure 25: Verney and Howell problems. Inner radius vs. time showing late time acoustic response. Resolutions shown: 4x16 (red), 8x32 (green), 16x64 (blue), 32x128 (purple), 64x256 (aqua). Note that the coarser resolutions are off scale in the CCH2 plots (left).

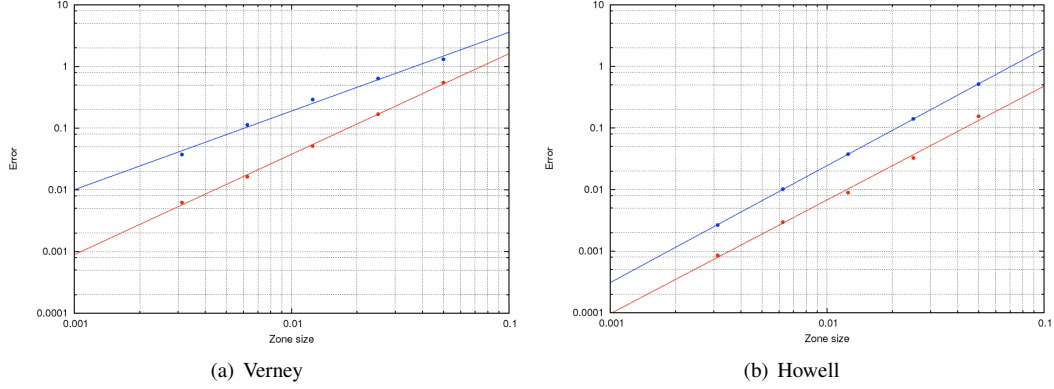


Figure 26: Verney and Howell problems. Error in the minimum radius vs. radial mesh size. For both problems, the CGR error (red) is significantly less than that of CCH2 (blue). For Verney (a), the respective convergence rates are 1.278 (CCH2) and 1.628 (CGR). For Howell (b), the respective convergence rates are 1.898 (CCH2) and 1.846 (CGR).

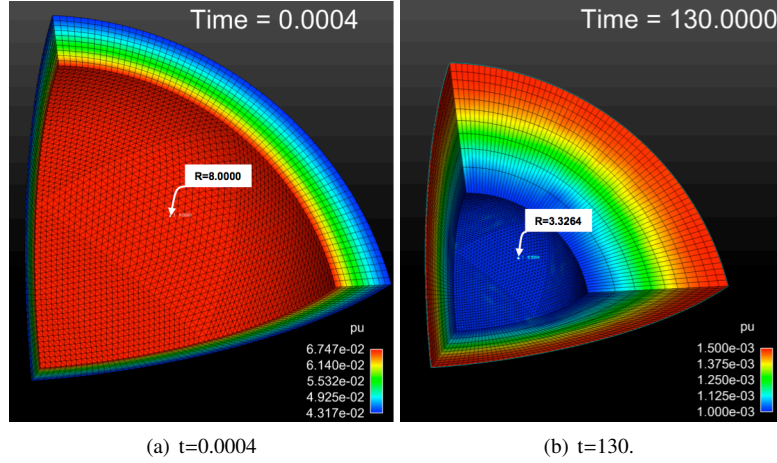


Figure 27: 3D Verney. Geodesic mesh at  $t=0.004$  and 130. The result is comparable to the coarsely gridded 2D result.

dynamic analytical result, we used a higher resolution CGR (128x512) calculation as a reference. As a figure of merit, we took the minimum inner radius near a time of 100 for Verney and 140 for Howell. The radii are shown in Table 5, and the reported error is the difference between the tabulated radii and the reference radius. The convergence rates are plotted in Figure 26. The CCH2 and CGR rates were comparable for the Howell problem, but CGR was much better for the Verney problem.

We have included a 3D Verney calculation to demonstrate CGR in a 3D configuration with strength and an unstructured geodesic mesh. Figure 27(a) shows the initial mesh for a very coarsely gridded 3D Verney problem. The mesh is geodesic [43, 44] with 10 cells in the radial direction. Figure 27(b) shows the mesh at  $t=130 \mu s$ . Colors represent velocity magnitude. The result is comparable to the coarsely gridded 2D result.

### 5.7. Taylor anvil

Taylor anvil experiments have their origins in the work of G.I. Taylor [97] and are often used to calibrate material strength parameters. Although this problem begins with a shock, we have included it among the *smoothflow* test problems because the solution is dominated by later flow. Our assumed configuration consists of a cylindrical copper rod of radius 0.32 cm and length 3.24 cm, impacting a rigid surface at velocity 227 m/s [92]. There are no analytical results for this particular test problem, and no direct comparison with experiment. As a test problem, the Taylor anvil is principally useful in comparing dissipation and stiffness in numerical algorithms. The final positions of the toe



$R$  (the  $r$  axis position of the bottom of the rod) and heel  $Z$  (the  $z$  axis position of the top of the rod) are taken as a measures of the calculated plastic dissipation, the larger radius and shorter length corresponding to less dissipation.

The assumed copper material properties are: initial density  $\rho_0=8930 \text{ kg/m}^3$ , shear modulus  $G=43.333 \text{ GPa}$ , yield stress  $Y_0=400 \text{ MPa}$ , hardening modulus  $Y_H=100 \text{ MPa}$ , and a Gruneisen equation of state with  $c_0=3940.$ ,  $s=1.48$ ,  $\Gamma=2.0$ .

In the simulation, the rod is constrained to stick to the surface, although this is not true experimentally. We note that calculations in which the rod is not constrained to the surface were presented in Reference [81]. Our calculations were carried out up to a time of  $80 \mu\text{s}$ , at which point nearly all the initial kinetic energy had been dissipated into internal energy. The results are sensitive to the resolution. For comparison purposes we use a relatively coarse mesh of  $24 \times 80$  cells respectively in the radial and axial directions.

Figure 28 (a and b) compares the CCH2 (left) and CGR (right) configurations at  $80 \mu\text{s}$ , clearly showing greater dissipation in the CCH2 calculation as evidenced by the deformation. The respective toe positions were  $R=0.006625$  and  $0.006972$ . The respective heel positions were  $Z=0.02197$  and  $0.02150$ . Figure 28 (c left) demonstrates the checkerboard patterns that can occur if only the LSQ point gradient is used, corresponding to  $\lambda = 0$ . in Section 15. The pattern is essentially removed by mixing LSQ point and corner gradients as indicated in Figure 28 (c right) for  $\lambda = 0.25$ . The heel and toe positions were relatively unaffected by this parameter.

## 6. Shock dominated problems

### 6.1. Sod shock tube

The Sod shock tube is a very well known problem defined in [96]. It consists of a shock tube of 100 units in length. The interface is located at  $x = 50$ . At the initial time, the states on the left and the right sides of the interface are uniform. The left state is a high pressure fluid characterized by  $\{\rho_L, p_L, u_L\} = \{1, 1, 0\}$  the right state is a low pressure fluid defined by  $\{\rho_R, p_R, u_R\} = \{0.125, 0.1, 0\}$  The polytropic gas is defined by  $\gamma = 7/5$ . Physically, the problem is 1D, but we model it on a 2D mesh. The computational domain is defined by  $[x, y] \in [0, 100] \times [0, 10]$ . The initial mesh is a Cartesian grid with  $1000 \times 10$  cells. The boundary conditions are reflective.

In Figure 29, we compare scatter plots of density, pressure, velocity and specific internal energy for CCH2 and CGR at  $t=20$ . There are only minor differences between the calculations, the greatest being in the SIE field that is expanded in Figure 30. The CGR calculation has slightly greater wall heating at the contact discontinuity but is also sharper at the shock. There was no observable variation through the 10 cells in the  $y$  direction.

### 6.2. Noh problem

The Noh problem [85] has been used extensively to illustrate the difficulties of preserving symmetry as well as exposing tendencies to produce a well known entropy error known as wall heating [23]. The material is a polytropic gas with  $\gamma = 5/3$ . Initially the velocity is directed radially inward with a unity magnitude, the density is unity, and the internal energy is small ( $10^{-4}$ ). The converging flow causes a shock to form at the origin and propagate radially outward. The density plateau behind the shock wave reaches a uniform value of 16 in XY and 64 in RZ out to a radius of 0.2 at  $t=0.6$ . Numerically, the proper density near the origin is not obtained because of the aforementioned wall heating. Two types of mesh are commonly employed: a polar grid with equiangular zoning and a square or box grid.

**2D polar meshes.** The polar grids used were 100 cells in the radial direction by 40 in the azimuthal. As shown in Figure 31(a) for XY geometry and in (b) for RZ geometry, CCH2 and CGR produce nearly identical results. In both cases, CGR had less wall heating in the first cell. For both CCH2 and CGR, the RZ formulation described in [15] guarantees symmetry on equiangular polar meshes. With 40 azimuthal cells, convergence of the flow produces large aspect ratio cells near the origin as the radial velocity tends toward zero. Because  $\hat{\mathbf{a}}$  in Equation 11 vanishes for stationary flow, these cells can become unstable. To avoid this, the parameter  $\eta$  in Equation 13 was set to a large number, forcing  $\hat{\mathbf{a}}$  to equal the corner normal. Figure 32 shows the effect of the  $s$  term in Equation 10 for a CGR calculation. Omitting this term clearly reduces the wall heating.

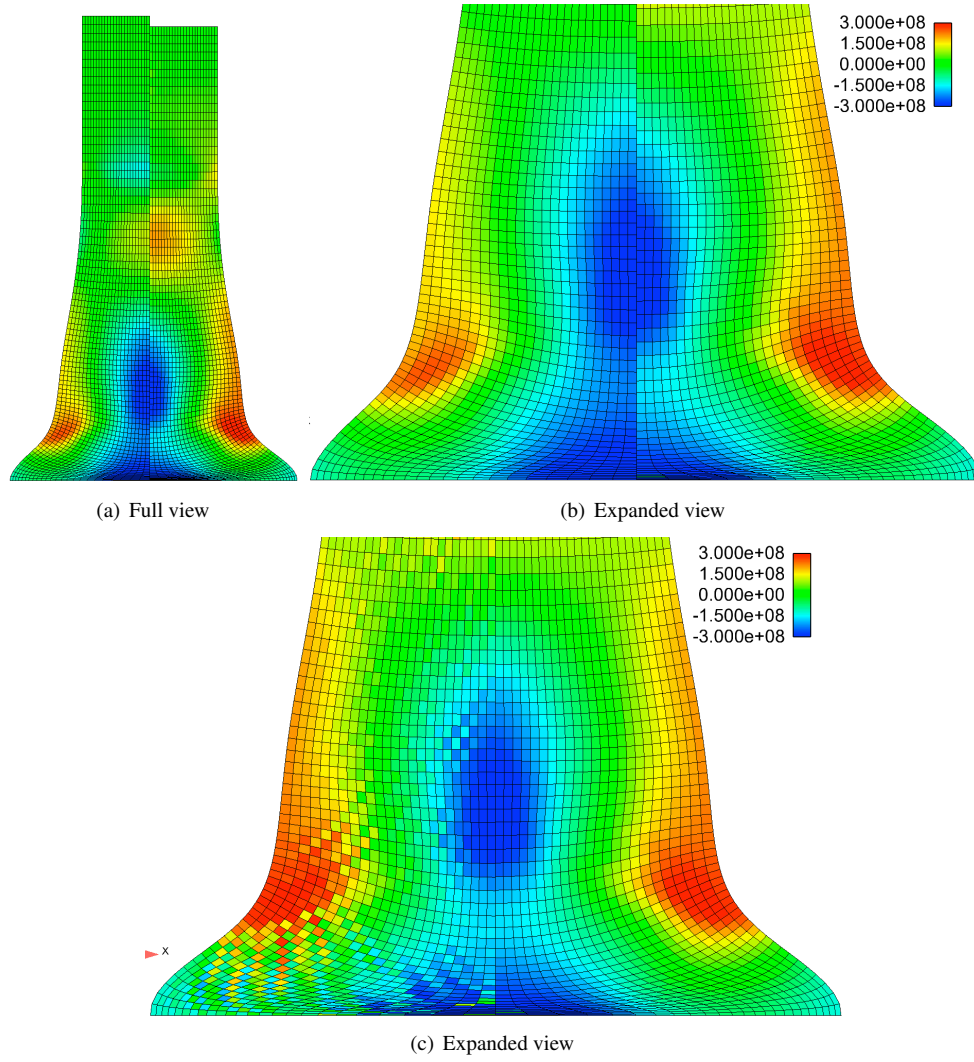


Figure 28: Taylor anvil at  $t=80 \mu s$  (a) full view, (b) expanded view. Pressure contours comparing CCH2 (left) and CGR (right) on a scale of  $-3 \cdot 10^8$  to  $+3 \cdot 10^8$ . The respective toe positions were  $R=0.006625$  and  $0.006972$ . The respective heel positions were  $Z=0.02197$  and  $0.02150$ . (c) CGR checkerboard pattern (left) with  $\lambda = 0.0$  and (right) reduction with  $\lambda = 0.25$  although a small amount remains near the axis.

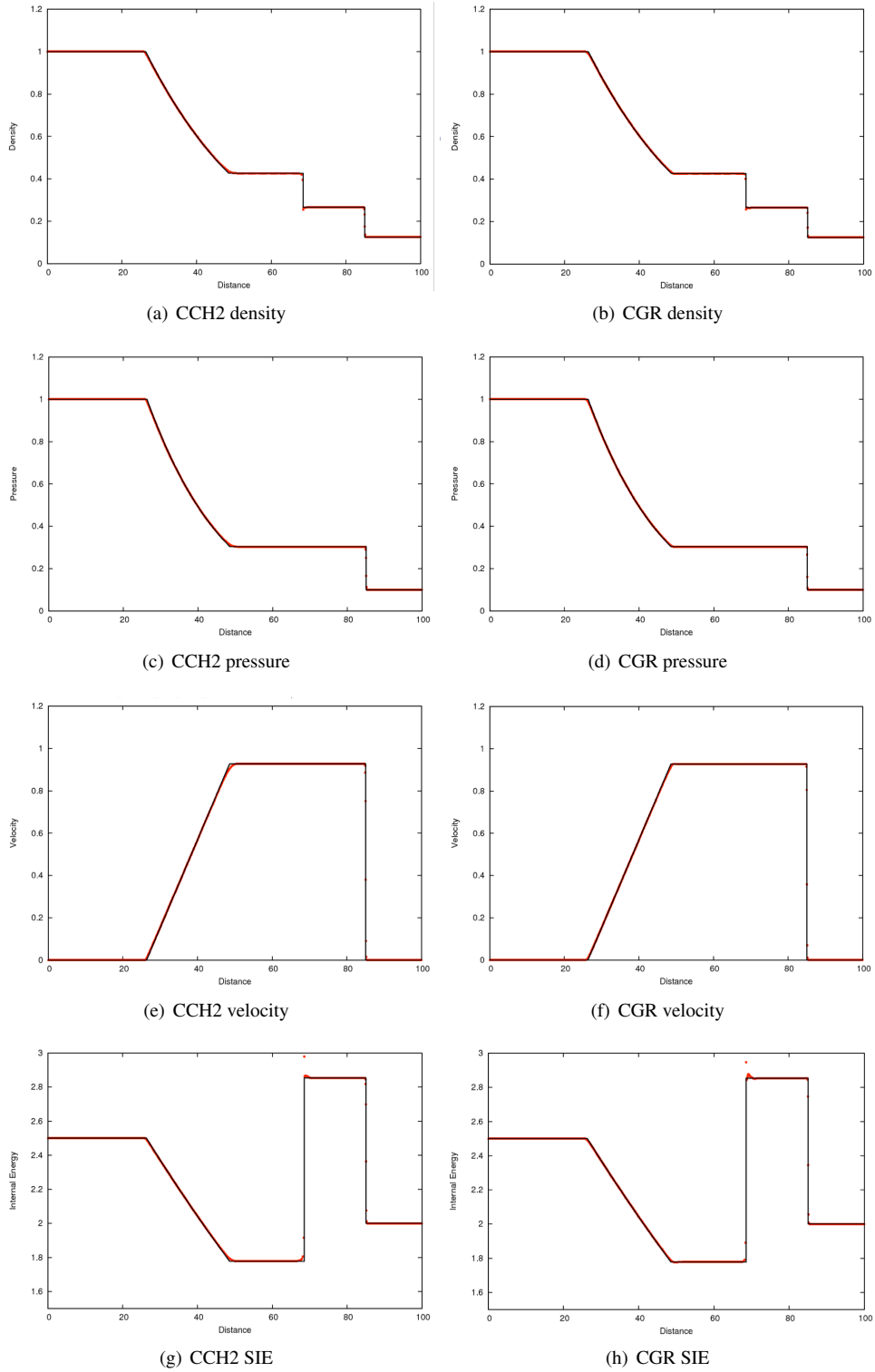


Figure 29: Sod. Scatter plots of density, pressure, velocity and specific internal energy vs. position at  $t=20$  for CCH2 (left) and CGR (right). Analytic result in black.

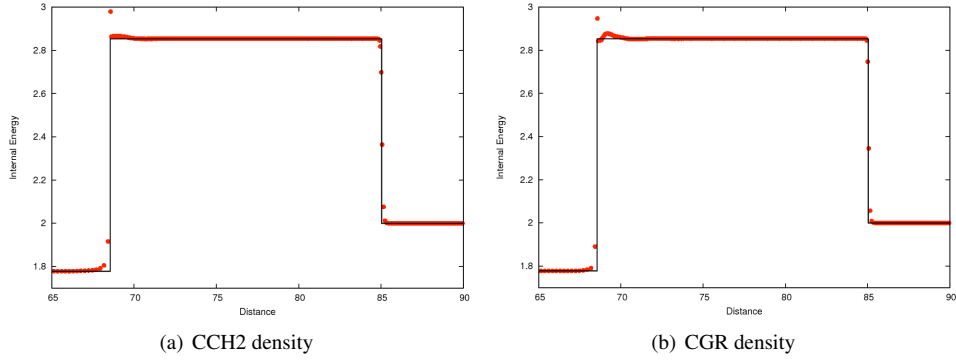


Figure 30: Sod. Comparison of SIE at  $t=20$  for CCH2 (a) and CGR (b). Analytic result in black.

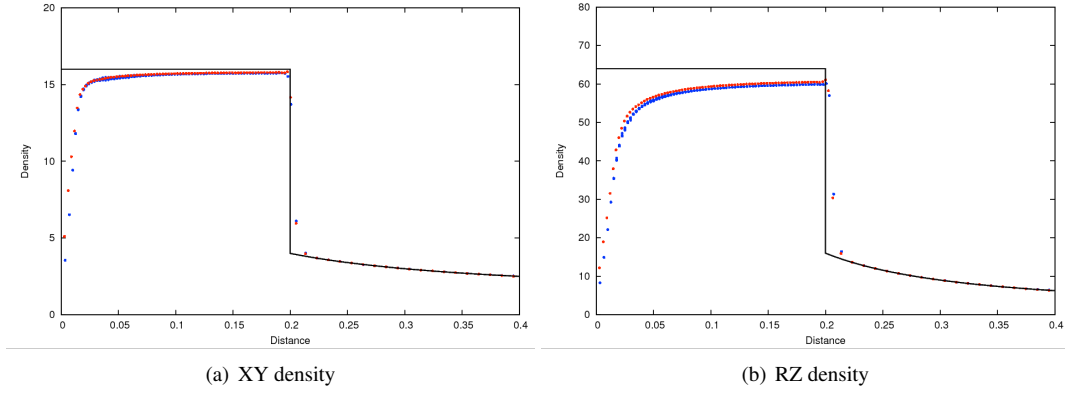


Figure 31: Noh 40x100 polar mesh. Scatter plot of density vs. radius comparing CCH2 (blue) and CGR (red) in XY (a) and RZ (b) geometries. Analytic result in black.

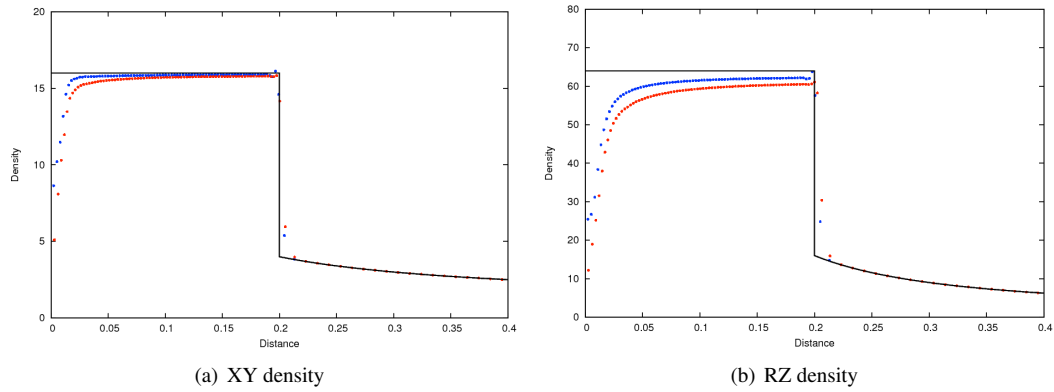


Figure 32: Noh 40x100 polar mesh. Scatter plot of density vs. radius showing the effect of the  $s$  term in Equation 10 for CGR in XY (a) and RZ (b) geometry. Off (blue), on (red). Results are comparable for CCH2. Analytic result in black.

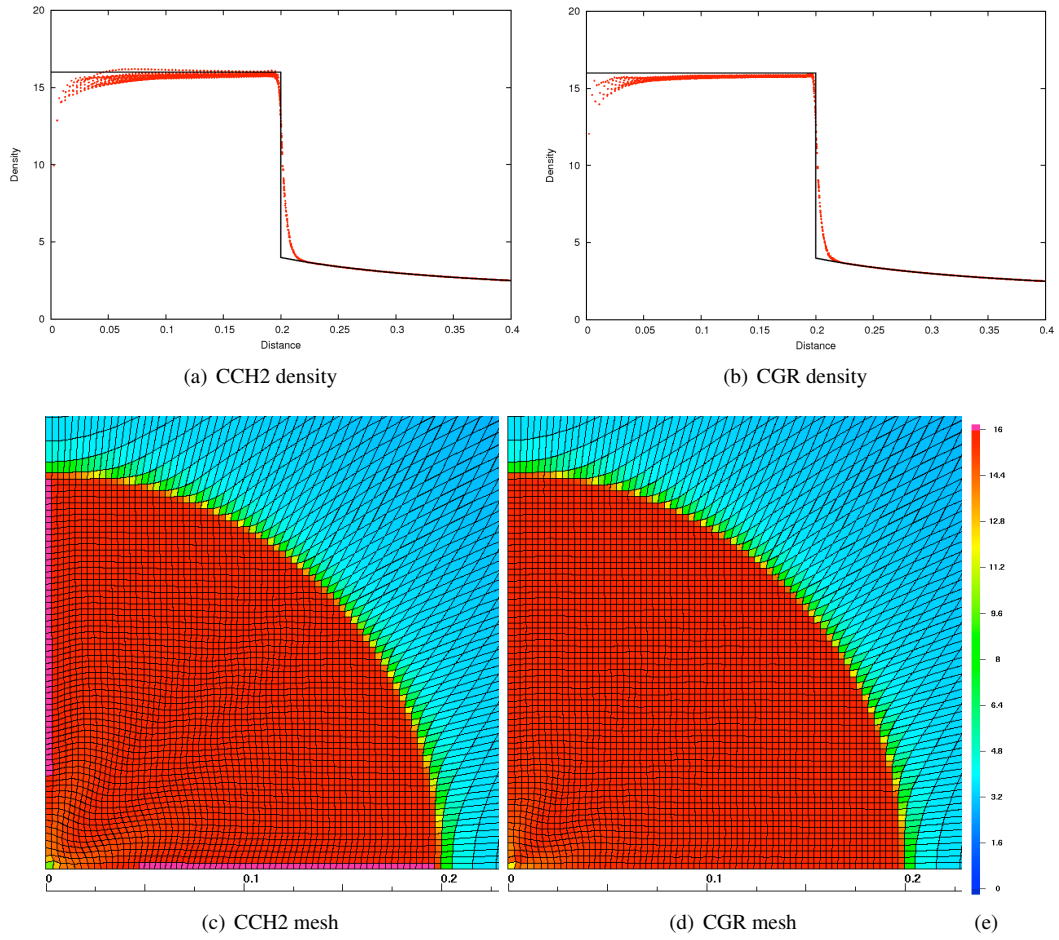


Figure 33: Noh XY 100x100 box mesh. Scatter plot of density vs. radius on a box grid: CCH2 (a) and CGR (b). Analytic result in black. Corresponding mesh plots colored by density appear in (c) and (d).

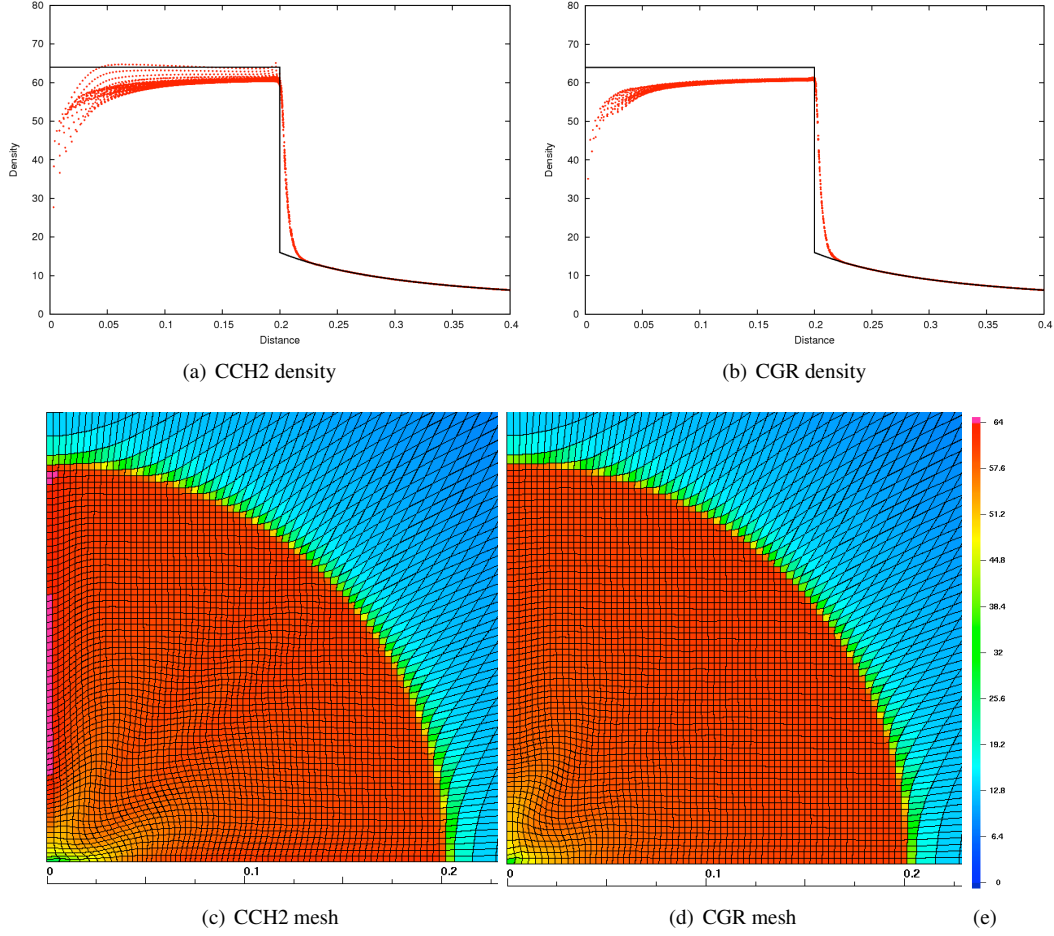


Figure 34: Noh RZ 100x100 box mesh. Scatter plot of density vs. radius on a box grid: CCH2 (a) and CGR (b). Analytic result in black. Corresponding mesh plots colored by density appear in (c) and (d).

*2D box meshes.* For our box grid comparisons, we use a 100x100 square grid on a physical domain on  $[0,1.2]$  in both directions. As in the polar calculations, the parameter  $\eta$  in Equation 13 was set to a large number, forcing  $\hat{\mathbf{a}}$  to equal the corner normal. As shown in Figure 33 (a and b), the density fields calculated by CCH2 and CGR in XY geometry are comparable. The corresponding mesh plots colored by density appear in Figure 33 (c and d).

Figure 34 (a and b) compares the density fields calculated by CCH2 and CGR in RZ geometry. The CGR result has excellent symmetry and reduced wall heating errors. CCH2 has more scatter as well as more wall heating. The corresponding mesh plots colored by density appear in Figure 34 (c and d). The CCH2 mesh displays significant loss of symmetry and mesh distortion near the origin, whereas that of CGR remains good. We note that the symmetry proof for the RZ formulation described in [15] applies only to equiangular polar meshes, not for box meshes used here. The choice of the  $\lambda$  parameter used in all the CGR test problems was largely based upon the results shown in Figure 35 in which  $\lambda=0.25$  significantly reduces the spread in the density distribution.

*3D box mesh.* Figure 36 compares the density fields calculated by CCH2 and CGR in 3D XYZ geometry. CCH2 has considerably more scatter than CGR. The differences between CCH2 and CGR are also apparent in Figure 37 that compares mesh plots for CCH2 (a) and CGR (b). The colors represent density. Figure 37 (c) is a CGR result in which the gradient operators do not use the auxiliary ghost cells discussed in Section 4.1. The lack of symmetry along the block edges is apparent.

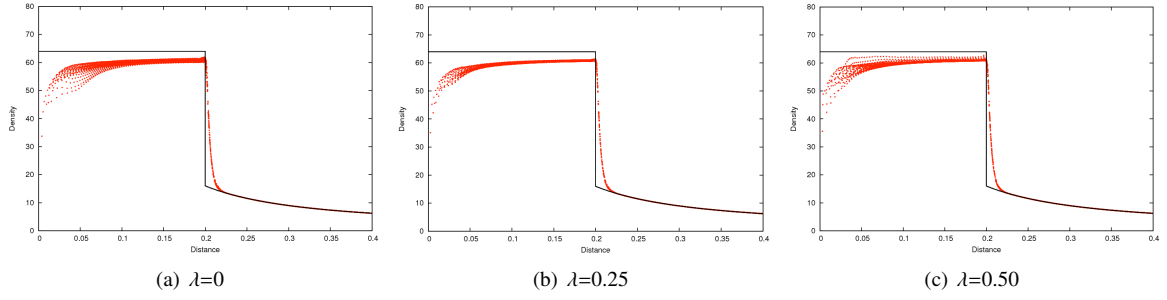


Figure 35: Noh RZ 100x100 box mesh. Scatter plot of density vs. radius on a box grid, varying the CGR  $\lambda$  parameter. The choice  $\lambda=0.25$  significantly reduces the spread. Analytic result in black.

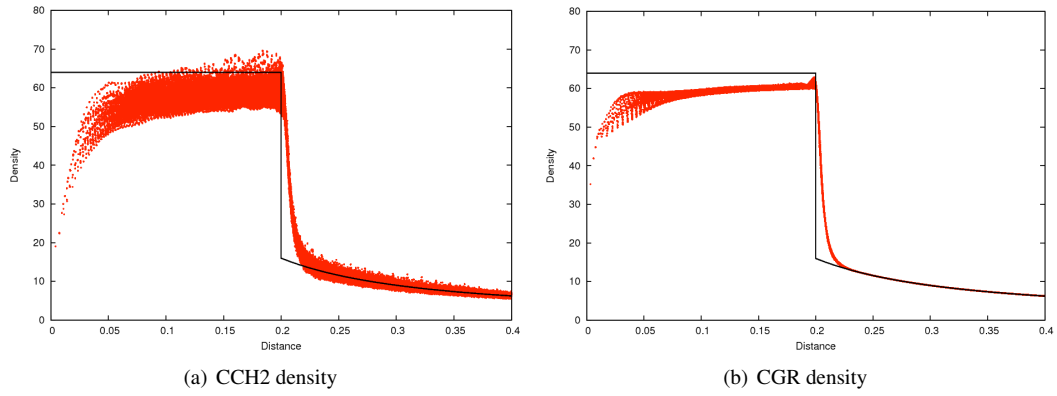


Figure 36: 3D Noh 96x96x96 box mesh. Scatter plot of density vs. radius on a box grid: CCH2 (a) and CGR (b). The latter compares favorably with the CGR RZ calculation in Figure 34(b). Analytic result in black.

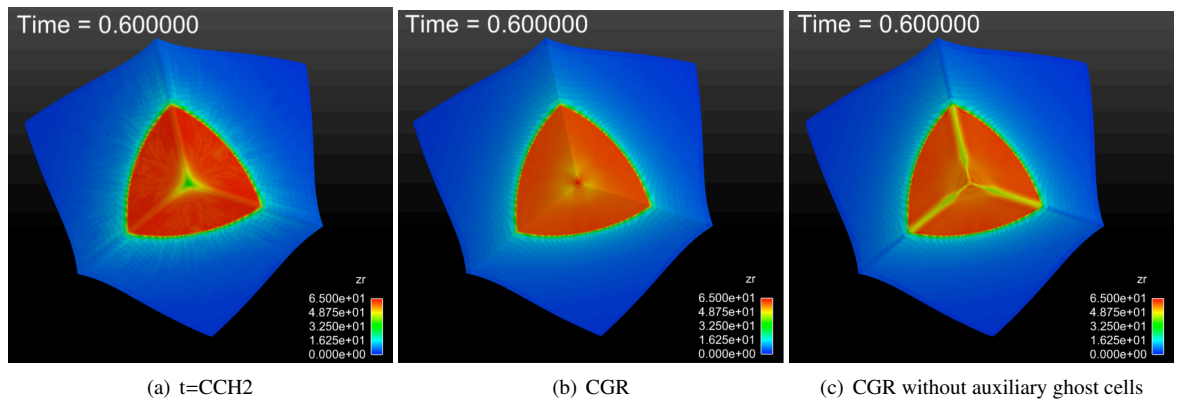


Figure 37: 3D Noh 50x50x50 box mesh. Surface plots of density. Mesh cube viewed from the origin.

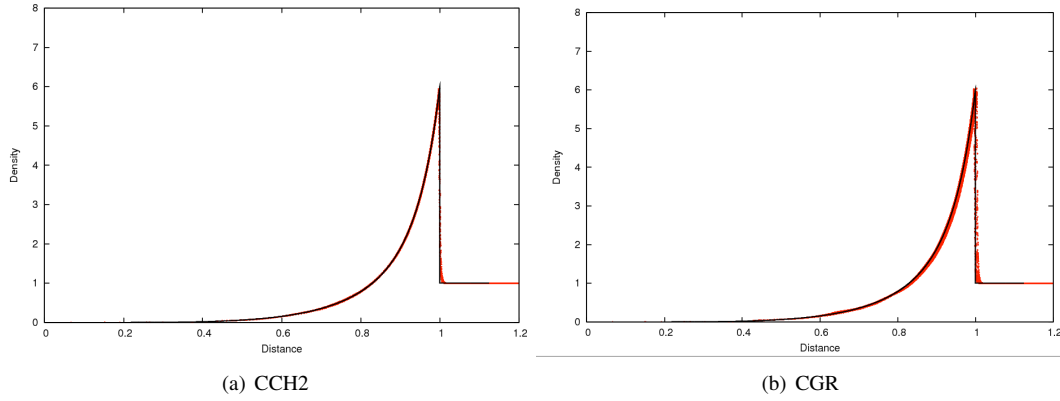


Figure 38: Sedov XY. Scatter plots of density vs. distance for CCH2 (a) and CGR (b) on a 200x200 box grid. The analytic peak density is 6.0.

### 6.3. Sedov blast wave

In this section, we present results of the Sedov blast wave [93] as an example of a diverging shock wave with a similarity solution. The initial setup consists of a square grid extending from 0 to 1.2 in both  $x$  and  $y$  directions defining a single quadrant. Except as noted, calculations were run on a 200x200 square mesh. All boundaries are reflective. The material is a polytropic gas with initial density of unity and initial velocity, zero everywhere. The specific internal energy is effectively zero ( $10^{-6}$ ) except in the source region. We consider two variations of the problem.

*XY.* In XY, we used  $\gamma = 7/5$ . The energy source was a single cell with internal energy 0.245919. The similarity solution for a point source predicts that the shock should be at a radius of unity at a time of unity with a peak density of 6.0. Figure 38 compares the two. Both match the analytic solution well, but CCH2 has less scatter. The CGR method appears to be more sensitive to the grid distortion along the diagonal shown in Figure 39.

*RZ.* In RZ, we used  $\gamma = 5/3$ . The energy source was a single cell with internal energy 0.26795. The similarity solution for a point source predicts that the shock should be at a radius of unity at a time of unity with a peak density of 4.0. Figure 40 compares CCH2 and CGR. The solutions are comparable and match the analytic solution well.

*3D.* In 3D, we again used  $\gamma = 5/3$ . We modeled an octant with a 48x48x48 mesh on a cubical domain of length 1.2 in each direction. The energy source was a single cell with internal energy 0.0616988. Figure 41 compares CCH2 and CGR. Again, the solutions are comparable and match the analytic solution well.

### 6.4. Saltzman shock tube

The Saltzman problem was proposed by J. Saltzman and is documented in various sources [78, 36, 12]. It consists of a piston-driven planar shock passing through a skewed mesh not aligned with the flow and was devised to test robustness of Lagrangian methods. In 1D, the unskewed problem is simply a shock tube of unit length, driven on the left by a fixed velocity of unity. The material is a polytropic gas with  $\gamma = 5/3$  and  $\{\rho_0, e_0, u_0\} = \{1., 1.e - 6, 0.\}$ . The shock develops at the piston face and propagates at a velocity of  $4/3$  until it reflects from the right boundary at  $t = 0.75$  and reflects again from the piston face at  $t = 0.90$ . The density should be equal to 4.0 in the singly shocked region and equal to 10.0 in the doubly shocked region that results after the first reflection.

*2D Saltzman.* Numerical results for the 2D Saltzman problem have been reported by many authors for both staggered [78, 36, 12] and cell-centered schemes [74, 13]. The 2D problem domain is  $(x, y) \in [0, 1] \times [0, 0.1]$  and is defined by

$$\begin{aligned} x_{ij} &= L(i-1) + L(11-j) \sin[\pi(i-1)] \\ y_{ij} &= L(j-1) \end{aligned}$$

in which  $L = 0.01$  and the indices are in the range  $(i, j) \in [1, 101] \times [1, 11]$ . The resulting mesh is shown in Figure 42(a). Boundaries are reflective except for the  $x = 0$  boundary that is driven with a constant rightward velocity of



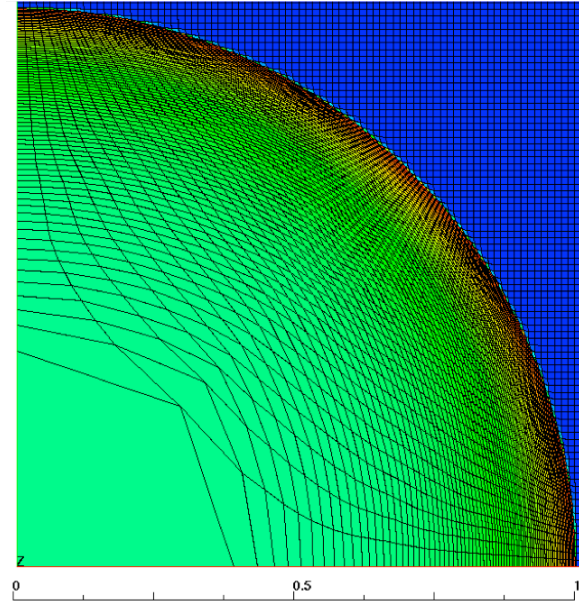


Figure 39: Sedov XY. 100x100 mesh showing systematic deformation in the 45 degree direction. Colors represent pressure.

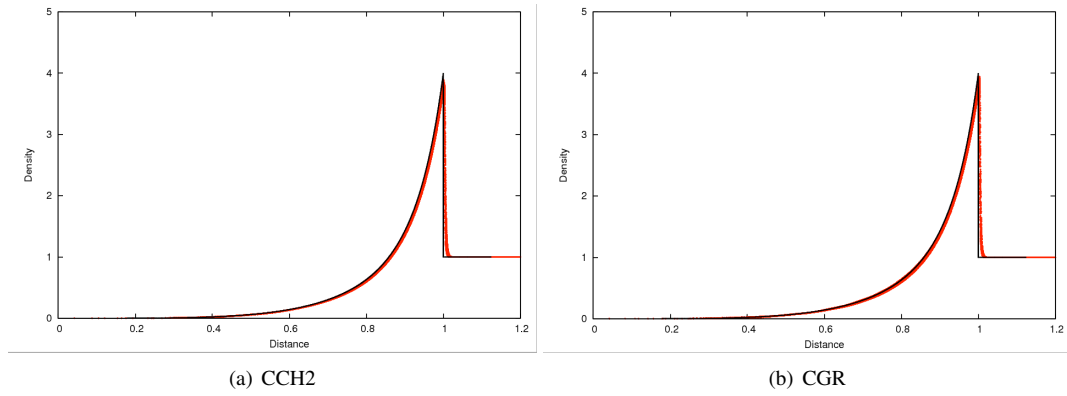


Figure 40: Sedov RZ. Scatter plots of density vs. distance for CCH2 (a) and CGR (b) on a 200x200 box grid. The analytic peak density is 4.0.

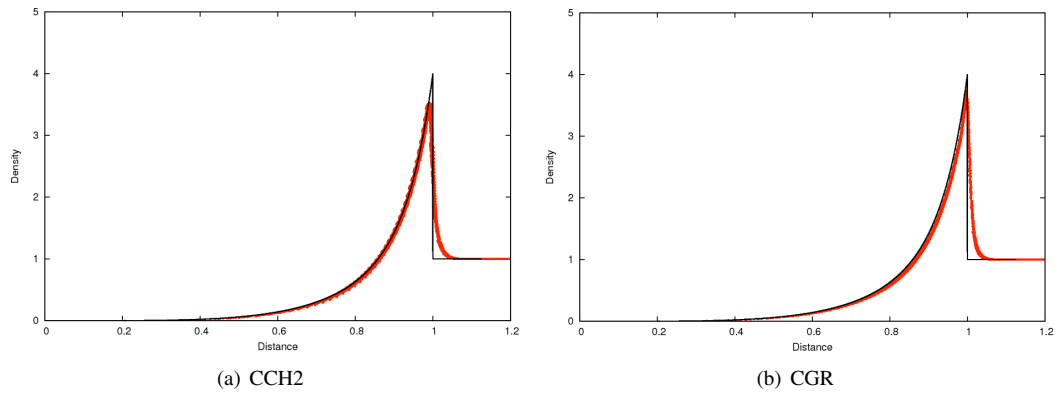
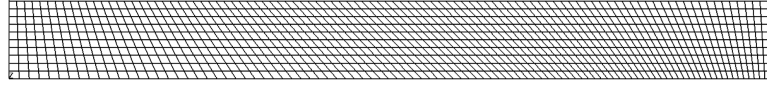
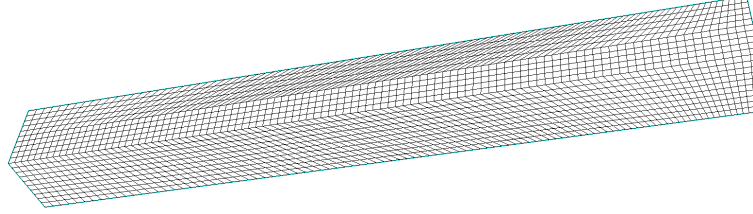


Figure 41: Sedov 3D. Scatter plots of density vs. distance for CCH2 (a) and CGR (b) on a 48x48x48 box grid. The analytic peak density is 4.0.



(a) 2D Saltzman mesh



(b) 3D Saltzman mesh

Figure 42: Saltzman. (a) 2D and (b) 3D meshes

unity. Because the physical flow is one-dimensional, the calculated mesh lines should be horizontal, and the density field should be uniform in the vertical direction.

Figure 43 shows CCH2 and CGR XY meshes at times of 0.70, 0.85 and 0.90. The results are comparable at  $t=0.7$ , but the CGR shock front is clearly more vertical at  $t=0.85$ , and the CGR mesh lines are more horizontal at  $t=0.90$ . The RZ comparison is similar and only the  $t=0.90$  meshes are shown in Figure 44. The corresponding XY densities are shown in Figure 45. Aside from a spike at the front at 0.70, the CGR results are clearly superior.

*3D Saltzman.* A 3D extension of the problem was proposed by E. Caramana, *et. al.* [22] who employed a staggered scheme. The problem has since been calculated by others in a cell-centered context [77, 6]. Reported calculations have tended to terminate by about a time of 0.8 or earlier because of tangling or small time step.

The 3D problem domain is  $(x, y, z) \in [0, 1] \times [0, 0.1] \times [0, 0.1]$  defined by

$$\begin{aligned} x_{ijk} &= \begin{cases} L(i-1) + 0.2L(11-k)(6-j)\sin[\pi(i-1)] & i \leq j \leq 6 \\ L(i-1) + 0.2L(k-1)(j-2)\sin[\pi(i-1)] & 7 \leq j \leq 11 \end{cases} \\ y_{ijk} &= L(j-1) \\ z_{ijk} &= L(k-1) \end{aligned}$$

in which the indices are in the range  $(i, j, k) \in [1, 101] \times [1, 11] \times [1, 11]$ . Note that the  $j = 6$  plane is unmodified while the  $j = 1$  and  $j = 11$  planes have opposite skew. The resulting mesh is shown in Figure 42(b).

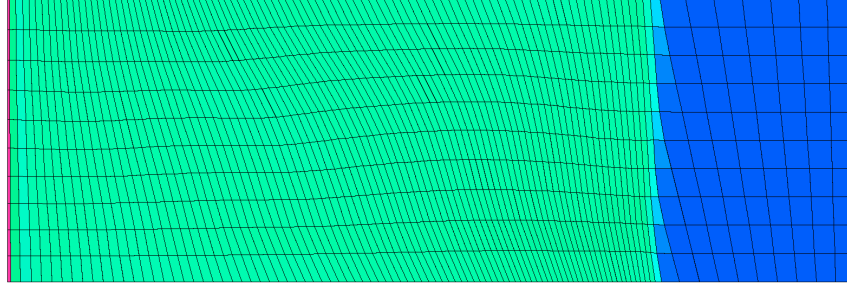
Both CCH2 and CGR 3D calculations were performed. The CCH2 calculation terminated at  $t=0.79$ , whereas the CGR calculation ran to nearly  $t=0.95$ . The CGR results are presented in Figure 46 at times corresponding to those of the 2D Figures 43 and 45. In the scatter plots, blue dots correspond to cells near the central plane and are in reasonable agreement with the 2D results of Figure 45. All other cells are indicated by red dots. Because the CCH2 calculation terminated before  $t=0.8$ , we compare CCH2 and CGR at earlier times of 0.60, 0.70, and 0.75 as shown in Figure 47. The CGR results have markedly less scatter.

### 6.5. Adiabatic release

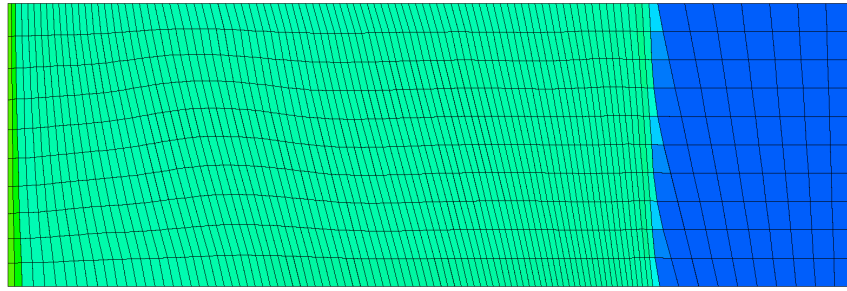
This test problem was originally posed by G. Bazan and formalized by R. Rieben [5] to verify the ability to follow adiabatic release down an isentrope following shock compression to Hugoniot density. An extensive code comparison was done in [86].

The problem can be viewed as a 1D Riemann problem on a domain  $x \in [0, 0.9]$  split into two materials with a contact discontinuity at  $x=0.3$  as shown in Figure 48. Each material is defined with the following equation of state

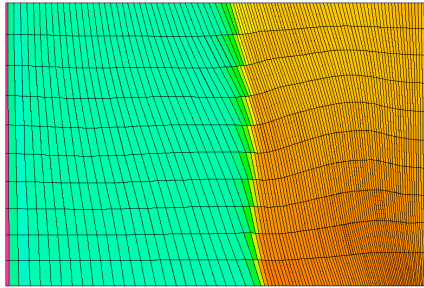
$$p(\rho) = \left( \frac{\rho}{\rho_0} - 1 \right) \rho_0 c_0^2 \quad (28)$$



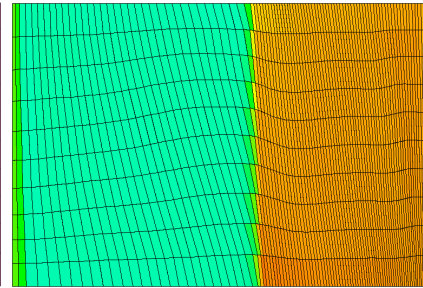
(a) CCH2 XY mesh at  $t=0.70$



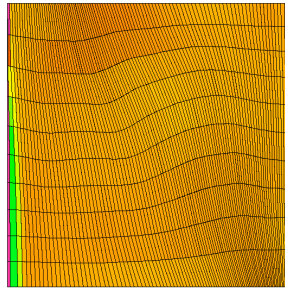
(b) CGR XY mesh at  $t=0.70$



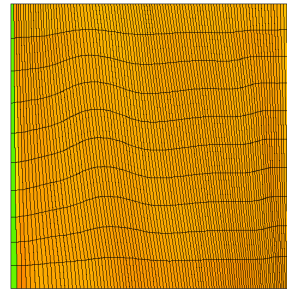
(c) CCH2 XY mesh at  $t=0.85$



(d) CGR XY mesh at  $t=0.85$



(e) CCH2 XY mesh at  $t=0.90$



(f) CGR XY mesh at  $t=0.90$



(g) Density scale

Figure 43: Saltzman 2D XY. Comparison of CCH2 and CGR meshes at  $t=0.70$  before reflection at the wall, 0.85 after the reflection, and 0.90 at the time of the reflection from the piston face. Color represents density on a scale of 0 to 12 as indicated in (g).

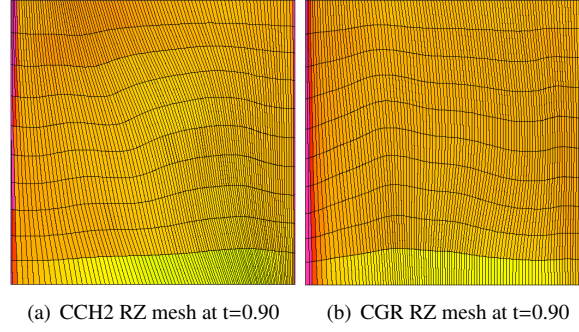


Figure 44: Saltzman 2D RZ. Comparison of CCH2 and CGR meshes at 0.90 at the time of the reflection from the piston face. Comparison at earlier times is similar to the XY case. Color represents density on a scale of 0 to 12 as indicated in Fig. 43(g)

in which  $\rho_0$  is the initial density,  $\rho$  is density and the sound speed at reference density  $c_0 = 0.4$ . The initial conditions are

$$\begin{aligned} \{u, \rho, e\}_L &= \{0.5, 16, 0\} \\ \{u, \rho, e\}_R &= \{0.0, 16, 0\} \end{aligned} \quad (29)$$

The boundary conditions at each end are free. The diagnostics consist of two Lagrangian tracer particles located initially at  $x = 0.36$  and  $x = 0.84$ . The problem is run until  $t = 1.4$  by which time a shock has formed at the contact, interacted with tracer 2 at about  $t \sim 0.83$ , formed a rarefaction at the free surface, and begun the release on tracer 2 at about  $t \sim 0.98$ . We ran 5 simulations with cell sizes of 0.01, 0.005, 0.0025, 0.00125, and 0.000625 cm.

An expression for the specific internal energy along the adiabat is easily derived. Following [5, 86]

$$u_p = \frac{1}{2} u_L \quad (30)$$

Based upon the initial conditions, the Hugoniot values are

$$\begin{aligned} p_H &= \rho_0 u_p (c_0 + u_p) \\ \rho_H &= \rho_0 \left(1 + \frac{u_p}{c_0}\right) \\ e_H &= \frac{p_H(\rho_H - \rho_0)}{2\rho_H\rho_0} \end{aligned} \quad (31)$$

The adiabat energy as a function of density is given by

$$e_A(\rho) = e_H + c_0^2 \left[ \frac{\rho - \rho_H}{\rho_0} - \ln\left(\frac{\rho}{\rho_H}\right) \right] \quad (32)$$

The figure of merit is the percentage error in this quantity. The SIE as a function of density during loading and release are shown in Figure 49.

Figures 50(a) and (b) shows the log of the SIE error along the adiabat as a function of density for CCH2 and CGR respectively. Both results compare very favorably with the best of those in Reference [86]. The CGR error is much less than CCH2 error over most of the release. Also, the CGR error remains relatively constant, whereas the error with CCH2 increases during the release.

### 6.6. Elastic-plastic piston

The elastic-plastic piston problem tests the strength formulation at the elastic-plastic limit. The objective is to match the speed and shape of the elastic precursor. The analytic solution for this problem was formulated from the discussion of impacts of elastic-plastic materials in Reference [100]. The mesh consists of 500x1 cells driven from the left with a velocity of 0.01 cm/ $\mu$ s. The material is aluminum with properties: density  $\rho_0 = 2.79$  g/cm<sup>3</sup>, shear modulus  $G = 0.286$  Mb, yield stress  $Y_0 = 0.0026$  Mb, and a Gruneisen equation of state with  $c_0 = 0.533$ ,  $s = 1.34$ , and  $\Gamma = 2.0$ . The domain is 0 to 1.5 cm in the direction of propagation.

At  $t = 2.0$ , the thermodynamic quantities (of which we show only density) are plotted vs distance in Figure 51 (a) to show both the plastic wave and the elastic precursor and on an expanded scale (b) for the precursor only. For both the elastic and plastic waves, the CGR result is sharper.

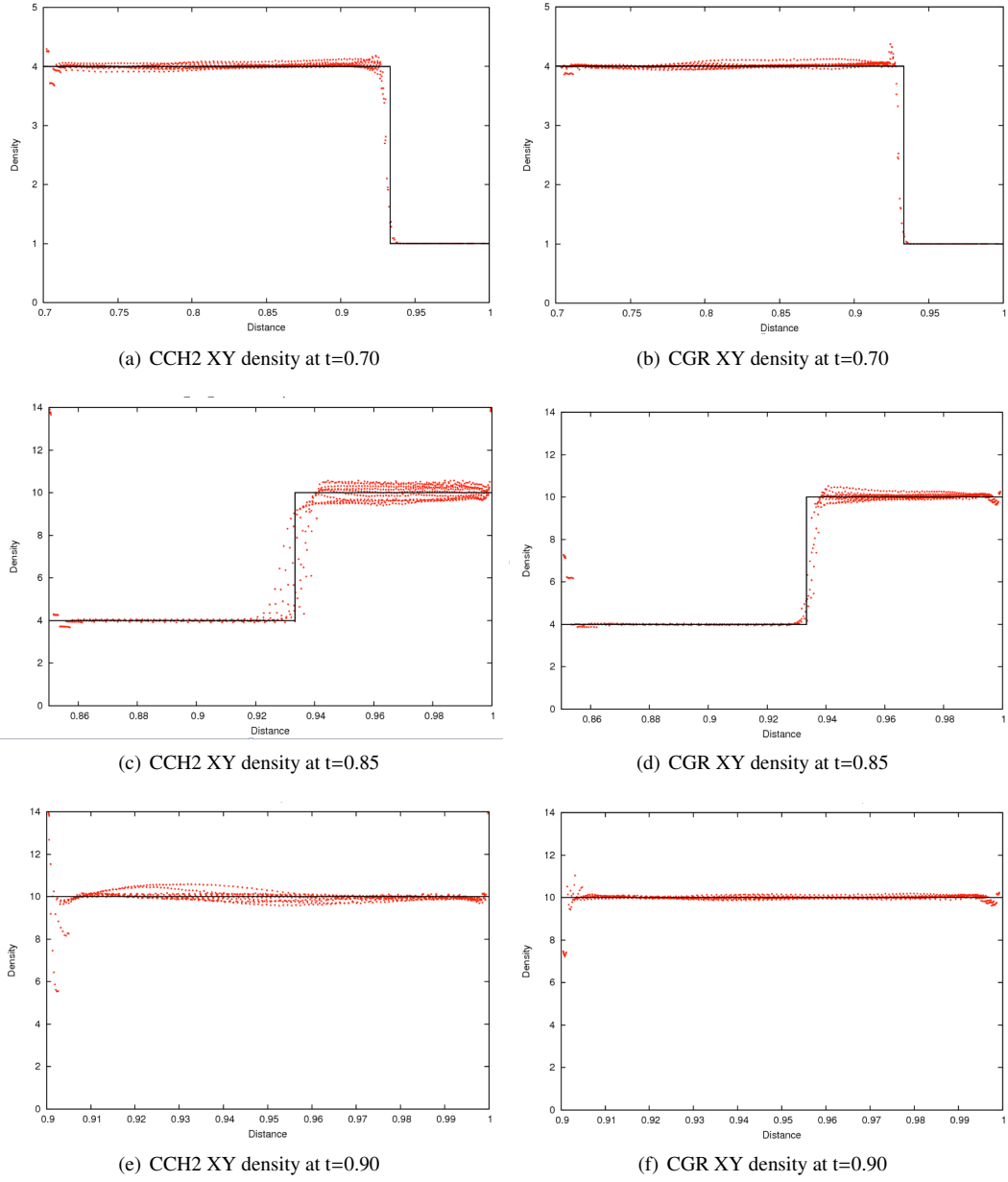
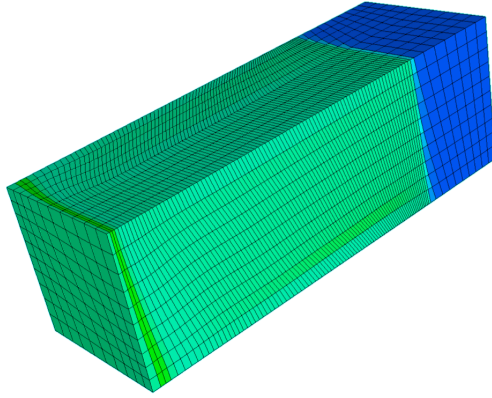
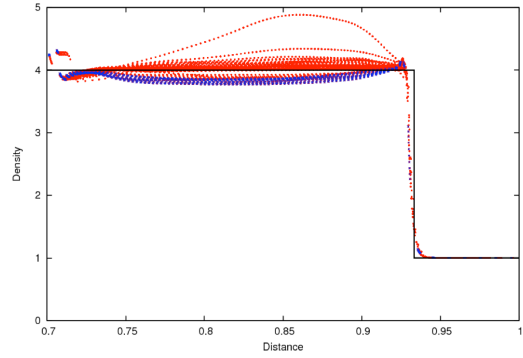


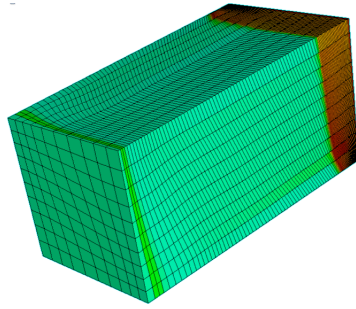
Figure 45: Saltzman 2D. Scatter plots of density for CCH2 and CGR calculations of the 2D problem at  $t=0.70$  before reflection at the wall, 0.85 after the reflection, and 0.90 at the time of the reflection from the piston face. Analytical solution shown in black.



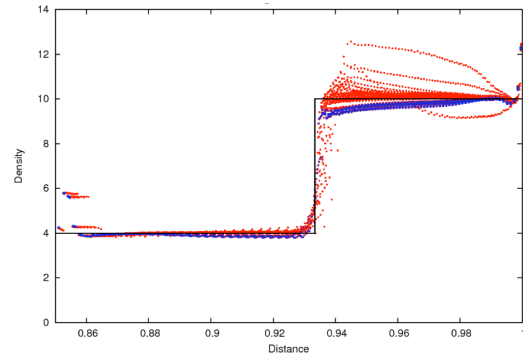
(a) CGR mesh at  $t=0.70$



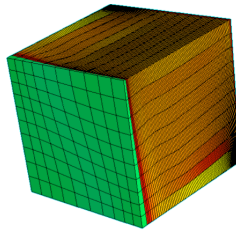
(b) CGR density at  $t=0.70$



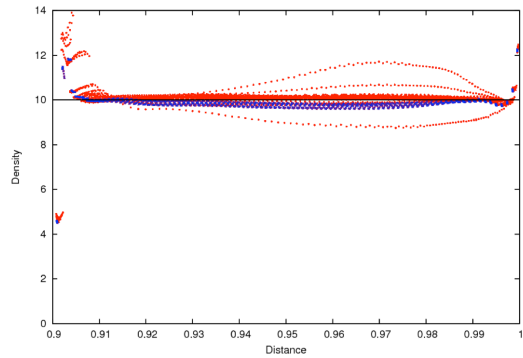
(c) CGR mesh at  $t=0.85$



(d) CGR density at  $t=0.85$



(e) CGR mesh at  $t=0.90$



(f) CGR density at  $t=0.90$

Figure 46: Saltzman 3D. Meshes and scatter plots of density for CGR calculations of the 3D problem at  $t=0.70$  before reflection at the wall, 0.85 after the reflection, and 0.90 at the time of the reflection from the piston face. Color in the mesh plots correspond to density on the scale of Figure 43(g). Density in all cells are indicated by red dots in the scatter plots. The blue dots correspond to cells near the central plane at  $j=6$ . Analytical solution shown in black.

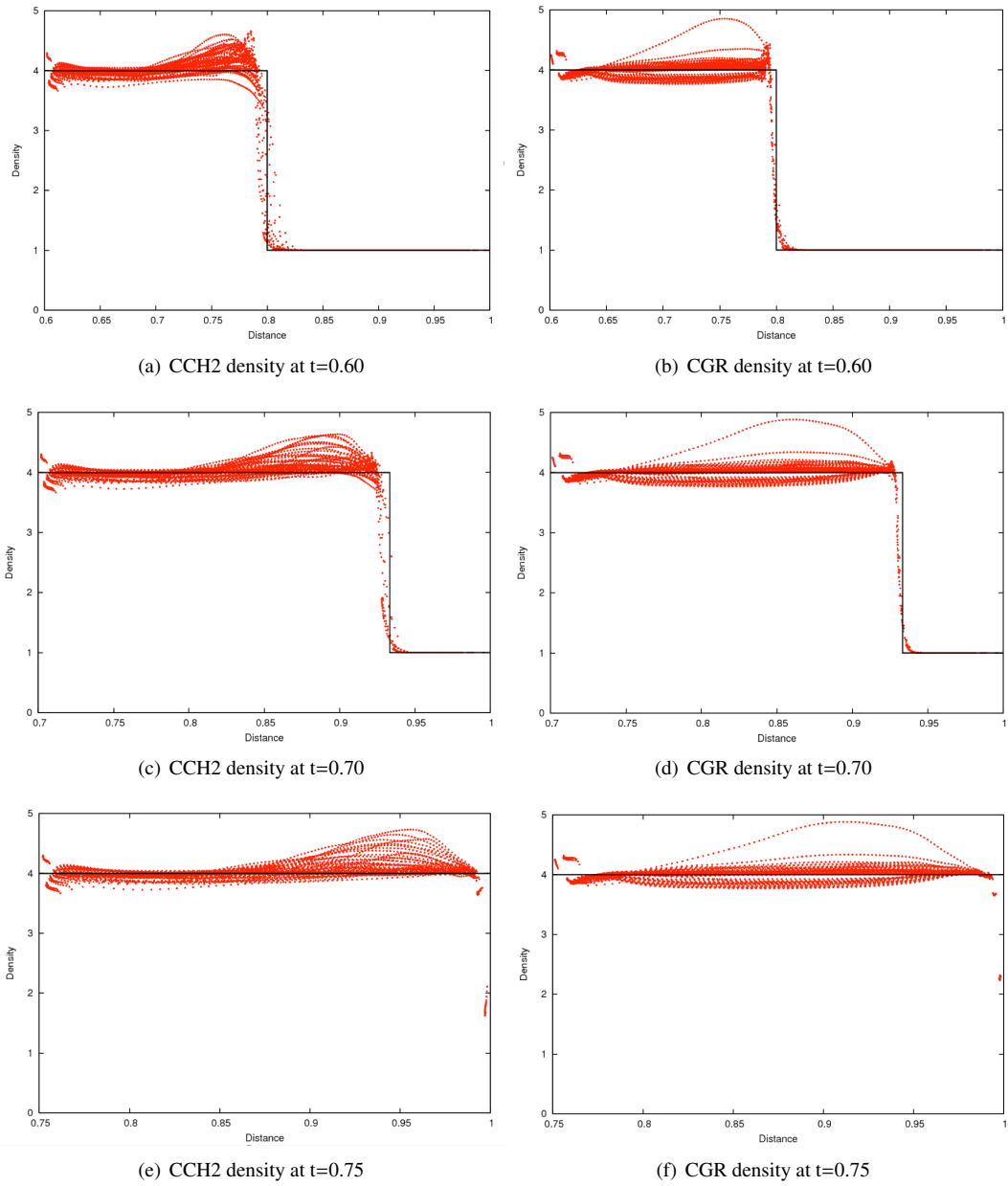


Figure 47: Saltzman. Scatter plots of density for CCH2 and CGR calculations of the 3D problem at times of 0.60, 0.70, and 0.75. Analytical solution shown in black.

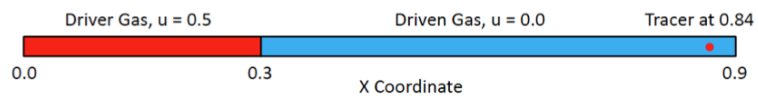


Figure 48: Adiabatic release. Initial configuration.

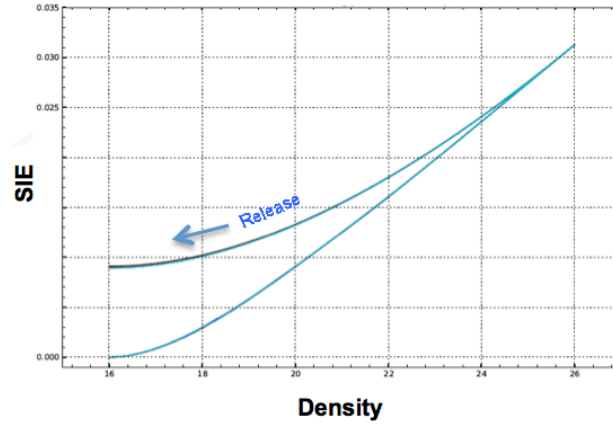


Figure 49: Adiabatic release. Specific internal energy (SIE) vs. density loading and release.

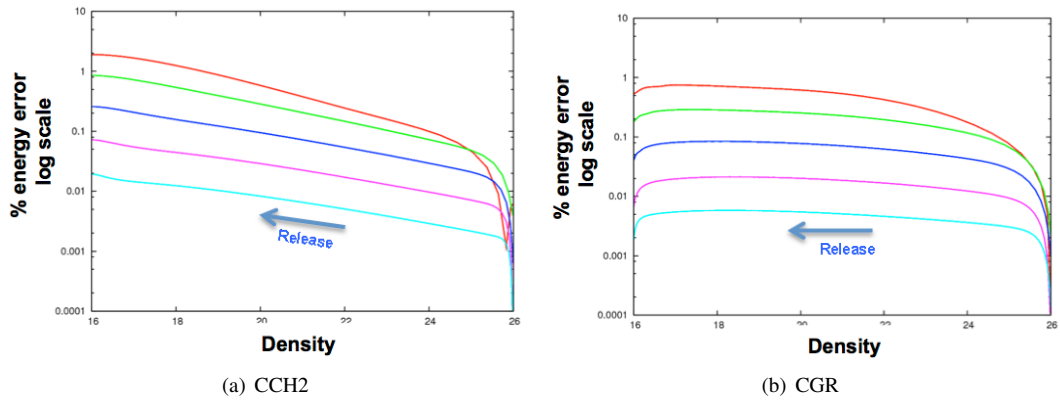


Figure 50: Adiabatic release. Percent energy error vs. distance for (a) CCH2 and (b) CGR for resolutions of 0.01 (red), 0.005 (green), 0.0025 (blue), 0.00125 (purple), and 0.000625 (aqua) cm.

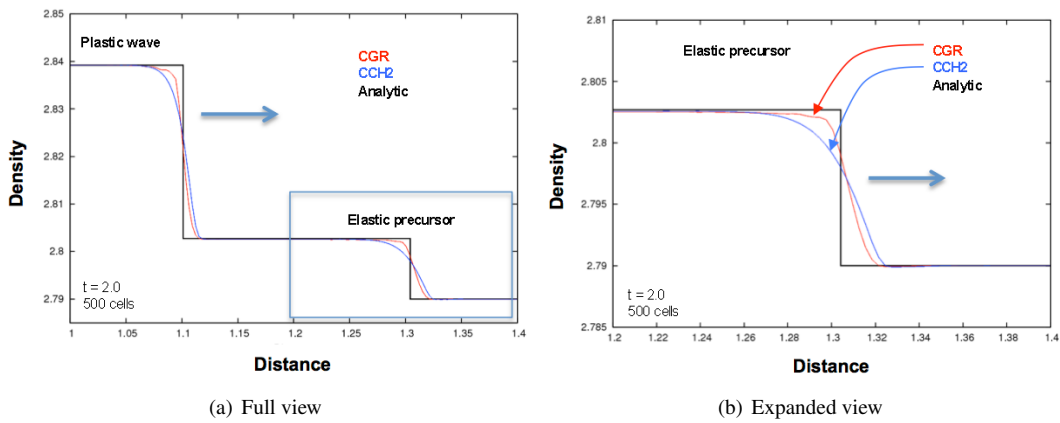


Figure 51: Elastic-plastic piston. Density vs. distance: CCH2 (blue), CGR (red), analytic (black). Box in (a) indicates region of elastic precursor that is expanded in (b).



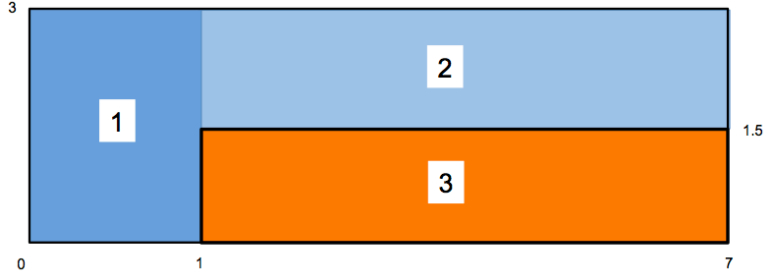


Figure 52: Triple point. Initial configuration.

## 7. Eulerian and ALE problems

### 7.1. Exact intersection remap (xALE)

The ALE problems were run using a scheme called xALE that is a second order, exact intersection remap method for unstructured polyhedral cells and is described in References [17, 19]. The method splits the operations into the usual Lagrange step followed by mesh optimization and an intersection based remap. Unlike swept face methods common in Eulerian and ALE schemes [52], intersection methods naturally couple across cell corners. We applied an efficient second-order method of remapping cell centered variables from one unstructured grid to another, based upon seminal work of Dukowicz and Ramshaw [37, 39, 89] and later extensions to unstructured polygonal grids [79], three dimensions [84], and reconstructed interfaces [83].

At start-up, the materials are painted into the background mesh. That is, one intersects the material geometry with the mesh and computes volume fractions of intersection for each mesh zone. After this, a volume-of-fluid interface reconstruction [116] is applied to recover linear interfaces in each multi-material zone. That is, each material in a multi-material zone is represented as a polygon and carries its own density, pressure, and internal energy. During the Lagrangian stage, we use Tipton's closure model [99, 95] to couple each material state in the multi-material zones. During the remapping stage we use multi-material remapping, which includes remapping of pure material sub-polygons (see, for example [61]). The rezoning strategy is a variation of Laplacian smoothing [51] the details of which are beyond the scope of this paper.

### 7.2. Triple Point problem

The triple point problem has its origins in a similarity solution to a shock interacting perpendicularly with a density discontinuity [40], giving rise to vorticity formation. It was cast as a reduced domain test problem in [94] and was mentioned but not specified in [64]. More recent Lagrange and ALE calculations were done by Maire [69]. It has since been calculated by a number of authors [46, 66, 59, 60, 67, 20, 17, 19, 18]. Although there is neither analytic nor converged numerical solution to the reduced domain problem, the problem is useful in comparing numerical algorithms.

The physical domain is shown in Figure 52, the object being material 3, and the shocked and unshocked fluids being regions 1 and 2 respectively. The problem is usually run in XY geometry. The calculation presented here was run to a time of 5.0 on a 100x200 grid in the vertical and horizontal directions respectively. All boundary conditions are reflective. As testing of mesh relaxation methods is not our objective, we run the problem with a Laplacian relaxer in an essentially Eulerian limit.

The density, pressure, and gamma are

$$\begin{aligned} \{\rho, p, \gamma\}_1 &= \{1, 1, 1.5\} \\ \{\rho, p, \gamma\}_2 &= \{0.125, 0.1, 1.5\} \\ \{\rho, p, \gamma\}_3 &= \{1, 0.1, 1.4\} \end{aligned} \tag{33}$$

with energies set appropriately. The initial velocity is zero everywhere.

At the contact discontinuity, a rarefaction forms in material 1, while shocks form in materials 2 and 3. Because of the different densities, shocks in the high and low density material travel at different velocities, giving rise to the

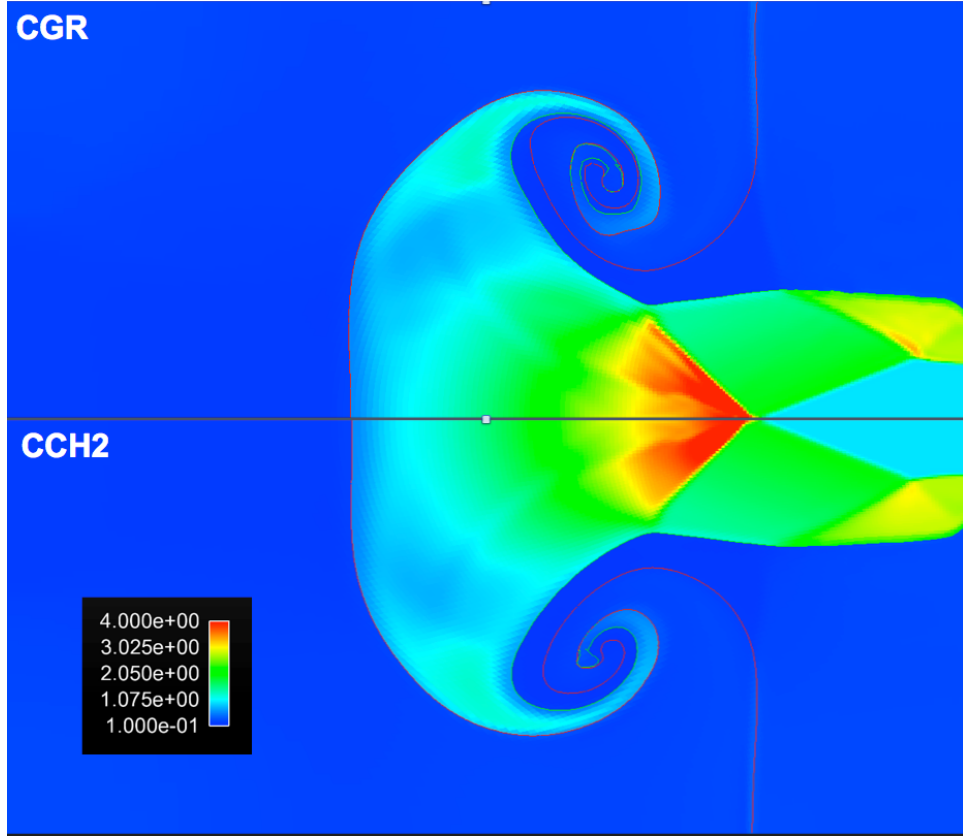


Figure 53: Triple point. Comparison of density contours at  $t=5.0$ . CGR (top), CCH2 (bottom)

formation of a vortex. As noted, there is no converged solution, but roll up in the tip will generally increase until perturbed by numerical error, giving rise to Kelvin-Helmholtz instabilities. A figure of merit in these calculations is the amount of roll up that can be calculated.

Figure 53 compares density contours for CGR (top) and CCH2 (bottom) calculations at a  $t=5.0$ . The results are similar, but the CGR calculation shows more detail in the red shock structure and in the tip roll up. The details of the tip region are more clearly seen in the expanded views of Figure 54. In the figure, the reconstructed interface between material 1 and other materials is red, while the interface between materials 2 and 3 is green. The CGR calculation shows an additional 180 degrees of rotation on the same mesh.

### 7.3. Helium bubble

This problem corresponds to the interaction of a shock wave with a cylindrical helium bubble surrounded by air. The problem is based on an experiment [50] and published calculations include [87, 46, 65]. The experiment involved a planar Mach  $M = 1.25$  shock wave through air interacting with a suspended spherical helium bubble with initial radius  $R_{He} = .025$  m within a test chamber with a 0.089 m square cross section.

The experimental Schlieren image times in [50] are relative to the time when the shock first reaches the bubble. A  $M = 1.25$  shock results in a shock speed  $u_{shock} = 428.9$  m/s in air which will propagate from the piston to the bubble in time  $t_{shift} = 1.807 \cdot 10^{-4}$  s. To model the experiment, we constructed synthetic Schlieren-like images. Schlieren shadowgraphy is based on the deflection of light by a refractive index gradient that is in turn directly related to the density gradient. See Appendix B for a description of the process used to generate the synthetic images.

Both materials are initially at rest. To simulate this in a 2D cylindrical coordinate system, the test chamber wall is assumed to be rigid with a cylindrical radius of 0.0445 m. A cylindrical computational domain was chosen with  $[0, 0.0445]$  m in the  $r$  direction and in the  $z$  direction  $[-0.1, 0.4]$  m with the helium bubble centered initially at the

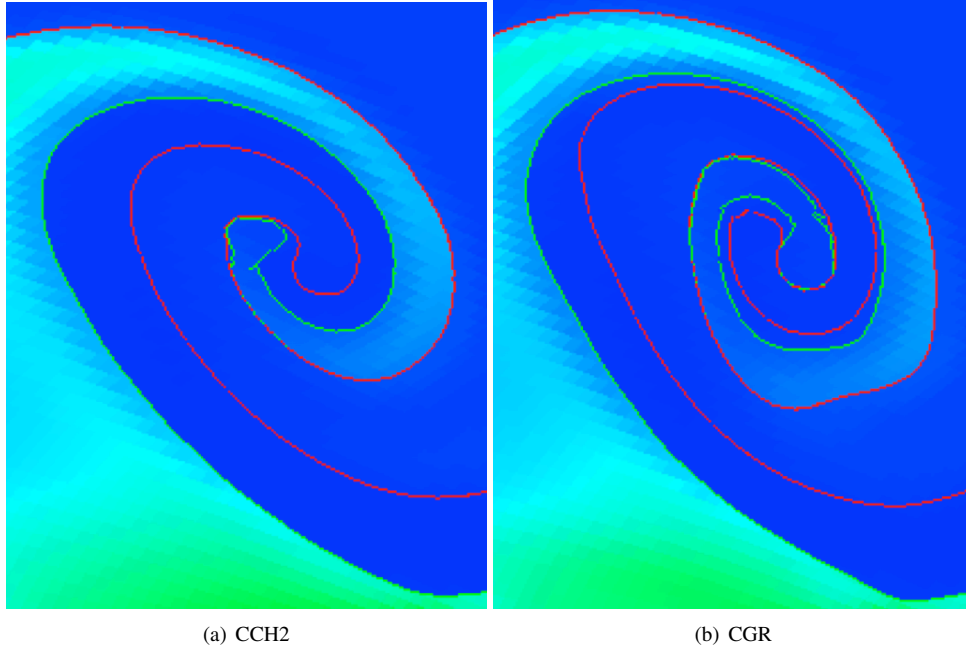


Figure 54: Triple point. Expanded view of vortices for CCH2 (a) and CGR (b) showing increased rotation in the latter. Referring to Fig. 52, the reconstructed interface between material 1 and other materials is red, while the interface between materials 2 and 3 is green.

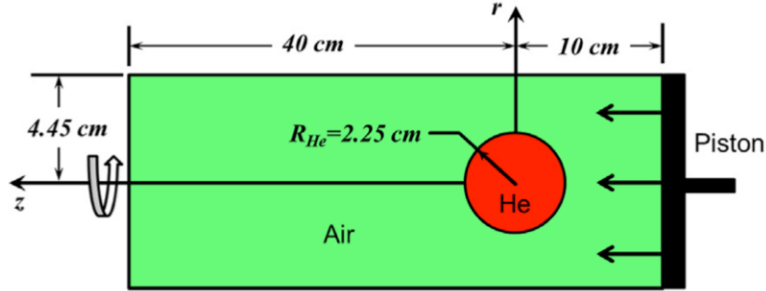


Figure 55: He bubble. Initial configuration.

origin. The domain is driven by a piston acting on the  $z = -0.1$  plane. The  $z$ -velocity of the mesh points along this surface is prescribed as a constant velocity boundary condition with  $u_{piston} = 128.678$  m/s which is the shocked particle velocity of the air, determined from the Rankine-Hugoniot jump relations, Mach number  $M$ , and the properties of the air.

This is a two-material calculation. At start-up, the bubble and air are painted into the background mesh. Both are polytropic gasses with

$$\begin{aligned} \{\gamma_{He}, \rho_{He}, P_{He}\} &= \{1.648, 0.2163 \text{ kg/m}^3, 10^5 \text{ Pa}\} \\ \{\gamma_{air}, \rho_{air}, P_{air}\} &= \{1.4, 1.189 \text{ kg/m}^3, 10^5 \text{ Pa}\} \end{aligned}$$

The mesh is a logically rectangular grid with  $80 \times 600$  cells. Reflecting boundary conditions are applied to the remaining mesh boundaries.

In Figures 56 and 57, we present qualitative comparison of our calculations with experimental results from [50]. Due to the limited data, uncertainty in the scale of the images, and questionable sphericity of the bubble, it is difficult to make more quantitative comparisons. In Figure 56, synthetic Schlieren images from the CGR (center) and CCH2

(right) calculations are compared to the experimental images at 5 times. For the first 3 times, the images are similar, but begin to differ markedly at times of 538 and 788  $\mu s$ . The CGR images at the latter times are in excellent agreement with the experiment, whereas the CCH2 are not.

In Figure 57, the bottom of each calculated image shows the material while the top is a color plot of density gradient. In the density gradient plots, the shock locations for both CGR and CCH2 are in good agreement with those in the Schlieren images. However, the shocks can be seen to dissipate at the later times in the CCH2 results.

## 8. Conclusions

Our goal was to address a justifiable perception that CCH is too dissipative. We have done so, as demonstrated on a wide variety of test problems with results that are among the best we have seen. To do this, we introduced a new CCH discretization called corner gradient reconstruction (CGR). CGR differs from traditional CCH only in the reconstruction step. Unlike higher order reconstructions, it does not require solving large systems of equations in each cell. The method extends trivially to 3D and is applicable to solids and fluids. CGR offers improved directional accuracy by virtue of corner coupling, provides significant reduction in dissipation, especially for smooth flows, and performs comparably or better for shock dominated flows. The computational cost is comparable to that of traditional CCH2.

## 9. Acknowledgments

We gratefully acknowledge the support of the U.S. Department of Energy through the LANL LDRD and ASC Programs for this work. We also acknowledge the programmatic support of Scott Doebling, Jimmy Fung, Tom Gianakon, and Misha Shashkov, as well as very useful discussions with Andrew Barlow, Len Margolin, Shiv Sambasivan, and Misha Shashkov. Acknowledgements would not be complete without also recognizing the seminal contributions of Bruno Després and Pierre-Henri Maire to cell-centered methodology. The Los Alamos unlimited release number is: LA-UR-14-28809.

## Appendix A. Solid constitutive model

In the calculations presented, we use an isotropic hypo-elastic model based upon the Wilkins formulation [113] in which the Cauchy stress is decomposed into a mean stress  $p = -\frac{1}{3}tr(\sigma)$  and deviatoric components  $\mathbf{s} = \sigma + p\mathbf{I}$ . Similarly the strain rate is decomposed into volumetric  $\dot{\epsilon}^V = tr(\dot{\epsilon}) = \frac{\dot{v}}{v}$  and deviatoric components  $\dot{\mathbf{e}} = \dot{\epsilon} - \frac{1}{3}\dot{\epsilon}^V\mathbf{I}$ . For isotropic materials, the stiffness tensor  $\mathbf{D}$  reduces to a simple form involving only bulk and shear moduli. When the plastic flow is entirely deviatoric (a reasonable approximation for most non-porous metals), the deviatoric and volumetric stress rates are entirely decoupled and can be updated separately. The mean stress can then be obtained from an equation of state function  $p = P(v, e)$  and the deviatoric stress from a rate equation.

For the calculations shown, the equation of state was a Gruneisen form [31] derived from a linear relationship between the shock and particle velocities,  $U_s = c_0 + sU_p$ , that results in Hugoniot pressure  $P_H(\eta) = \frac{\rho_0 c_0^2 \eta}{(1-s\eta)^2}$  and energy  $E_H(\eta) = \frac{\eta P_H}{2\rho_0}$  in which  $\eta = 1 - v/v_0$ . The equation of state is offset from the Hugoniot according to

$$p(\eta, e) = P_H + \frac{\Gamma}{v}(e - E_H) \quad (\text{A.1})$$

The Jaumann deviatoric stress rate is obtained from

$$\dot{\mathbf{s}} = 2G(\dot{\mathbf{e}} - \dot{\mathbf{e}}^P) - \mathbf{s}\dot{\omega} + \dot{\omega}\mathbf{s} \quad (\text{A.2})$$

which is a sum of two components, one proportional to the current rate of deformation and the other resulting from the existing stress rotating with the material. In this equation, the elastic shear modulus  $G$  is typically a function of density and temperature.

The stress rate in Equation A.2 is calculated using a split operation in which the Jaumann rotational terms are applied at the start of the time increment and the elastic contribution  $\dot{\mathbf{s}}^E = 2G(\dot{\mathbf{e}} - \dot{\mathbf{e}}^P)$  is computed using a *radial*

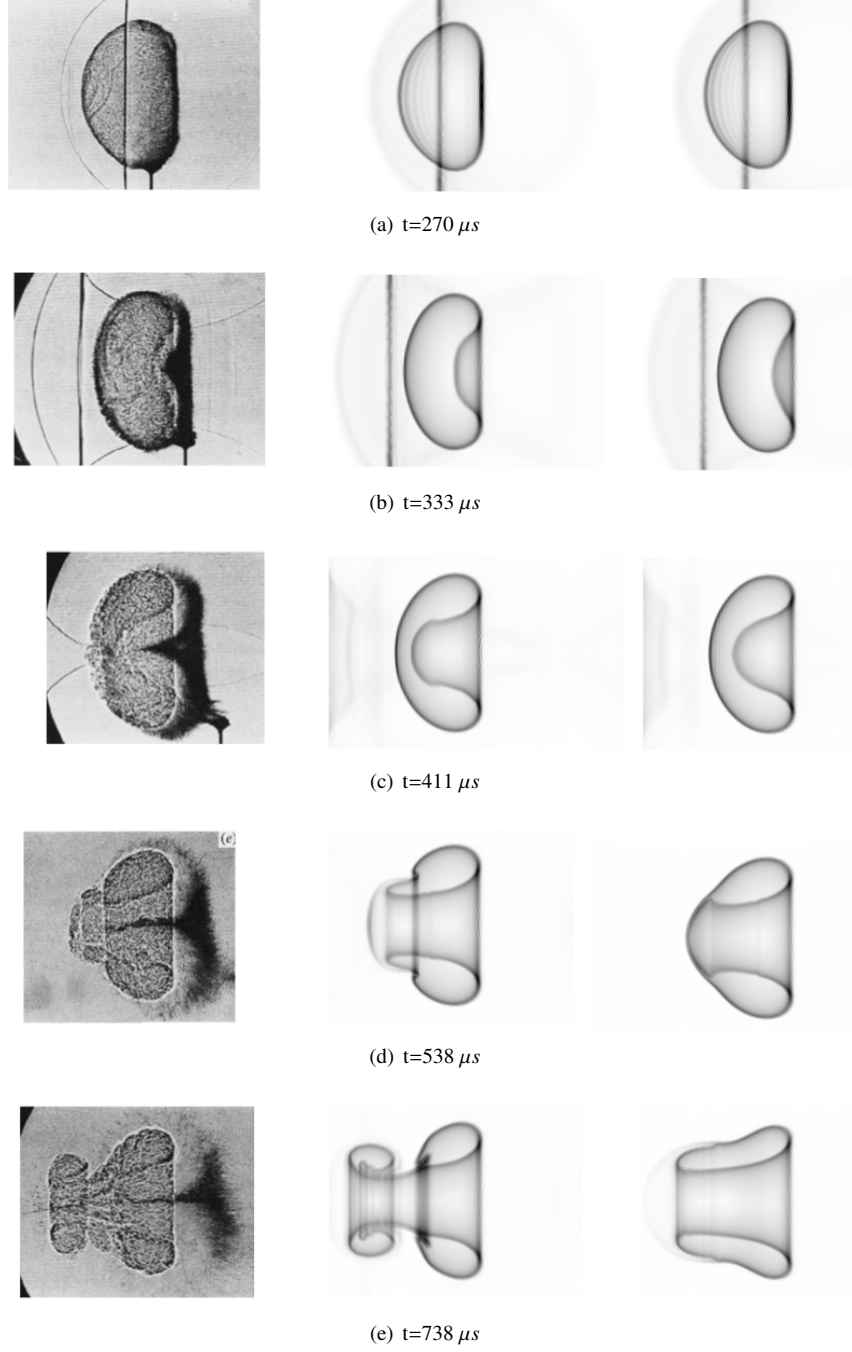


Figure 56: He bubble. Comparison of Schlieren images (left) from [50] with synthetic Schlieren images from CGR (center) and CCH2 (right) at simulation times of 270, 333, 411, 538 and 788  $\mu s$ .

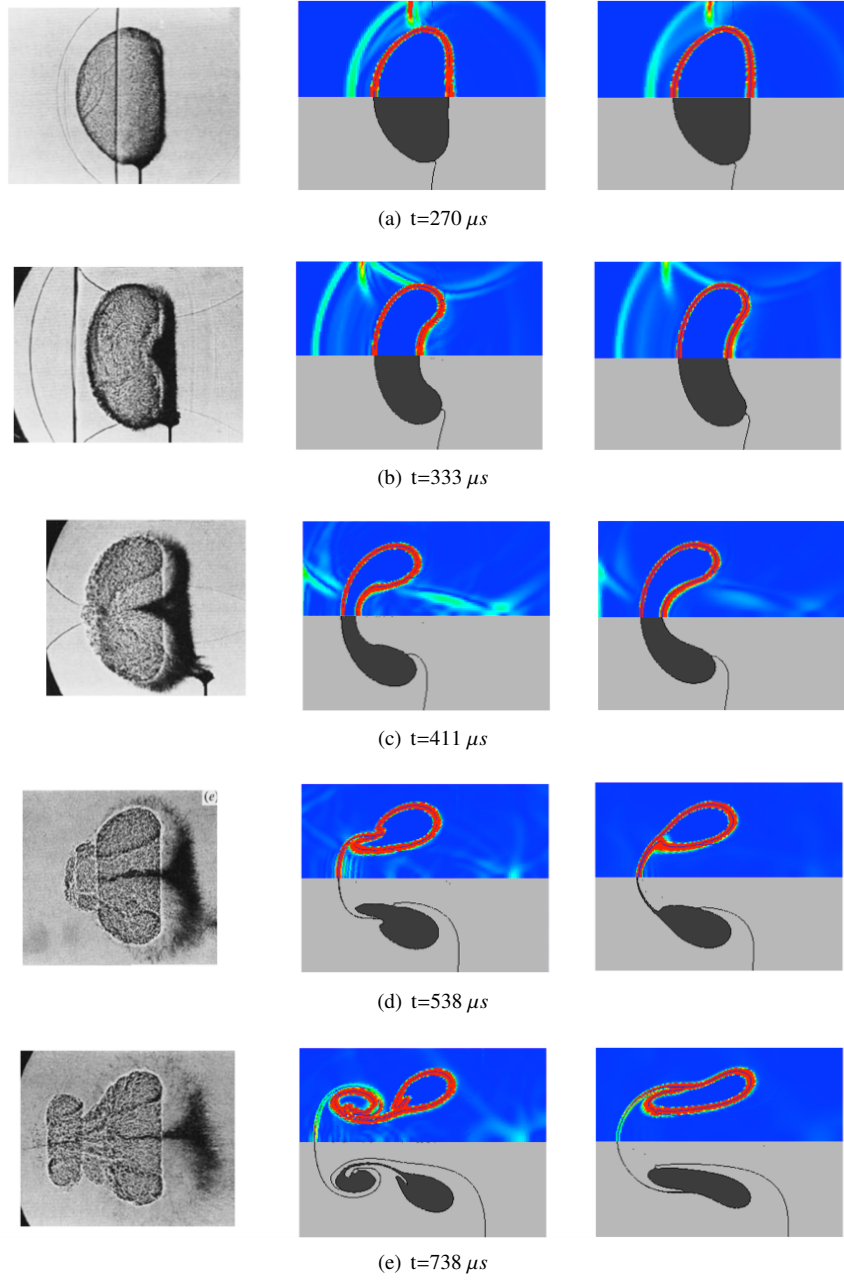


Figure 57: He bubble. Comparison of Schlieren images (left) from [50] with images from CGR (center) and CCH2 (right) at simulation times of 270, 333, 411, 538 and 788  $\mu s$ . The top of each image is colored by density gradient and the bottom by material (dark for He and light for air).

*return* procedure. Radial return is a simplified flow rule that is valid for materials in which the plastic strain increments are entirely deviatoric and directionally aligned with the deviatoric stress. Under these conditions, the final stress is a scaled version of a trial stress that is computed under the assumptions of no plastic flow  $\dot{\mathbf{s}}^t = 2G\dot{\mathbf{e}}$ .

The term *equivalent* is used to describe scalar quantities derived from the second deviatoric invariant of a tensor. An equivalent trial stress is defined from the second invariant of the trial stress and compared to the radius of the yield surface in the octahedral plane. The radius is defined as an increasing function of equivalent plastic strain  $\varepsilon_{eq}^P$  to be defined later

$$Y(\varepsilon_{eq}^P) = Y_0 + Y_H \varepsilon_{eq}^P \quad (\text{A.3})$$

Here,  $Y_0$  is the radius of the initial yield surface and  $Y_H$  is the hardening modulus. If the yield surface is exceeded,  $s_{eq}^t > Y(\varepsilon_{eq}^P)$ , the final deviatoric stress tensor is obtained by scaling

$$\mathbf{s} = \mathbf{s}^t \frac{Y(\varepsilon_{eq}^P)}{s_{eq}^t} \quad (\text{A.4})$$

The equivalent plastic strain is the integral  $\varepsilon_{eq}^P = \int \dot{\varepsilon}_{eq}^P dt$  of a strain rate that is formally  $\dot{\varepsilon}_{eq}^P = \sqrt{\frac{2}{3} \dot{\mathbf{e}}^P : \dot{\mathbf{e}}^P}$ . With radial return, the computation of the individual components of the plastic strain rate tensor is unnecessary, and the equivalent plastic strain rate is computed directly from

$$\dot{\varepsilon}_{eq}^P = \frac{s_{eq}^t - Y(\varepsilon_{eq}^P)}{3G \delta t} \quad (\text{A.5})$$

Strict enforcement of the preceding equations requires iteration because the system is implicit in equivalent plastic strain. In practice, the previously computed equivalent plastic strain is used in the hardening rule.

## Appendix B. Synthetic Schlieren images

The synthetic Schlieren images were generated as follows. Rays normal to the r-z plane are intersected with the volume of revolution about the z-axis of all zones in the mesh. One ray is generated for each mesh zone such that the ray intersects the r-z plane at that cell's center. The attenuation for each ray can therefore be stored as a cell-centered quantity. This cell field is plotted in visualization software to produce the images.

The ray-cell intersection length  $\Delta x = x_2 - x_1$  is computed for every zone the ray intersects. This is shown in Figure B.58(a). The 2D zonal density gradient  $\nabla \rho_{rz}$  computed at the cell center  $\{r, z\}$  is rotated by  $\theta = (\theta_1 + \theta_2)/2$  about the z-axis to obtain the 3D density gradient  $\nabla \rho_{3D}$ . The density gradient normal to the ray,  $\nabla \rho_{proj}$  is obtained by projecting  $\nabla \rho_{3D}$  onto the r-z plane. See Figures B.58(b) and (c).

The attenuation of ray  $n$  from one ray-cell intersection is

$$\alpha_n^z = \|\nabla \rho_{proj}\| \Delta x$$

so that the total attenuation for ray  $n$  is then

$$\alpha_n = \sum_z^n \alpha_n^z$$

where the sum is over the set of zones intersected by ray  $n$ . This process is repeated for all rays to produce the field that is plotted in the images. An inverse grayscale color palette was used such that the largest attenuation values are black, the least are white and intermediate values are varying shades of gray.

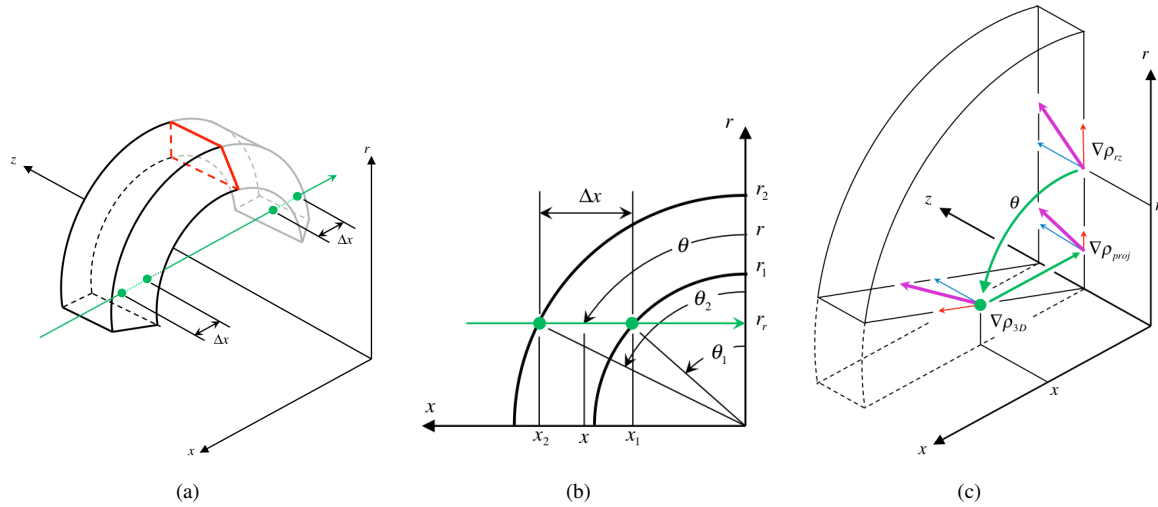


Figure B.58: Schlieren image generation

## References

- [1] R. Abgrall, R. Loubere, and J. Ovardia. A Lagrangian discontinuous Galerkin-type method on unstructured meshes to solve hydrodynamics problems. *Int. J. Numer. Meth. Fluids*, 44:645–663, 2004.
- [2] F.L. Addessio, J.R. Baumgardner, J.K. Dukowicz, N.L. Johnson, B.A. Kashiwa, R.M. Rauenzahn, and C. Zemach. CAVEAT: A computer code for fluid dynamics problems with large distortion and internal slip. Technical Report LA-10613, Los Alamos National Laboratory, 1990.
- [3] A.J. Barlow and P.L. Roe. A cell centered Lagrangian Godunov scheme for shock hydrodynamics. *Comput. Fluids*, 46(1):133–136, 2011.
- [4] T.J. Barth and D.C. Jespersen. The design and application of upwind schemes on unstructured meshes. In *AIAA paper 89-0366, 27th Aerospace Sciences Meeting, Reno, Nevada*, 1989.
- [5] G. Bazan and R.N. Rieben. Adiabatic release test problem description. Technical Report LLNL-PRES-463883, Lawrence Livermore National Laboratory, 2010.
- [6] W. Boscheri and M. Dumbser. A direct arbitrary Lagrangian-Eulerian ADER-WENO finite volume scheme on unstructured tetrahedral meshes for conservative and non-conservative hyperbolic systems in 3D. *J. Comput. Phys.*, 275:484–523, 2014.
- [7] T. Buffard and Stéphane Clain. Monoslope and multislope MUSCL methods for unstructured meshes. *J. Comput. Phys.*, 229:3745–3776, 2010.
- [8] D.E. Burton. Conservation of energy, momentum, and angular momentum in Lagrangian staggered-grid hydrodynamics. Technical Report UCRL-JC-105926, available from the author, Lawrence Livermore National Laboratory, November 1990. NECDC 1990: Nuclear Explosives Code Developers’ Conference, Monterey, California, November 6-9, 1990.
- [9] D.E. Burton. Exact conservation of energy and momentum in staggered-grid hydrodynamics with arbitrary connectivity. In *Advances in the Free Lagrange Method*. Springer Verlag, NY, 1990. Lawrence Livermore National Laboratory Report UCRL-JC-104258, June 1990.
- [10] D.E. Burton. Connectivity structures and differencing techniques for staggered grid free Lagrange hydrodynamics. In R. Vichnevetsky, D. Knight, and G. Richter, editors, *Seventh IMACS International Conference on Computer Methods for Partial Differential Equations, New Brunswick, NJ, June 1992*, June 1992. Lawrence Livermore National Laboratory, UCRL-JC-110555.
- [11] D.E. Burton. Consistent finite-volume discretization of hydrodynamic conservation laws for unstructured grids. Technical Report UCRL-JC-118788, available from the author, Lawrence Livermore National Laboratory, October 1994. NECDC 1994: Eighth Nuclear Explosives Code Developers Conference, Las Vegas, NV, October 1994.
- [12] D.E. Burton. Multidimensional discretization of conservation laws for unstructured polyhedral grids. Technical Report UCRL-JC-118306, available from the author, Lawrence Livermore National Laboratory, August 1994. SAMGOP-94: 2nd International Workshop on Analytical Methods and Process Optimization in Fluid and Gas Mechanics, VNIIEF, Holiday Base, Arzamas-16, Russia, September 10-16, 1994.
- [13] D.E. Burton, T.C. Carney, N. R. Morgan, S.K. Sambastivan, and M.J. Shashkov. A cell-centered Lagrangian Godunov-like method for solid dynamics. *Comput. Fluids*, 83:33–47, 2013.
- [14] D.E. Burton, T.C. Carney, N. R. Morgan, and M.J. Shashkov. Exploration of a cell-centered Lagrangian hydrodynamics method. Technical Report LA-UR-11-01294, Los Alamos National Laboratory, February 2011. SIAM Conference on Computational Science and Engineering, Reno, NV, U.S.A, February 2011.
- [15] D.E. Burton, T.C. Carney, and N.R. Morgan. On the question of area weighting in cell-centered hydrodynamics. Technical Report LA-UR-13-23155, Los Alamos National Laboratory, April 2013.
- [16] D.E. Burton, T.C. Carney, N.R. Morgan, and M.A. Kenamond. Compendium of CCH and xALE test problems. Technical Report LA-UR-13-24115, Los Alamos National Laboratory, April 2013.
- [17] D.E. Burton, M.A. Kenamond, T.C. Carney, N.R. Morgan, and J. Fung. A cell-centered Godunov-like ALE remap scheme (RALE). Techni-



- cal Report LA-UR-12-22849, Los Alamos National Laboratory, October 2012. NECDC 2012: 2012 Nuclear Explosive Code Development Conference, Livermore, October 22-26, 2012.
- [18] D.E. Burton, M.A. Kenamond, T.C. Carney, N.R. Morgan, and J. Fung. Corner gradient reconstruction (CGR) in Lagrange cell-centered hydro (CCH). Technical Report LA-UR-14-27503, Los Alamos National Laboratory, September 2014. NECDC 2014: 2014 Nuclear Explosive Code Development Conference, Livermore, October 20-24, 2014.
  - [19] D.E. Burton, M.A. Kenamond, N.R. Morgan, T.C. Carney, and M.J. Shashkov. An intersection based ALE scheme (xALE) for cell centered hydrodynamics (CCH). Technical Report LA-UR-13-26756, Los Alamos National Laboratory, August 2013. MultiMat 2013: International Conference on Numerical Methods for Multi-Material Fluid Flows, San Francisco, CA September 2-6, 2013.
  - [20] D.E. Burton, N.R. Morgan, T.C. Carney, and S. Sambasivan. A cell-centered Godunov-like ALE method for solid dynamics. Technical Report LA-UR-12-20613, Los Alamos National Laboratory, April 2012. The 9th International Conference on New Models and Hydrocodes for Shock Processes in Condensed Matter, London, April 2012.
  - [21] D.E. Burton and M.J. Shashkov. Mimetic formulation of cell-centered Lagrangian hydrodynamics (CCH). Technical Report LA-UR-09-05875, Los Alamos National Laboratory, August 2009. MultiMat 2009: Numerical Methods for Multi-Material Fluids and Structures, Pavia, Italy, September 21-25, 2009.
  - [22] E. J. Caramana, C.L. Rousculp, and D.E. Burton. A compatible, energy and symmetry preserving Lagrangian hydrodynamics algorithm in three-dimensional cartesian geometry. *J. Comput. Phys.*, 157:89–119, January 2000. doi: 10.1006/jcph.1999.6368.
  - [23] E. J. Caramana and P. P. Whalen. Numerical preservation of symmetry properties of continuum problems. *J. Comput. Phys.*, 141:174–198, April 1998.
  - [24] E.J. Caramana, D.E. Burton, M.J. Shashkov, and P.P. Whalen. The construction of compatible hydrodynamics algorithms utilizing conservation of total energy. *J. Comput. Phys.*, 146:227–262, 1998. doi: 10.1006/jcph.1998.6029. URL <http://portal.acm.org/citation.cfm?id=302638.302658>.
  - [25] G. Carré, S. Del Pino, B. Després, and E. Labourasse. A cell-centered Lagrangian hydrodynamics scheme on general unstructured meshes in arbitrary dimension. *J. Comput. Phys.*, 228:5160–5183, 2009.
  - [26] M.R. Charest, T.R. Canfield, N.R. Morgan, J. Waltz, and J.G. Wohlbiel. A high-order vertex-based central eno finite-volume scheme for three-dimensional compressible flows. *Comput. Fluids*, 114:172–192, 2015.
  - [27] J. Cheng and C-W. Shu. A third-order conservative Lagrangian type scheme on curvilinear meshes for the compressible Euler equations. *Commun. Comput. Phys.*, 4:1008–1024, 2008.
  - [28] S.V. Coggeshall. Analytic solutions of hydrodynamics equations. *Physics of Fluids A*, 3:760–769, 1991.
  - [29] S.V. Coggeshall and J. Meyer ter Vehn. Group-invariant solutions of multidimensional hydrodynamics. *J. Math. Phys.*, 33:3585, 1992.
  - [30] P. Colella and P. R. Woodward. The piecewise-parabolic method (PPM) for gas-dynamical simulations. *J. Comput. Phys.*, 54:174–201, 1984.
  - [31] W.C. Davis. Shock waves; rarefaction waves; equations of state. In J.A. Zukas and W.P. Walters, editors, *Explosive Effects and Applications*. Springer, 1998.
  - [32] B. Després. Weak consistency of the cell-centered Lagrangian GLACE scheme on general meshes in any dimension. *Comput. Methods Appl. Mech. Engr.*, 199:2669–2679, 2010.
  - [33] B. Després and C. Mazeran. Lagrangian gas dynamics in two dimensions and Lagrangian systems. *Arch. Rational Mech. Anal.*, 178:327–372, 2005.
  - [34] V.A. Dobrev, T.V. Kolev, and R.N. Rieben. High-order curvilinear finite element methods for Lagrangian hydrodynamics. *SIAM J. Sci. Comput.*, 34(5):B606B641, 2012.
  - [35] D. Drikakis, C. Fureby, F. Grinstein, and D. Youngs. Simulation of transition and turbulence decay in the Taylor-Green vortex. *J. Turbulence*, 8:1–12, 2007.
  - [36] J. K. Dukowicz and B. Meltz. Vorticity errors in multidimensional Lagrangian codes. *J. Comput. Phys.*, 99:115, 1992.
  - [37] J.K. Dukowicz. Conservative rezoning (remapping) for general quadrilateral meshes. *J. Comput. Phys.*, 54:411–424, 1984.
  - [38] J.K. Dukowicz. A general, non-iterative Riemann solver for Godunov’s method. *J. Comput. Phys.*, 61:119–137, 1985.
  - [39] J.K. Dukowicz, M.C. Cline, and F.S. Addessio. A general topology method. *J. Comput. Phys.*, 82:2963, 1989.
  - [40] V.F. D’yadechko. Some new method for numerical solving non stationary gas dynamic problems. *USSR Comput. Math. and Math. Phys.*, 5:680–688, 1965.
  - [41] D.P. Flanagan and T. Belytschko. A uniform strain hexahedron and quadrilateral with orthogonal hourglass control. *Int. J. for Num. Meth. in Engr.*, 17:679–706, 1981.
  - [42] C. Fochesato, R. Loubère, R. Motte, and J. Ovidia. Adaptive subdivision piecewise linear interface calculation(ASPLIC) for 2D multi-material hydrodynamic simulation codes. *Int. J. Numer. Meth. Fluids*, 77:418–439, 2015.
  - [43] J. Fung, M. Kenamond, and D. Burton. Spherical geodesic mesh generation. Technical Report LA-UR-07-2801, Los Alamos National Laboratory, November 2007. LLNL Workshop on Advanced Numerical Methods for Lagrangian Hydrodynamics, Livermore, November 2007.
  - [44] J. Fung, M. Kenamond, and D. Burton. Spherical geodesic mesh generation. Technical Report LA-UR-08-4835, Los Alamos National Laboratory, July 2008. 2008 SIAM Annual Meeting, Multi-Material Fluid Flows, July 2008.
  - [45] S. Galera, J. Breil, and P.-H. Maire. A 2D unstructured multi-material cell-centered arbitrary Lagrangian-Eulerian (CCALE) scheme using MOF interface reconstruction. *Comput. Fluids*, 46:237–244, 2010.
  - [46] S. Galera, P.-H. Maire, and J. Breil. A two-dimensional unstructured cell-centered multi-material ALE scheme using VOF interface reconstruction. *J. Comput. Phys.*, 229:5755–5787, 2010.
  - [47] S.K. Godunov. A finite-difference method for the numerical computation and discontinuous solutions of the equations of fluid dynamics. *Mat. Sb.*, 47:271–306, 1959.
  - [48] S.K. Godunov. Reminiscences about difference schemes. *J. Comput. Phys.*, 153:625, 1999.
  - [49] S.K. Godunov, A. Zabrodine, M. Ivanov, A. Kraiko, and G. Prokopov. Rsolution numerique des problemes multidimensionnels de la dynamique des gaz. *Mir*, 1979.

- [50] J.F. Haas and B. Sturtevant. Interaction of weak-shock waves. *J. Fluid Mech.*, 181:4176, 1987.
- [51] G.A. Hansen, R.W. Douglass, and A. Zardecki. *Mesh Enhancement: Selected Elliptic Methods, Foundations, and Applications*. Imperial College Press, 2005.
- [52] C.W. Hirt, A. Amsden, and J.L. Cook. An arbitrary Lagrangian-Eulerian computing method for all flow speeds. *J. Comput. Phys.*, 14:227–253, 1974.
- [53] B.P. Howell and G.J. Ball. A free-Lagrange augmented Godunov method for the simulation of elastic-plastic solids. *J. Comput. Phys.*, 175:128–167, 2002.
- [54] J.R. Kamm, J.S. Brock, S.T. Brandon, D.L. Cotrell, B. Johnson, P. Knupp, W.J. Rider, T.G. Trucano, and V.G. Weirs. Enhanced verification test suite for physics simulation codes. Technical Report LA-14379, Los Alamos National Laboratory, September 2008.
- [55] R. Kidder. Laser compression of matter: optical power and energy requirements. *Nucl. Fusion*, 14:797–803, 1974.
- [56] R. Kidder. Laser-driven compression of hollow shells: power requirements and stability limitations. *Nucl. Fusion*, 16:3–14, 1974.
- [57] R. Kidder. Theory of homogeneous isentropic compression and its application to laser fusion. *Nucl. Fusion*, 14:53–60, 1974.
- [58] G. Kluth and B. Després. Discretization of hyperelasticity on unstructured mesh with a cell-centered Lagrangian scheme. *J. Comput. Phys.*, 229:9092–9118, 2010.
- [59] M. Kucharik, R.V. Garimella, S.P. Schofield, and M.J. Shashkov. A comparative study of interface reconstruction methods for multi-material ale simulations. Technical Report LA-UR-09-01324, Los Alamos National Laboratory, 2009.
- [60] M. Kucharik, R.V. Garimella RV, S.P. Schofield, and M.J. Shashkov. A comparative study of interface reconstruction methods for multi-material ALE simulations. *J. Comput. Phys.*, 229:2432–2452, 2010.
- [61] M. Kucharik and M. Shashkov. One-step hybrid remapping algorithm for multi-material arbitrary Lagrangian-Eulerian methods. *J. Comput. Phys.*, 231:2851–2864, 2012.
- [62] V.F. Kuropatenko. On difference methods for the equations of hydrodynamics. In N.N. Jenenko, editor, *Difference Methods for Solutions of Problems of Mathematical Physics*, volume 116. American Mathematical Society, 1967.
- [63] R. Loubère. Une methode particulaire Lagrangienne de type Galerkin discontinu, application a la mecanque des fluides et l’interaction laser/plasma. Technical report, Universite de Bordeaux, 2002. Ph.D. thesis.
- [64] R. Loubère. Validation test case suite for compressible hydrodynamics computation. Unpublished notes, Los Alamos National Laboratory, 2005.
- [65] R. Loubère, P.-H. Maire, and M. Shashkov. ReALE: a reconnection-based arbitrary LagrangianEulerian method in cylindrical geometry. *Comput. Fluids*, 46:59–69, 2011.
- [66] R. Loubère, P.-H. Maire, M. Shashkov, J. Breil, and S. Galera. ReALE: A reconnection-based arbitrary LagrangianEulerian method. Technical Report LA-UR-09-07844, Los Alamos National Laboratory, 2009.
- [67] R. Loubère, P.-H. Maire, M. Shashkov, J. Breil, and S. Galera. ReALE: a reconnection-based arbitrary LagrangianEulerian method. *J. Comput. Phys.*, 229:4724–4761, 2010.
- [68] R. Loubère, P.-H. Maire, and P. Vachal. Staggered Lagrangian discretization based on cell-centered riemann solver and associated hydrodynamics scheme. *Communications in Computational Physics*, 10:940–978, 2011.
- [69] P.-H. Maire. A cell-centered arbitrary Lagrangian Eulerian method for two-dimensional multimaterial problems. In *MultiMat 2007: International Conference on Numerical Methods for Multi-Material Fluid Flows, Prague, September 10 - 14, 2007*, 2007.
- [70] P.-H. Maire. A high-order cell-centered Lagrangian scheme for compressible fluid flows in two-dimensional cylindrical geometry. *J. Comput. Phys.*, 228:6882–6915, October 2009.
- [71] P.-H. Maire. A high-order cell-centered Lagrangian scheme for two-dimensional compressible fluid flows on unstructured mesh. *J. Comput. Phys.*, 228:2391–2425, 2009.
- [72] P.-H. Maire. High-order cell-centered Lagrangian scheme for the simulation of elastic-plastic solids. In *MultiMat 2011: International Conference on Numerical Methods for Multi-Material Fluid Flows, Arcachon, France September 5-9, 2011*, 2011.
- [73] P.-H. Maire. A unified sub-cell force based discretization for cell-centered Lagrangian hydrodynamics on polygonal grids. *Int. J. Numer. Meth. Fluids*, 65:1281–1294, 2011.
- [74] P.-H. Maire, R. Abgrall, J. Breil, and J. Ovadia. A cell-centered Lagrangian scheme for two-dimensional compressible flow problems. *SIAM J. Sci. Comput.*, 29:1781–1824, 2007.
- [75] P.-H. Maire and J. Breil. A second-order cell-centered Lagrangian scheme for two-dimensional compressible flow problems. *Int. J. Numer. Meth. Fluids*, 56:1417–1423, 2008.
- [76] P.-H. Maire, J. Breil, and S. Galera. A cell-centered arbitrary Lagrangian-Eulerian (ALE) method. *Int. J. Numer. Meth. Fluids*, 56:1161–1166, 2008.
- [77] P.-H. Maire and B. Nkonga. Multi-scale Godunov-type method for cell-centered discrete Lagrangian hydrodynamics. *J. Comput. Phys.*, 228:799–821, 2009.
- [78] L.G. Margolin. A centered artificial viscosity for cells with large aspect ratios. Technical Report UCRL-53882, Lawrence Livermore National Laboratory, 1988.
- [79] D.S. Miller, D.E. Burton, and J.S. Oliviera. Efficient second order remapping on arbitrary two dimensional meshes. Technical Report UCID-ID-123530, Lawrence Livermore National Laboratory, March 1996.
- [80] N. R. Morgan, K. Lipnikov, D.E. Burton, and M.A. Kenamond. A Lagrangian staggered grid Godunov-like approach for hydrodynamics. *J. Comput. Phys.*, 259:568–597, 2014. LA-UR-13-23442.
- [81] N.R. Morgan, M.A. Kenamond, D.E. Burton, T.C. Carney, and D. J. Ingraham. An approach for treating contact surfaces in Lagrangian cell-centered hydrodynamics. *J. Comput. Phys.*, 250:527–554, 2012.
- [82] N.R. Morgan, J.I. Waltz, D.E. Burton, M.R. Charest, T.R. Canfield, and J.G. Wohlbiel. A point-centered arbitrary Lagrangian Eulerian hydrodynamic approach for tetrahedral meshes. *J. Comput. Phys.*, 290:239273, 2015.
- [83] S.J. Mosso and D.E. Burton. Two and three-dimensional interface reconstruction in unstructured meshes. Technical Report LA-UR-00-3522, Los Alamos National Laboratory, October 2000. NECDC.
- [84] S.J. Mosso, D.E. Burton, A.K. Harrison, E.J. Linnebur, and B.K. Swartz. A second-order, two and three dimensional remap method.

- Technical Report LA-UR-98-5353, Los Alamos National Laboratory, October 1998. NECDC, Las Vegas, October 25-30, 1998.
- [85] W. F. Noh. Errors for calculations of strong shocks using artificial viscosity and an artificial heat flux. *J. Comput. Phys.*, 72:78–120, 1987.
  - [86] J. M. Owen, R. Rieben, F. Najjar, and J. White. TP 105: Adiabatic release test problem. Technical Report LLNL-PRES-557631, Lawrence Livermore National Laboratory, 2112.
  - [87] James J. Quirk and S. Karni. On the dynamics of a shock-bubble interaction. *J. Fluid Mech.*, 318:129163, 1996.
  - [88] S. Ramsey. A class of self-similar hydrodynamic test problems. Technical Report LA-UR-10-08184, Los Alamos National Laboratory, 2010.
  - [89] J.D. Ramshaw. Simplified second-order rezoning algorithm for generalized two-dimensional meshes. *J. Comput. Phys.*, 67:214–222, 1986.
  - [90] S.K. Sambasivan, M.J. Shashkov, and D.E. Burton. Exploration of new limiter schemes for stress tensors in Lagrangian and ALE hydrocodes. *Comput. Fluids*, 86:98–114, 2013.
  - [91] S.K. Sambasivan, M.J. Shashkov, and D.E. Burton. A finite volume cell-centered Lagrangian hydrodynamics approach for solids in general unstructured grids. *Int. J. Numer. Meth. Fluids*, 72:770–810, 2013.
  - [92] S.K. Sambasivan and H.S. Udaykumar. A sharp interface method for high-speed multi-material flows: strong shocks and arbitrary material pairs. *Int. J. Comput. Fluid Dynamics*, 25(3):139–162, 2011.
  - [93] L.I. Sedov. *Similarity and Dimensional Methods in Mechanics*. Academic Press, 1959.
  - [94] M. Yu. Shashkov and A. V. Solovjov. Numerical simulations of two-dimensional flows by the free-Lagrangian method. Technical Report TUM-M9105, Technische Universitat Munchen, Mathematisches Institut, 1991.
  - [95] M.J. Shashkov. Closure models for multimaterial cells in arbitrary Lagrangian-Eulerian hydrocodes. *Int. J. Numer. Meth. Fluids*, 56:1497–1504, 2008.
  - [96] G.A. Sod. A survey of several finite difference methods for systems of non-linear hyperbolic conservation laws. *J. Comput. Phys.*, 27:1–31, 1978.
  - [97] G. I. Taylor. The use of flat-ended projectiles for determining dynamic yield stress, theoretical considerations. *Proc. R. Soc. London, Series A*, 194(1038):289–299, 1948.
  - [98] G. I. Taylor and A.E. Green. Mechanism of the production of small eddies from large ones. *Proc. R. Soc. London, Series A*, 158(499):499–521, 1937.
  - [99] R.E. Tipton. CALE mixed zone pressure relaxation model. Unpublished notes, Lawrence Livermore National Laboratory, 1989.
  - [100] H.S. Udaykumar, L. Tran, D.M. Belk, and K.J. Vanden. An Eulerian method for computation of multi-material impact with ENO shock-capturing and sharp interfaces. *J. Comput. Phys.*, 186:136–177, 2003.
  - [101] B. van Leer. Towards the ultimate conservative difference scheme I. the quest of monotonicity. *Lect. Notes Phys.*, 18:163–168, 1973.
  - [102] B. van Leer. Towards the ultimate conservative difference scheme II. monotonicity and conservation combined in a second-order scheme. *J. Comput. Phys.*, 14:361–370, 1974.
  - [103] B. van Leer. Towards the ultimate conservative difference scheme III. upstream-centered finite-difference schemes for ideal compressible flow. *J. Comput. Phys.*, 23:263–275, 1977.
  - [104] B. van Leer. Towards the ultimate conservative difference scheme IV. a new approach to numerical convection. *J. Comput. Phys.*, 23:276–299, 1977.
  - [105] B. van Leer. Towards the ultimate conservative difference scheme, V. a second-order sequel to Godunovs method. *J. Comput. Phys.*, 32:101, 1979.
  - [106] B. van Leer. Upwind and high-resolution methods for compressible flow: From donor cell to residual- distribution schemes. *Commun. Comput. Phys.*, 1:192–206, 2006.
  - [107] D. Verney. Évaluation de la limite Élastique du cuivre et de l’uranium par des expériences d’implosion. In *Behavior of Dense Media under High Dynamic Pressures, Symposium, H.D.P., IUTAM, Paris 1967*, pages 293–303. Gordon and Breach, New York, 1968.
  - [108] F. Vilar, P-H. Maire, and R. Abgrall. A discontinuous Galerkin discretization for solving the two-dimensional gas dynamics equations written under total Lagrangian formulation on general unstructured grids. *J. Comput. Phys.*, 276:188–234, 2014.
  - [109] F. Vilar, P-H. Maire, and R. Abgrall. A discontinuous Galerkin discretization for solving the two-dimensional gas dynamics equations written under total Lagrangian formulation on general unstructured grids. *Journal of Computational Physics*, 276:188–234, 2014.
  - [110] J. von Neumann and R.D. Richtmyer. A method for the calculation of hydrodynamic shocks. *J. Comput. Phys.*, 21:232–237, 1950.
  - [111] W. N. Weseloh, S. P. Clancy, and J.W. Painter. PAGOSA sample problems. Technical Report LA-UR-05-6514, Los Alamos National Laboratory, 2005.
  - [112] W. N. Weseloh, S. P. Clancy, and J.W. Painter. PAGOSA physics manual. Technical Report LA-14425-M, Los Alamos National Laboratory, 2010.
  - [113] M.L. Wilkins. Calculation of elastic-plastic flow. In B. Alder, S. Fernbach, and Manuel Rotenberg, editors, *Methods of Computational Physics*, volume 3. Academic Press, New York, 1964.
  - [114] M.L. Wilkins. The use of artificial viscosity in multidimensional fluid dynamic calculations. *J. Comput. Phys.*, 36:281, 1980.
  - [115] P. Woodward and P. Colella. The numerical simulation of two-dimensional fluid flow with shocks. *J. Comput. Phys.*, 54:115–173, 1984.
  - [116] D. L. Youngs. Time-dependent multi-material flow with large fluid distortion. In K. W. Morton and M. J. Baines, editors, *Numerical Methods for Fluid Dynamics*, pages 273–285. Academic Press, New York, 1982.